

Automated Acquisition of Brain MRSI Data

by

Eugene Ozhinsky

DISSERTATION

Submitted in partial satisfaction of the requirements for the degree of

DOCTOR OF PHILOSOPHY

in

Bioengineering

in the

GRADUATE DIVISION

of the

UNIVERSITY OF CALIFORNIA, SAN FRANCISCO

AND

UNIVERSITY OF CALIFORNIA, BERKELEY

Approved:

Sarah J Nelson  
Daryl B. Vrana  
Smichay

Copyright 2012

by

Eugene Ozhinsky

## Acknowledgements

First of all, I would like to thank my research advisor, Sarah Nelson for suggesting an excellent topic for my graduate research project, for great advice and countless ideas that helped steer this project towards completion and, in general, for helping me learn to navigate the academic research environment.

I am also very grateful to the members of my dissertation committee for helping me plan my work and giving very constructive feedback – to Dan Vigneron for being my academic advisor and guiding me through all the requirements of the program; to Susan Chang for helping me understand the clinical implications of brain tumor imaging; to Steve Conolly for giving me an outside perspective on the strengths and weaknesses of our methods; and to John Kurhanewicz for helping me understand the theory behind MR spectroscopy.

I would also like to thank my colleagues in the Nelson lab. Joe Osorio has started the work on improving outer volume suppression for the spectroscopic imaging of the brain that served as a foundation for this project. Janine Lupo and Esin Ozturk answered my countless questions and helped me understand the way data is acquired, processed and analyzed. Jason Crane and Beck Olson developed unique software for data processing and visualization, without which this project would not be possible. Adam Elkhaled, Trey Jalbert, Chris Williams, Angela Jakary and Wei Bian helped acquire and process the data that was used to test, evaluate and validate my techniques.

I am very thankful for the members of the Vigneron Lab – Peder Larson, Doug Kelley and Galen Reed for helping me with pulse sequence development. Collaboration with Adam Kerr from the Stanford University Department of Electrical Engineering was extremely valuable for me in understanding the physics of spatial saturation pulses.

I would also like to thank all patients and volunteers that were scanned for this project. Many hours of testing helped make the automated prescription and outer volume suppression methods effective and robust.

I am grateful to my family for continuously motivating me to focus on my goals and, especially, to my grandmother for showing me a first hand example of a successful career in science.

I would like to thank Blue Bottle Coffee, Farley's and Contraband Coffee Bar for excellent coffee that helped write this dissertation.

Lastly, I would like to acknowledge the funding agencies that made this work possible. Among them is National Institute of Health grants R01 CA127612, R01 CA111291 and P01 CA118816, UC Discovery Grant ITL-BIO04-10148 in conjunction with GE Healthcare and Surbeck Foundation Scholar Award.

## **Published Materials**

Chapter 4 is based on the journal article titled "Improved Spatial Coverage for Brain 3D PRESS MRSI by Automatic Placement of Outer-Volume Suppression Saturation Bands" (E. Ozhinsky, D.B. Vigneron, and S.J. Nelson), published in the Journal of Magnetic Resonance Imaging in 2011 and used with permission from Wiley.

Chapter 5 is based on the journal article titled "Automated Prescription of Oblique 3D Magnetic Resonance Spectroscopic Imaging" (E.Ozhinsky, D.B. Vigneron, S.M. Chang, and S.J. Nelson), published in "Magnetic Resonance in Medicine" in 2012 and is used with permission from Wiley.

Chapter 6 is based on an abstract "Novel Automated 3D MRSI Acquisition with Whole Brain Slice Selection and Outer-Volume Suppression" (E. Ozhinsky, A.B. Kerr, S.J. Nelson) that has been presented at the 19th annual meeting of the International Society for Magnetic Resonance in Medicine (ISMRM) in 2011.

Eugene Ozhinsky is the primary author of these published materials. His role included development of the methodology, performing experiments and data analysis.

# **Automated Acquisition of Brain MRSI Data**

**by Eugene Ozhinsky**

## **Abstract**

Magnetic Resonance Spectroscopic Imaging or MRSI is a noninvasive medical imaging modality that combines the principles of magnetic resonance imaging and spectroscopy to measure relative concentrations of metabolites in an array of voxels throughout the brain. Primary brain tumors are typically aggressive lesions that are difficult to treat and have a relatively poor prognosis for many patients. By showing metabolically active infiltrative tumor that can look similar to surrounding tissues on conventional MR images, MRSI allows for a more accurate definition of the extent of the disease. Despite those benefits, MRSI has not been widely used to care for patients with brain tumors. Two major difficulties encountered in implementing MRSI in a clinical setting are limited coverage and difficulty in prescription.

The goal of this dissertation work was to make MRSI more useful in the clinical setting. Several new techniques have been developed to automate MRSI prescription and acquisition, improve the coverage of the brain and ensure high quality data. They included automated placement of outer volumes suppression (OVS) bands for suppression of the subcutaneous lipid signal, placement of the excitation volume or slice and automated oblique shimming.

These techniques were validated on healthy volunteers and patients with brain tumors. They allowed the acquisition of MRSI data from a much larger brain

volumes than the conventional methods and resulted in more comprehensive and consistent MRSI datasets while maintaining high data quality.

The results of this work show that automated prescription can help solve two of the most significant problems with brain PRESS MRSI acquisitions: limited brain coverage and difficulty in prescription. The improved coverage will be useful for evaluating heterogeneous and infiltrative tumors, which are difficult to evaluate with current protocols. It should make possible a more accurate assessment of the progression of tumors in serial studies. The use of this technique reduced the need for extensive operator training, thus facilitating wider utilization of MRSI in the clinical setting. The automated MRSI protocols have been implemented in the ongoing clinical research studies and used to acquire data from hundreds of patients with brain tumors.

# **Table of Contents**

## **Chapter 1. Introduction 1**

### **Chapter 2. Background 5**

Brain Tumors 5

MR Imaging 10

MR Spectroscopy and Spectroscopic Imaging 18

Lipid Suppression 31

Image Segmentation 40

Optimization Methods 44

## **Chapter 3. Development of Software for Prescription, Acquisition and Processing of MRSI Data 52**

Introduction 52

Pulse Sequence Considerations 53

Pulse Sequence Development 57

Externally Prescribed OVS bands 58

Dualband VSS Pulses 61

Externally Prescribed PRESS box 65

Automated Prescription Software on the Scanner 66

Data Transfer 68

Shimming 68

Data Processing and Visualization Pipeline 69

## **Chapter 4. Automated Saturation Band Placement 73**

Introduction 73

Methods 75

Results 86

Discussion 94

## **Chapter 5. Automated Oblique Prescription 100**

Introduction 100

Methods 103

Results 115

Discussion 123

## **Chapter 6. Slice-Selected 3D MRSI with Automated Prescription 127**

Introduction 127

Methods 129

Results and Discussion 135

## **Summary 139**

Automated Saturation Band Placement 139

Automated Oblique Prescription 141

Slice-Selected 3D MRSI with Automated Prescription 141

Conclusion 142

## **Bibliography 144**

## List of Tables

<b>Table 2.1.</b> Effect of acquisition parameters on image weighting.	17
<b>Table 4.1.</b> 3D MRSI acquisition protocols that were compared in this study.	84
<b>Table 4.2.</b> Reproducibility of technique, measured by acquiring data from 3 healthy volunteers.	92
<b>Table 4.3.</b> Performance of the protocols in patients.	93
<b>Table 5.1.</b> 3D MRSI acquisition protocols that were considered in this study.	112
<b>Table 5.2.</b> Mean values across all subjects, Bland-Altman reproducibility coefficients and mean differences between measurements of the same subject for coverage volumes and metabolite ratios.	120
<b>Table 5.3.</b> Mean SNR efficiency and linewidth and their standard deviations of the NAA peak in the datasets, acquired from healthy volunteers with the protocols that were compared.	121

# List of Figures

<b>Figure 2.1.</b> Treatment schema for patients with grade IV glioma.	9
<b>Figure 2.2.</b> RF excitation.	11
<b>Figure 2.3.</b> Selective excitation of a slice.	13
<b>Figure 2.4.</b> MR images obtained from a patient with a grade-IV glioma.	17
<b>Figure 2.5.</b> $^1\text{H}$ NMR spectrum of the human brain at 7 T for single shot ( $N = 1$ ) and for 64 averages.	19
<b>Figure 2.6.</b> PRESS excitation.	21
<b>Figure 2.7.</b> Gradient waveform for the echo-planar trajectories (solid) and k-space points acquired (diamonds).	23
<b>Figure 2.8.</b> MRSI pulse sequence (sections scaled differently).	25
<b>Figure 2.9.</b> Visualization of MRSI data.	29
<b>Figure 2.10.</b> Spectra from healthy and malignant tissues.	30
<b>Figure 2.11.</b> Lipid spectra.	32
<b>Figure 2.12.</b> Lipid molecule.	33
<b>Figure 2.13.</b> Longitudinal magnetization of fat and water in relation to the inversion pulse.	35
<b>Figure 2.14.</b> Image of a phantom with OVS bands.	37
<b>Figure 2.15.</b> Saturation pulse (VSS).	38
<b>Figure 2.16.</b> Segmentation of an MR Image.	40
<b>Figure 2.17.</b> Gradient descent.	47
<b>Figure 3.1.</b> Parameters of a saturation band.	60
<b>Figure 3.2.</b> Cosine-modulated dualband VSS RF pulse.	62

<b>Figure 3.3.</b> Exponential-modulated dualband VSS RF pulse.	64
<b>Figure 3.4.</b> Automated prescription software running on the scanner console.	66
<b>Figure 3.5.</b> Shim GUI with "Load Oblique ROI" feature.	69
<b>Figure 3.6.</b> SIVIC software showing an MRSI dataset, acquired with automated prescription.	71
<b>Figure 4.1.</b> Anatomical image acquisition and processing.	76
<b>Figure 4.2.</b> The sequence of optimizations to obtain the saturation band prescription	78
<b>Figure 4.3.</b> MRSI dataset acquired with STANDARD protocol.	87
<b>Figure 4.4.</b> MRSI dataset acquired with OCTAGONAL protocol.	88
<b>Figure 4.5.</b> MRSI dataset acquired with AUTOSAT protocol.	89
<b>Figure 4.6.</b> Pairwise comparison of coverage volume (cm <sup>3</sup> ) and SNR efficiency of NAA and lipid peaks for exams with two MRSI acquisitions.	90
<b>Figure 4.7.</b> Convergence of the optimization algorithm.	95
<b>Figure 5.1.</b> Technique overview.	104
<b>Figure 5.2.</b> The stages of prescription optimization.	107
<b>Figure 5.3.</b> Example of the covered volumes acquired from a healthy volunteer	115
<b>Figure 5.4.</b> Covered volume of the three volunteers using the three protocols that were compared.	116
<b>Figure 5.5.</b> Dataset, acquired from a patient using the AUTO MRSI protocol.	118
<b>Figure 5.6.</b> Consistency of prescription and data quality.	122
<b>Figure 6.1.</b> MRSI localization techniques.	128
<b>Figure 6.2.</b> Automated placement of the selected slice.	130

<b>Figure 6.3.</b> Saturation band optimization sequence.	132
<b>Figure 6.4.</b> Software on the scanner console.	133
<b>Figure 6.5.</b> MRSI pulse sequence with single- and dual-band OVS pulses (sections scaled differently).	134
<b>Figure 6.6.</b> Comparison of images of a phantom with cosine-modulated dualband pulses (left) and exponential-modulated dualband pulses (right).	135
<b>Figure 6.7.</b> Healthy volunteer MRSI acquisition.	136

# **Chapter 1. Introduction**

Magnetic Resonance Imaging (MRI) is a non-invasive medical imaging modality that allows the visualization of the anatomy without subjecting patients to harmful ionizing radiation. Many types of MR acquisition techniques have been developed, which use different contrast mechanisms to give clinicians insight in the anatomy, structure and physiology of healthy and diseased tissues.

MRI is uniquely suited to providing diagnostic information from the brain. X-rays and computed tomography (CT) are good at imaging bones and large organs, but they do not show distinction between soft tissues well. They also require significant doses of ionizing radiation, which provide a risk for causing cancer. Ultrasound is inexpensive and is widely used for imaging internal organs but is unable to penetrate well into the skull. Positron emission tomography (PET) and single-photon emission computed tomography (SPECT) produce low-resolution images and require injection of radioactive isotopes. They can be used for imaging brain cancer but are best when applied in combination with anatomic images obtained with MRI and CT.

Primary brain tumors are typically aggressive lesions that are difficult to treat and have a relatively poor prognosis for many patients. Finding therapies that are effective in defeating brain tumors or in at least postponing their growth requires the identification of biomarkers that indicate whether the treatment is working or not without having to wait months or years until the patient succumbs to the disease. There have been a number of such MR biomarkers developed in recent years and this field remains an area of active research.

In the last few decades, the view of cancers has evolved into the understanding that it is not a single disease, but a family of related diseases that may require different therapeutic strategies. MR Imaging can help to sort or "stratify" patient populations by disease type. This allows the identification of subgroups of patients for whom certain treatments are likely to be most effective.

MR imaging has also been instrumental in the diagnosis, treatment and research of a number of neurodegenerative diseases such as multiple sclerosis (MS), Parkinson's disease, traumatic brain injury (TBI) and psychiatric conditions, such as depression, schizophrenia and substance abuse.

Magnetic Resonance Spectroscopy (MRS) uses similar principles as MR imaging, but instead of showing anatomical images, it allows for the detection of relative concentrations of certain chemical compounds in the tissue. This allows for the identification of metabolically abnormal tissues, such as a tumor.

Magnetic Resonance Spectroscopic Imaging or MRSI combines the principles of MRI and MRS to measure relative concentrations of metabolites in an array of voxels throughout the brain. The data can be displayed as a grid of spectra or as metabolite maps, overlaid on top of anatomic MR images. By showing metabolically active infiltrative tumor that can look similar to surrounding tissues on conventional MR images, MRSI allows for a more accurate definition of the extent of the disease than MRI because it provides the ability to distinguish between infiltrating tumor cells, solid tumor, necrosis (dead tissue), edema (swelling) and gliosis (scarring). MRSI has been successfully used for planning surgery and radiation therapy. MRSI

parameters are also used as biomarkers of malignancy and aggressiveness of the tumor.

Despite those benefits, MRSI has not been widely used to care for patients with brain tumors. This is largely due to the difficulty in obtaining good quality MRSI data in clinical as opposed to research centers. Among the challenges faced when applying spectroscopic imaging techniques are long acquisition times, low spatial resolution, poor coverage of the brain, interfering signal from fat tissues and sinuses and difficulty of exam prescription.

The unifying goal of the projects that became this dissertation was to make MRSI more useful in the clinical setting. To accomplish that I have developed techniques to automate MRSI prescription and acquisition, improve the coverage of the brain and ensure high quality data. The tools that have been developed were validated on healthy volunteers and patients with brain tumors and implemented in the hospital for routine clinical research examinations.

Chapter 2 describes the background and provides the reader with a brief overview of brain tumors, MR imaging and spectroscopy, and numerical optimization methods. It discusses the methods, currently used for image processing, accelerated spectroscopic imaging and lipid suppression.

Chapter 3 discusses the pulse sequences and scanner software developed in this project to enable the automated acquisition of 3D MRSI data. It describes the custom software pipeline used for processing and quantification of MRSI data and the changes to this pipeline that had to be made to accommodate processing of obliquely prescribed datasets with extended coverage.

Chapter 4, "Automated Sat Band Placement" presents the work done to increase the coverage of 3D MRSI by providing effective automated outer volume suppression. This chapter is based on the manuscript called "Improved Spatial Coverage for Brain 3D PRESS MRSI by Automatic Placement of Outer-Volume Suppression Saturation Bands," published in the Journal of Magnetic Resonance Imaging in 2011 (1) and used with permission from Wiley.

Chapter 5, "Automated Oblique Prescription" describes the project to completely automate the process of MRSI scan prescription. It made possible to include 3D MRSI into the clinical research protocols without the need for extensive operator training, yielding consistent prescription quality and further increasing the coverage of the brain. This work has been published in "Magnetic Resonance in Medicine" in 2012 (2) and is used with permission from Wiley.

Finally, Chapter 6, "Slice Selected 3D MRSI" presents further work on improving the brain coverage in 3D MRSI by employing whole-brain slice selection with an optimized outer-volume suppression scheme that used custom dual-band radio-frequency pulses for lipid suppression. This work has been presented at the 19th annual meeting of the International Society for Magnetic Resonance in Medicine (ISMRM) in 2011 (3).

# **Chapter 2. Background**

## **Brain Tumors**

### **Epidemiology**

In 2012 it is anticipated that approximately 1.6 million cases of cancer will be diagnosed in the US. Almost 600,000 people will die of cancer – a quarter of all deaths in this year (4). Brain tumors are relatively uncommon, with the annual incidence of malignant primary brain tumors is 6-7 per 100,000 people. In the US this will translate to 23,000 cases of brain and nervous system cancers this year – with almost 14,000 deaths. Primary brain tumors account for 95% of tumors of the primary nervous system (5). Gliomas and other neuroepithelial tumors account for about half of primary brain tumors. Despite their relatively low incidence, brain tumors are very deadly, with the 5 year survival for brain cancers in the period between 2001 and 2007 being 35% in comparison with 67% for all cancers.

The two general categories of brain tumors are primary and metastatic. Primary tumors originate from the cells in the brain, while metastatic tumors originate in other organs and eventually migrate to the brain. Primary brain tumors are often more invasive and do not exhibit a defined boundary between the tumor and healthy tissue.

### **Classification**

Primary brain tumors are classified by the type of brain cells that have undergone oncogenic transformation to give rise to the tumor. Those, which originate from glial cells – the support cells of the brain – are called gliomas. They can be further divided into astrocytomas (originating from astrocytes),

oligodendrogiomas (oligodendrocytes), ependymomas (ependymal cells) and mixed tumors, which exhibit characteristics of more than one type of glial cell.

Primary brain tumors are further classified by the malignant characteristics that are observed in tissue samples obtained from biopsy or surgical resection as defined criteria specified by the World Health Organization (WHO). Criteria that pathologists use to define astrocytic tumor grade include nuclear atypia, mitotic activity, endothelial proliferation and presence of necrosis as follows:

- Grade 1 tumors are benign and slow growing. They are localized and can be completely cured by excision.

- Grade 2 tumors (low grade) are characterized by invasive cells and the presence of nuclear atypia. They are treatable and have relatively good prognosis with treatment: median survival is 5-10 years. These tumors progress to higher grade.

- Grade 3 tumors (anaplastic) exhibit nuclear atypia and increased mitosis. Median survival for anaplastic tumors is around 3 years.

- Grade 4 tumors, called glioblastoma multiforme or GBM, exhibit signs of necrosis or endothelial proliferation in addition to the rest of the features above. Median survival for patients with GBM is only 9-12 months. They are, unfortunately, the most common type of primary brain tumors.

The tumor grade does not necessarily correspond to the stage of the disease. For example GBM (grade 4) can be either newly diagnosed or have upgraded from a lower grade after disease recurrence.

## **Diagnosis and Treatment**

There is no screening test for gliomas. Brain tumor diagnosis is suspected when the patient presents with one or more neurological symptoms. Newly appearing seizures are the most common symptom. Other possibilities are headaches and neurological deficits, such as hemiparesis (weakness on one side of the body), aphasia (impairment of language), or sensory abnormalities.

Imaging (MRI, CT) is used to determine whether there is a mass lesion and whether surgical resection is appropriate. Histological diagnosis of tumor grade depends upon the analysis of the tissue samples obtained during biopsy or surgery. The neuro-oncologist uses a combination of factors, including tumor grade, location and patient's condition to select treatment.

Treatment for malignant glioma involves a combination of surgery, radiotherapy and chemotherapy. The surgery is used to relieve symptoms due to the mass effect of the tumor and to remove as much of the tumor as possible. Complete removal of these infiltrative tumors is often not possible due to difficulty in defining the margins and to proximity to critical cortical areas or white-matter pathways. The extent of tumor resection has been shown to correlate with patient survival (6). Tissue samples collected during the surgery are used to determine tumor grade.

Radiation therapy is used in an attempt to kill residual tumor cells by inflicting DNA damage. The target area is planned based on MR images with the goal of delivering the highest doses to the tumor and minimizing damage to normal tissue. Stereotactic radiosurgery or gamma knife is used to treat tumors in locations that are impossible to reach surgically.

Chemotherapy drugs are used to further suppress disease progression by targeting fast-dividing cells in the body. The range of chemotherapy agents effective in the brain is limited due to the presence of blood-brain barrier, which prevents large molecules from entering the brain tissue from the bloodstream. Temozolomide (TMZ) is one of the few agents that can cross the blood-brain barrier and is the current standard of care for patients with high grade glioma.

In the recent years there has been a significant interest in using anti-angiogenic drugs, such as bevacizumab (Avastin) for treatment of brain tumors. Traditionally it was thought that these drugs prevent tumor growth by suppressing growth of blood vessels that feed the tumor. However, there is still no consensus on the mechanism of action of these drugs in the brain. While reducing inflammation around the tumor these drugs have been shown to make tumors more diffuse, their effectiveness in improving patient survival is still a hotly debated topic. Selecting the most effective treatment protocol, parameters and timing of individual therapies for different types of tumors is an active area of medical research.

Imaging is used to monitor the extent of tumor resection and presence of residual tumor. Patients receive regular scans to monitor response to treatment and disease progression. Since it is impossible to completely destroy all the tumor cells, the disease will eventually recur at the site of or close to the original lesion. At that point another cycle of treatment may be prescribed. Due to mutation and natural selection of the cells, that are resistant to therapy, the recurring tumor is often more malignant than the primary one.

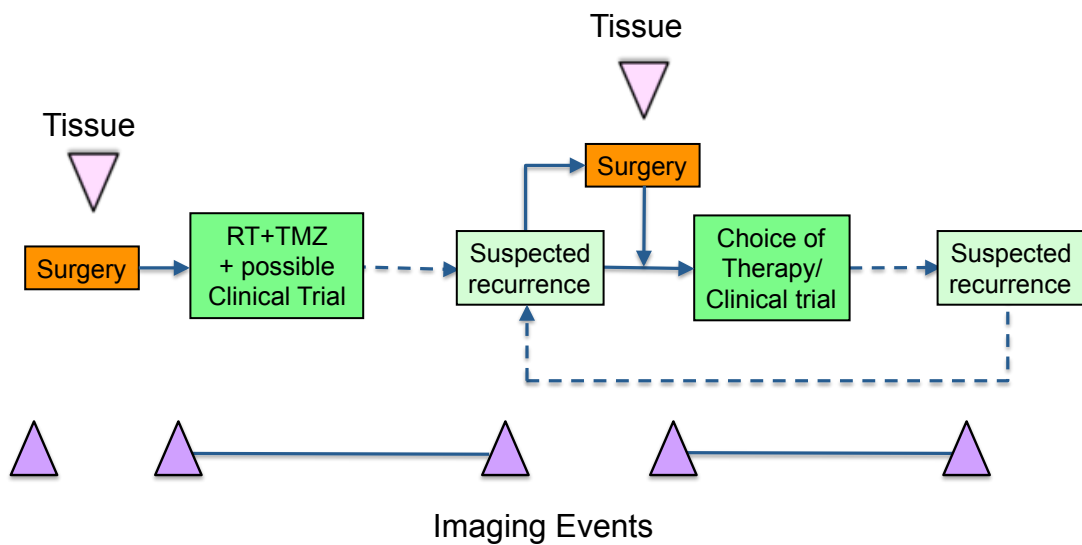


**Figure 2.1.** Treatment schema for patients with grade IV glioma.

The time points at which imaging is used to plan surgery and radiation therapy, to assess tumor burden and to evaluate the response to therapy are shown in purple.

Figure courtesy S.J. Nelson.

## **MR Imaging**

Magnetic Resonance Imaging (MRI) is a non-invasive medical imaging modality that allows the visualization of the anatomy of the patients without subjecting them to harmful ionizing radiation. The patient lies inside a strong magnet that has constant field strength. The scanner emits radio-frequency (RF) pulses in the presence of additional varying magnetic fields (gradients) and records the RF "echo" of those pulses, produced by the molecules of the body. Digital processing of those echoes allows for the reconstruction of images in the body.

### **Spin physics**

In quantum mechanics, elementary particles, such as electrons and composite particles, such as protons and nuclei of atoms have a property of angular momentum, called spin. The spin quantum number of the nucleus is determined by its composition. Isotopes that are composed of an odd number of protons or neutrons have non-zero magnetic moment, and thus, non-zero spin. The spins of such nuclei precess in an external magnetic field with a frequency proportional to the field strength:

$$\omega = \gamma B_0 \quad [2.1]$$

where gamma is called the gyromagnetic ratio and B<sub>0</sub> is the external magnetic field. The frequency of precession is referred to as the Larmor frequency.

Without an external magnetic field, the spins of the nuclei in the tissue are oriented randomly, making the combined magnetization zero. When an external magnetic field is applied the spins tend to orient themselves parallel or anti-parallel to the magnetic field. There is an energy difference between these two states:

$$\Delta E = \frac{\gamma h}{2\pi} B_0$$

[2.2]

where  $h$  is the Planck's constant.

The ratio of the nuclei that occupy those states depends on the energy and temperature and is described by the Boltzmann's distribution:

$$\frac{N_+}{N_-} = e^{-\frac{\Delta E}{kT}}$$

[2.3]

where  $T$  is the temperature and  $k$  - Boltzmann's constant. This ratio determines the total magnetization of the tissue.

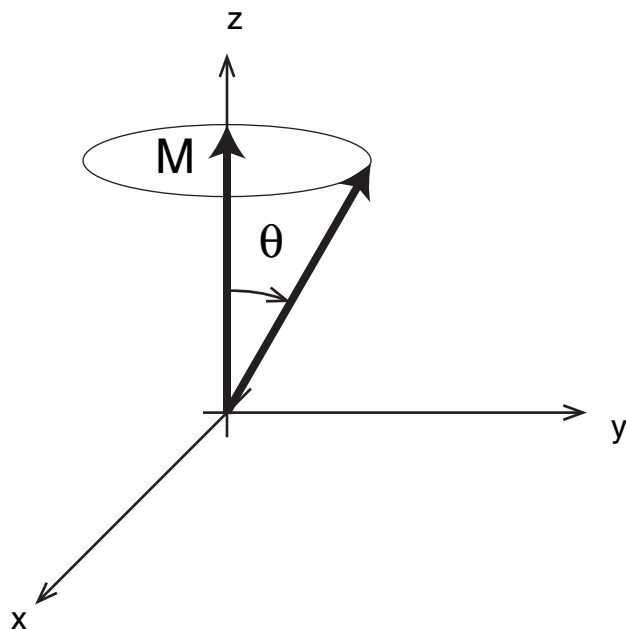


**Figure 2.2. RF excitation.**

When the net magnetization vector is aligned with the main magnetic field, it cannot be detected by the scanner. In order to tip the magnetization vector into the orthogonal direction, an RF pulse tuned to the resonant frequency of the spins is played. It can be thought as providing an additional temporary magnetic field  $B1$  in

the XY (transverse) plane. This magnetic field will tip the magnetization vector by an angle:

$$\theta = \gamma B_1 \tau \quad [2.4]$$

where  $\tau$  – time the B1 pulse was on.

The transverse component of the magnetization vector can be detected using RF received coils, tuned to the frequency of precession. After the excitation, the magnetization vector comes back to its equilibrium state via two processes: spin-lattice relaxation and spin-spin relaxation. Spin-lattice or T1 relaxation refers to the return of the longitudinal magnetization to its thermal equilibrium due to interaction between the nuclei and their surrounding lattice. It is described by equation:

$$M_z(t) = M_{z,eq} \left( 1 - e^{-\frac{t}{T1}} \right) \quad [2.5]$$

where T1 is the time it takes to regain approximately 63% ( $1 - 1/e$ ) of its value.

The spin-spin relaxation is responsible to decay of the transverse component of the magnetization vector. It is characterized by the constant T2, which represents the time for the magnetization to reach 37% ( $1/e$ ) of its initial value:

$$M_{xy}(t) = M_{xy}(0) e^{-\frac{t}{T2}} \quad [2.6]$$

The transverse magnetization can be further separated into T2\* relaxation due to inhomogeneity of the magnetic field and T2 relaxation due to interaction of excited spins with other spins. T2\* is usually much shorter than T2, but can be alleviated with spin-echo technique. Recovering magnetization due to T2 relaxation requires performing another excitation.

Taking these effects into account, the behavior of the magnetization vector can be described by the Bloch equation:

$$\frac{d\mathbf{M}}{dt} = \mathbf{M} \times \gamma \mathbf{B} - \frac{M_x \mathbf{i} + M_y \mathbf{j}}{T_2} - \frac{(M_z - M_0) \mathbf{k}}{T_1} \quad [2.7]$$

where  $\mathbf{i}, \mathbf{j}, \mathbf{k}$  - unit vectors in x, y, z directions respectively

### Localization

To generate images from the magnetic resonance signal it is necessary to distinguish between the signals coming from different parts of the tissue. One way to localize the signal is through selective excitation. If a gradient magnetic field is added during the excitation, the spins in the different parts of the tissue will precess at different frequencies. The RF pulse can be designed to excite a range of frequencies, called bandwidth. By adjusting the gradient strength and orientation and the carrier frequency of the RF pulse, an arbitrary slice in space can be excited.

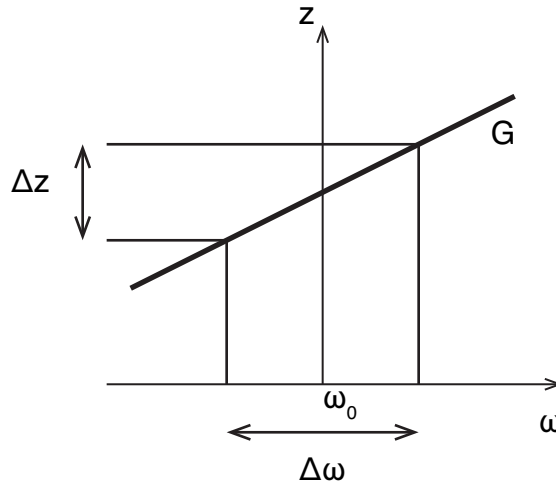


**Figure 2.3. Selective excitation of a slice.**

*RF pulse with carrier frequency  $\omega_0$  and bandwidth  $\Delta\omega$  applied in the presence of a gradient  $G$ , resulting in excitation of a slice  $\Delta z$ .*

Another technique, used to localize MR signal is frequency encoding. When applying a different gradient magnetic field during signal acquisition, spins in the different parts of the tissue precess with different frequencies. The recorded signal will be the combination of all of those signals. This makes it possible to separate the intensity of the signals along one axis.

The third technique that is commonly used for localization is phase encoding. It is similar to frequency encoding, except that the gradient magnetic field is turned on for a period of time after the excitation, but before the acquisition. During the time the gradient is on, spins from where the field is stronger rotate faster, while others rotate slower. When the gradient is turned off, the spins resume their regular rate of precession, but their relative position, or phase is different. This phase difference can be detected during signal acquisition.

Although each of those techniques allows localization of the signal along a single dimension, the combination of slice selection, frequency and phase encoding allows the MR signal to be resolved in three dimensions, producing a volumetric image of the object.

## **Reconstruction**

To generate images from the data that are acquired, the spatial dependence of the signals need to be reconstructed. It can be shown that the acquired MRI signal can be described by the following equation:

$$s(t) = \int \int_{x, y} m(x, y) e^{-i2\pi[k_x(t)x + k_y(t)y]} dx dy \quad [2.8]$$

where:

$$k_x(t) = \frac{\gamma}{2\pi} \int_0^t G_x(\tau) d\tau \quad k_y(t) = \frac{\gamma}{2\pi} \int_0^t G_y(\tau) d\tau \quad [2.9]$$

As can be seen from these equations, the recorded signal represents a 2D Fourier transform of the original image intensity.  $k_x$  and  $k_y$  can be thought of as spatial frequencies of the image. The acquired data can be described as points in the spatial-frequency space or k-space, where samples close to the origin (low spatial frequencies) describe the general shape of the object, while the samples further away describe fine features of the object. The image of an object can be reconstructed from k-space data by performing an inverse Fourier transform.

Although it is possible to acquire the signal directly after excitation, the early part of the signal is difficult to sample and the signal decays very fast due to spin-spin relaxation, which results in a very short acquisition window and poor signal-to-noise ratio (SNR). This type of acquisition is called a free induction decay or FID.

A better way to sample MR signal is to generate an "echo." After the excitation, a gradient can be applied to rapidly spread or "defocus" the precessing spins. Then the gradient field of an opposite sign is applied. That makes the spins refocus to the same coherent state they were at the time of excitation, and then defocus again. Using the echo allows for the signal to be sampled longer in the vicinity of the coherent state of the spins which have the highest magnitude of signal and contain information on the most important lowest spatial frequencies of an object. This approach is called "gradient echo" or GRE.

Another way to generate an echo is by using an RF pulse instead of gradient field to refocus the spins. After the initial  $90^\circ$  excitation, the spins are allowed to

spread for time  $\tau$ . A  $180^\circ$  RF pulse is then applied to flip the spins in the transverse plane. Since the slower precessing spins are now in front of the faster precessing ones, the fast spins will catch up with the slow ones, generating an echo after a period  $2\tau$ . This period is called an "echo time" or TE and the technique of using an additional RF pulse to refocus the spins is called a "spin echo." After the signal is sampled and the longitudinal magnetization has recovered, the excitation can be repeated. The period between excitations is referred to as "repetition time" or TR. The biggest advantage of the spin-echo is that, unlike the gradient echo, it is less sensitive to the local magnetic field variations and the signal decay is dominated by a relatively long T2, rather than the extremely short T2\*.

Spin-echo-based sequences can generate different contrast between tissues, depending on the choice of TE and TR. A proton-density image reflects the concentration of water molecules in the tissue. It cannot distinguish between tissues that have similar amounts of water. The signal in T1-weighted images depends on the relaxation times of individual tissues and can help to distinguish between grey and white matter in the brain. Similarly, a T2-weighted image often shows inflammation or edema because of a large amount of fluid that has longer T2 in the affected tissues. Additionally, contrast agents, such as gadolinium compounds are used to highlight tissues where blood leaks from the vessels by shortening the T1 of the signal from those areas.

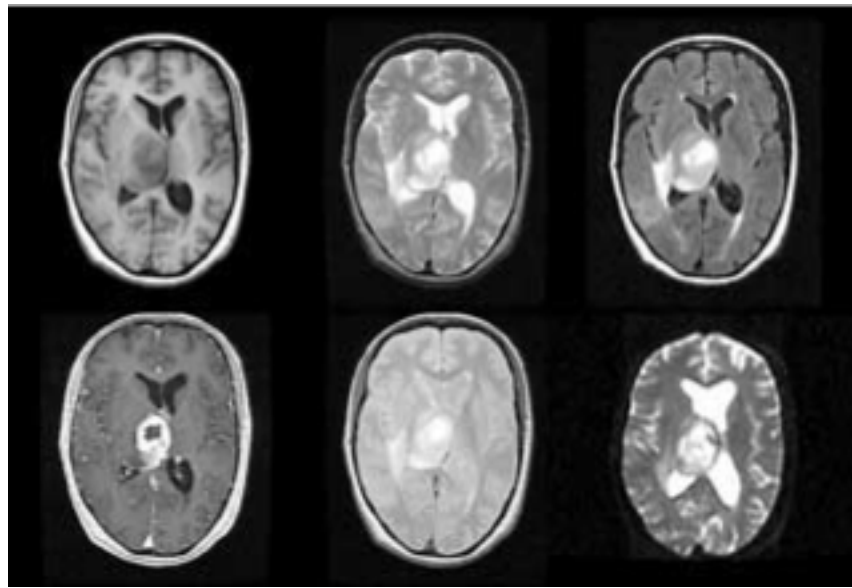


**Figure 2.4.** MR images obtained from a patient with a grade-IV glioma.

The images presented on the top row are pre-Gadolinium T1-weighted, T2-weighted spin echo, and FLAIR weighted; on the bottom row are post-Gadolinium T1-weighted, proton density-weighted spin echo, and a T2-weighted echo planar. Figure from: Nelson SJ. Magnetic resonance spectroscopic imaging. Evaluating responses to therapy for gliomas. IEEE Eng Med Biol Mag 2004;23(5):30-39. © 2004 IEEE (7)

weighting	TR	TE
proton-density	long	short
T1	short	short
T2	long	long

**Table 2.1.** Effect of acquisition parameters on image weighting.

## MR Spectroscopy and Spectroscopic Imaging

MR Spectroscopy (MRS) is a non-invasive imaging technique that uses similar principles to those of MR Imaging but differs in that it is used to quantify relative concentrations of compounds in the tissue rather than create an anatomical image. MR spectroscopy allows assessment of the biochemical and functional status of the tissue to, for example, distinguish between cancerous and healthy tissues.

### Chemical Shift

The phenomenon that makes MRS possible is a change in the resonant frequency of protons depending on their local microenvironment, which is called "chemical shift." The motion of electrons in the presence of an external magnetic field produces electric current around the nucleus. That current produces a small local magnetic field that opposes, or shields the nucleus from the external magnetic field. Many factors, such as local electron density, vicinity of electronegative atoms, effects from interatomic currents and molecular interactions can have an additional shielding or de-shielding effect. The small difference in magnetic fields, experienced by the nuclei results in a change in their frequency of precession:

$$\omega_i = \gamma B_0 (1 - \sigma_i) \quad [2.10]$$

where  $\sigma_i$  - chemical shielding of nucleus  $i$  in the compound.

$$\delta_i = \frac{\omega_i - \omega_{ref}}{\omega_{ref}} \cdot 10^6 \quad [2.11]$$

The chemical shift  $\delta_i$  is defined by the relative frequency offset of a nucleus to the reference frequency – commonly the resonance frequency of tetramethylsilane (TMS) and is measured in parts per million (ppm). MR spectra are traditionally

plotted with higher ppm values on the left and lower values on the right of the horizontal axis.

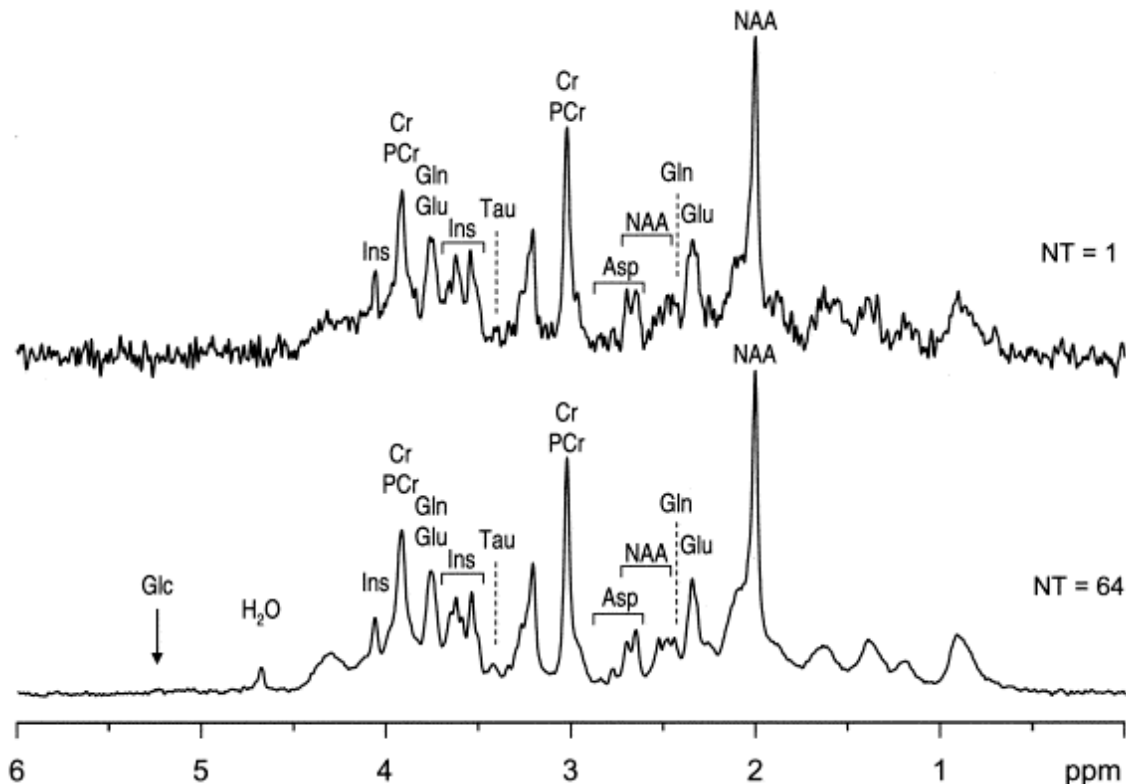


**Figure 2.5.**  $^1\text{H}$  NMR spectrum of the human brain at 7 T for single shot ( $N = 1$ ) and for 64 averages.

Reprinted from Magnetic Resonance Imaging, Volume 21, Issue 10, Kâmil Uğurbil et al., Ultrahigh field magnetic resonance imaging and spectroscopy, Pages 1263–1281, Copyright 2003, with permission from Elsevier.

Other protons in the vicinity of the nucleus affect its precession frequency with the environment of these protons affecting the amount of shielding they cause. Each proton in the magnetic field can have one of two possible spin orientations, so the magnetic field of the neighboring protons can have one of two possible values,

making the peak appear split. This effect is called spin coupling or J-coupling. The number of split peaks is proportional to the number of neighboring protons. The frequency difference between the split peaks does not depend on the applied magnetic field and is called the J-coupling constant.

### **MRS Signal**

MRS acquisition is similar to MRI, except that a gradient magnetic field is typically not used during signal readout. The recorded signal becomes a combination of the signals produced by nuclei that precess at different frequencies due to chemical shift:

$$S(t) = \int_f M(f) e^{-i2\pi ft} df \quad [2.12]$$

The spectrum can be reconstructed by applying an inverse Fourier transform to the acquired data.

### **MRS Localization**

In order to restrict the volume that generates the signal to the volume of interest, a number of localization techniques have been developed (8). Point-Resolved SpectroScopy, or PRESS, is one of the most commonly used techniques. It employs a double spin-echo sequence (fig. 2.6). The first 90° RF pulse with an accompanying gradient excites a slice, orthogonal to the Y axis. After a time TE1/2, a 180° pulse and a gradient along X refocuses only the intersection of spins, excited by these two pulses, forming a column. After a time TE2/2 another 180° degree pulse selects a slice, orthogonal to Z. An echo is formed TE2/2 after the second 180° pulse.

Only the spins that have been selected by all of the 3 pulses (a rectangular box) get refocused.

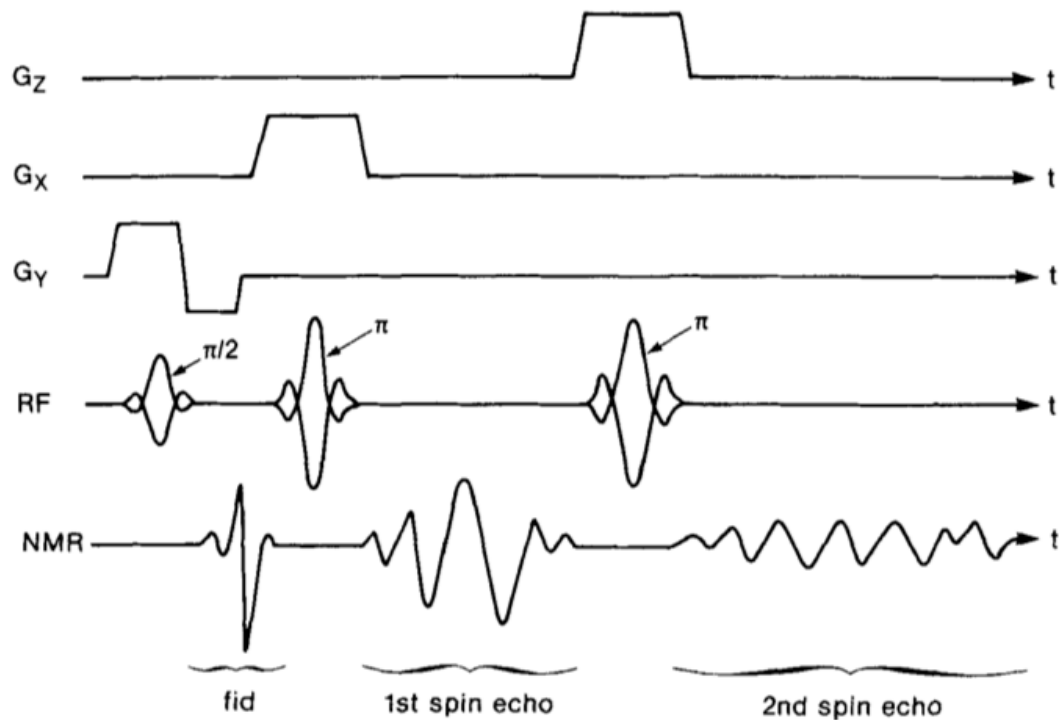


**Figure 2.6.** PRESS excitation.

Reprinted from Bottomley. *Spatial Localization in NMR Spectroscopy in Vivo* (8) with permission from Wiley.

A serious limitation of the PRESS selection is that the selected volume has to resemble a rectangular prism. Techniques such as 2DRF excitation (9) have been proposed to overcome this by exciting an arbitrary shaped volume. They require very long RF excitation pulses and can have problems with chemical shift misregistration due to the limited bandwidth of those pulses. The volume of interest could be also localized using outer volume suppression (OVS). This will be discussed in detail in later chapters.

## MR Spectroscopic Imaging

MR Spectroscopic Imaging allows the simultaneous acquisition of spectra from an array of voxels. It uses similar localization techniques to select the excited volume as single voxel spectroscopy with additional localization to be able to resolve the data from the voxels within that volume. Phase encoding could be used to perform such localization in one, two or all three dimensions. To fully sample the k-space, the pulse sequence has to go through all combinations of the gradient amplitudes for G<sub>x</sub>, G<sub>y</sub> and G<sub>z</sub>.

The acquired signal for 3D MRSI acquisition can be expressed as:

$$s(t) = \int_x \int_y \int_z \int_f M(x, y, z, f) e^{-i2\pi(xk_x + yk_y + zk_z + fk_f)} dx dy dz df \quad [2.13]$$

where:

$$k_{x,y,z}(t) = \frac{\gamma}{2\pi} \int_0^t G_{x,y,z}(\tau) d\tau \quad [2.14]$$

$$k_f = t$$

## Accelerated MRSI

The resolution and field of view of MRSI used to be severely limited due to the long acquisition times resulting from 3D phase encoding. For instance, an acquisition with a 16x16x8 cm field of view, 1x1x1 cm voxel size and the repetition time (TR) of one second would take 34 minutes.

A number of techniques have been developed to accelerate MRSI acquisitions. Among the first was reduced k-space sampling, where the phase encodes, corresponding to the corners of k-space, which contribute the least to the

data quality are not acquired and replaced with zero values. The drawback of this method is that it lowers the effective spatial resolution.

Another approach that leads to more dramatic acceleration is encoding both chemical and spatial information during signal readout. The k-space can be sampled using a number of trajectories, such as spiral, propeller or echo-planar.

The spiral and propeller trajectories are characterized by high efficiency, but they suffer from limited spectral bandwidth, are more susceptible to eddy currents and timing errors and require a more complicated reconstruction that regrids the data onto a Cartesian grid.

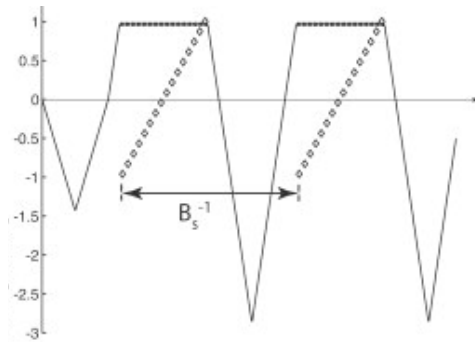


**Figure 2.7.** Gradient waveform for the echo-planar trajectories (solid) and k-space points acquired (diamonds).

Reprinted from Cunningham et al. *Design of Flyback Echo-Planar Readout Gradients for Magnetic Resonance Spectroscopic Imaging* (10) with permission from Wiley.

Echo-planar trajectories scan k-space along the parallel lines and can achieve high efficiency, large bandwidth. They are also more robust to acquisition imperfections and require relatively simple reconstruction. A flyback trajectory is a type of echo-planar trajectory that employs two segments to encode spatial and frequency information together. The data is acquired during a flat segment of the

gradient waveform. Than a short rewind lobe follows. It retraces the k-space back as quickly as possible, using the maximum slew rate and amplitude of the gradient that the hardware is capable of.

### **Magnetization Preparation**

The metabolites of interest are present in tissue in concentrations much smaller than those of water and lipids. To be able to detect the metabolite signals reliably, a number of magnetization preparation techniques are used to suppress or severely attenuate water and lipid signals.

The CHESS technique (Chemical Shift Selective Imaging) (11) uses one or more frequency-selective  $90^\circ$  pulses, followed by spoiling gradients to excite and de-phase spins, resonating in a given frequency range. Other compounds with different chemical shift remain unaffected. Subsequent excitation pulses, e.g. PRESS can only excite the spins that still have longitudinal magnetization. Lipid suppression, being a major focus of this work is discussed in greater details later.

### **BASING**

Resolving some compounds is not straightforward, since their signals overlap with other peaks. One example is the lactate peak, which lies over approximately the same frequency as the lipid peak. To overcome that, spectral editing techniques, such as BASING (Band Selective Inversion with Gradient Dephasing)(12) could be used. The BASING sequence utilizes a frequency selective  $180^\circ$  RF pulse and crusher gradients of opposite polarity. These crushers dephase any spins that were flipped by the  $180^\circ$  pulse and remove any net magnetization

from the target spin. This technique could be used to effectively suppress water and lipid signals.

The dual BASING sequence could be used for lactate editing (13). Lactate has a methyl peak (doublet) at 1.3 ppm and methine (quartet) at 4.1 ppm. Applying BASING pulse to the methyl peak can control phase of methyl. So, every excitation is performed twice. In the first acquisition, BASING pass band includes methine, resulting upright methyl peak at TE = 144 ms. In the second acquisition methine is excluded, TE adjusted to be multiple of  $1/J$ , producing an inverted lactate peak. During post-processing, the sum and difference spectra are generated from these two acquisitions. Sum spectra will have all the metabolites except lactate, while the difference spectra will contain only the lactate peak.

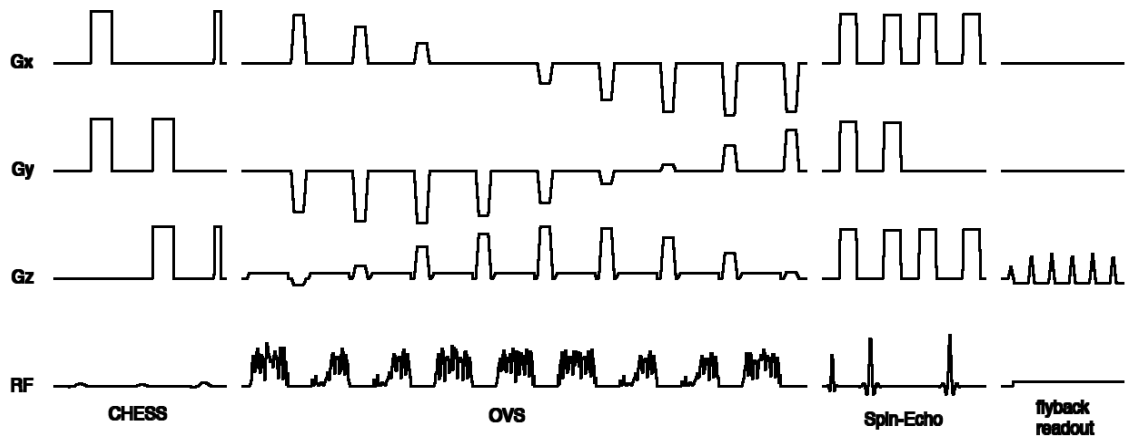


**Figure 2.8.** MRSI pulse sequence (sections scaled differently).

### B0 Shimming

The uniformity of the main magnetic field of the scanner is important for acquiring high quality MR imaging data. Inhomogeneity of the field can result in geometric distortions and signal dropouts due to dephasing of magnetization within individual voxels. For MR Spectroscopy, variation of magnetic field leads to the

spread of resonant frequencies of the protons of the same compound and ultimately to line broadening. Since the area under the peak is proportional to the concentration of the compound, wider peaks will be shorter and may be obscured by noise. Line broadening can also result in the overlap of the neighboring peaks, which makes it difficult to resolve them.

Field homogeneity on the order of 1 part per million is needed for MRI and MRS acquisitions. The superconducting magnets used in MRI scanners can never achieve this degree of homogeneity. The uniformity of the field depends on magnet imperfections, the magnetic fields of the environment (building, equipment, etc.) and even the patient anatomy. The air-tissue interfaces in the oral cavity, sinuses and ear canals cause variability of the field due to the susceptibility effect. Field inhomogeneity is an important problem at high magnetic field.

To mitigate these effects and make the main field more homogeneous, additional corrective magnetic fields are applied. This process is called "shimming" the magnet. Shimming can be passive or active. Passive shimming is performed during the manufacture or setup of the MRI scanner and involves placing pieces of steel with known magnetic properties in the carefully chosen locations on the magnet. Active shimming is done with magnetic coils during data acquisition.

Correcting linear field variations can be done by applying additional corrective currents to the gradient coils. The nonlinear field distortions require using high-order shimming coils. For example, the commonly used second order shimming coils include  $Z^2$ ,  $ZX$ ,  $ZY$ ,  $X^2-Y^2$  and  $XY$ . By carefully choosing the currents for these coils, together with the first-order shims, a wide variety of field

imperfections can be corrected. Due to the increased susceptibility artifacts and due to higher sensitivity to field variations at higher field the use of even higher-order shims (3rd, 4th and 5th order) have been proposed for 7T or higher field scanners.

The common approach to optimize the shim for a particular acquisition is to estimate the shim currents that would result in the minimum root-mean-square (RMS) value of  $B_0$  inhomogeneity over the region of interest (ROI) (14). Field maps of each shim coil are acquired during scanner setup or maintenance. During the imaging exam, the field map of the object being scanned is acquired using a fast proton-density pulse sequence with echo-planar or spiral trajectory. A mathematical model of the magnetic field is used to iteratively adjust the shim currents. The resulting values are then downloaded to the hardware and used during the MR acquisition.

### **MRSI Reconstruction**

Reconstruction of MRSI data is more complicated than that for regular MR images and due to its complexity and high computational demands it is commonly performed offline after the scan (15,16).

First, the raw file, containing the acquired data is transferred through the network to a workstation. The acquisition parameters are extracted from the raw file and written to a data descriptor file. The data from each receiver channel is extracted from the raw file, reordered for consistency, and is written to a separate file. To speed up the processing, the data from each channel is reconstructed in parallel on different machines of a computing cluster.

If echo-planar flyback acquisition has been used, the data points from the ramp portion are discarded, and a phase correction is performed to compensate for the tilted k-space sampling pattern. The data is filtered by apodization in time domain with Lorentzian or Gaussian Filter. Then the inverse Fourier transform is applied in X, Y, Z, and frequency dimensions.

Frequency correction is performed on a voxel-by-voxel basis to remove variation in the positions of the peaks. It uses a peak descriptor file, listing the positions of the peaks and their widths. A statistical peak finding algorithm estimates the frequency shift for the major peaks in every spectrum and calculates the mean shift.

Similarly, the phase correction algorithm estimates the mean phase shift for each channel of data, using a set of voxels in the middle of the field of view that are likely to have the highest signal to noise ratio.

The baseline removal algorithm makes the metabolite peaks easier to compare and quantify by making the baseline flat. Among the sources of the baseline signal are contributions of macromolecules that are too numerous and too varied to generate sharp peaks and the slopes of the residual water peak. The algorithm isolates the peaks of interest, based on the peak descriptor files and estimates the baseline by fitting a smooth curve to the remaining data points.

The metabolite data can be quantified in a number of ways, by calculating the height of the peaks or the area under each peak. The peak ratios give information of the relative concentrations of metabolites. Z-scores, such as Choline-to-NAA Index (CNI) are calculated by calculating residuals from fitting the metabolite values of the

voxel onto the linear regression curve, calculated from the metabolite values of the voxels of the healthy tissue.

The spectroscopy data is displayed on a rectangular grid, one slice at a time. The position of the grid is shown on the anatomical MR image, acquired during the same exam. The results of metabolite quantification can be displayed numerically within each voxel or as a metabolite map, overlaid over the image or spectra (17).

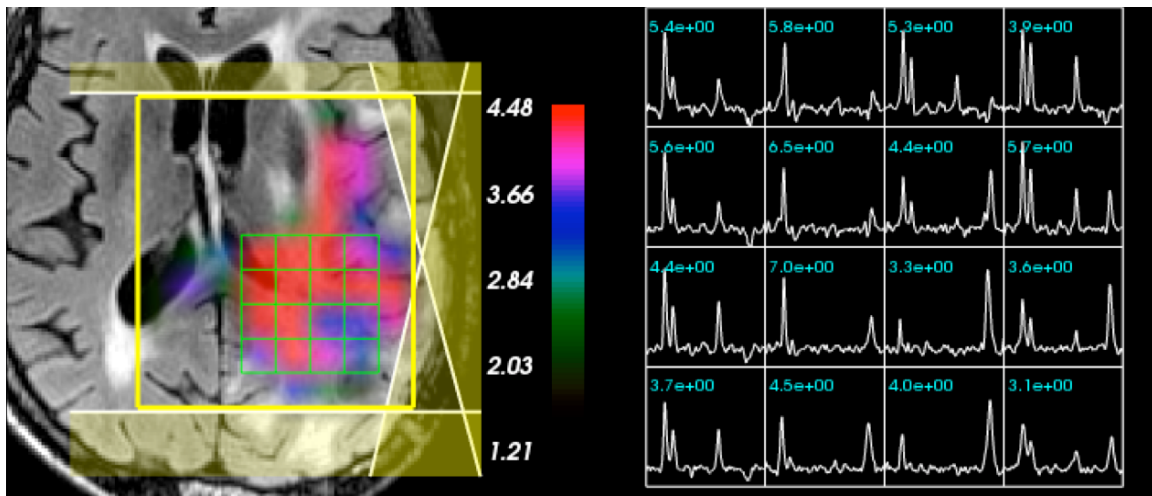


**Figure 2.9.** Visualization of MRSI data.

Figure courtesy Jason Crane and Beck Olson (17).

## Applications

MR Spectroscopic Imaging has been shown to be a valuable tool in studying the diseases of the brain and other organs and for evaluation of disease state and response to therapy in cancer, neurodegenerative and psychiatric diseases.

In brain tumors, the main metabolites of interest are Choline, Creatine and NAA. The main resonance for Choline is at 3.2 ppm and is composed of contributions from several compounds, such as free choline, phosphocholine and

glycerophosphocholine. Elevated Choline indicates increased membrane turnover corresponding to increased cellularity and/or increased proliferation.

The creatine peak (3.0 ppm) is composed of the signal from creatine and phosphocreatine and is linked to cellular metabolism. These compounds act as energy reservoirs by storing phosphates for ADP/ATP cycles.

N-acetyl aspartate (NAA, 2.0 ppm) is a neuronal marker. NAA is present within functioning neurons. Decreased NAA is common when the tumor displaces or damages neurons.

In the normal brain Choline and Creatine peaks are approximately equal in height, while the NAA is 1.2-2x higher. Spectra from malignant tissue typically exhibit elevated Choline and decreased NAA and Creatine.

Two other important metabolites in brain tumors are Lactate and Lipid, both resonating at 1.3 ppm. Lipid within the tumor indicates cellular membrane breakdown and necrosis. Lactate is a product of anaerobic metabolism. Its presence indicates hypoxia in the tumor that has been shown to be lead to resistance to radiotherapy. Other metabolites that have been studied in brain tumors include glutamine, glutamate and myo-inositol.

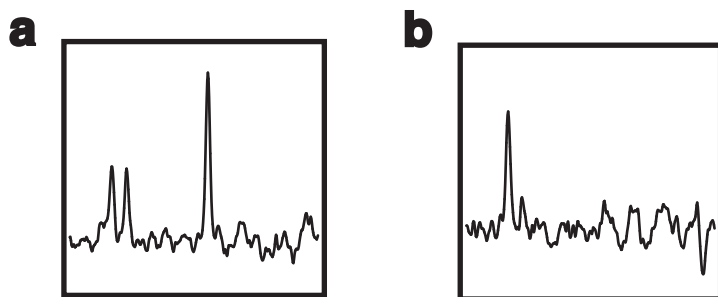


**Figure 2.10.** Spectra from healthy (a) and malignant (b) tissues.

## Lipid Suppression

### Problem

Interference from fat signal has long been a major problem in MR imaging and spectroscopy. Since fat has relatively short T1, fat signal often appears very bright, obscuring the diagnostically relevant features.

Fat contamination is especially big problem in brain MR spectroscopy. In the head, metabolites of interest, Choline, Creatine, Lactate and N-Acetyl-Aspartate (NAA) appear in concentrations on the order of  $10^4$  smaller than that of water or subcutaneous lipids (fatty tissues under the skin). While water signal can be successfully suppressed using techniques, such as CHESS, lipid peaks, are difficult to suppress spectrally, since they overlap with the metabolites of interest. If subcutaneous lipids are excited, the “ringing” artifact appears in voxels within the brain tissue due to side-lobes of the point-spread function of excited protons.

Figure 2.11b shows a slice of magnitude MRSI data with unsuppressed lipid signal. Due to Gibbs ringing, contributions of lipid can be seen beyond the area of subcutaneous fats. Figure 2.11c shows a voxel with unsuppressed water and lipid peaks. The lipid peak is much wider than that of water, since it is composed from contributions of many different CHx groups in different configurations.

The lipid contamination artifact results from ringing, caused by side-lobes of point-spread function of lipid protons. Assuming that the resolution of the spectroscopy data is  $1 \times 1 \times 1$  cm, the point-spread function of the acquisition follows  $\text{sinc}(x)$  and would result in the contribution of approximately 10% at a distance of 2.5 cm from the excited lipid.

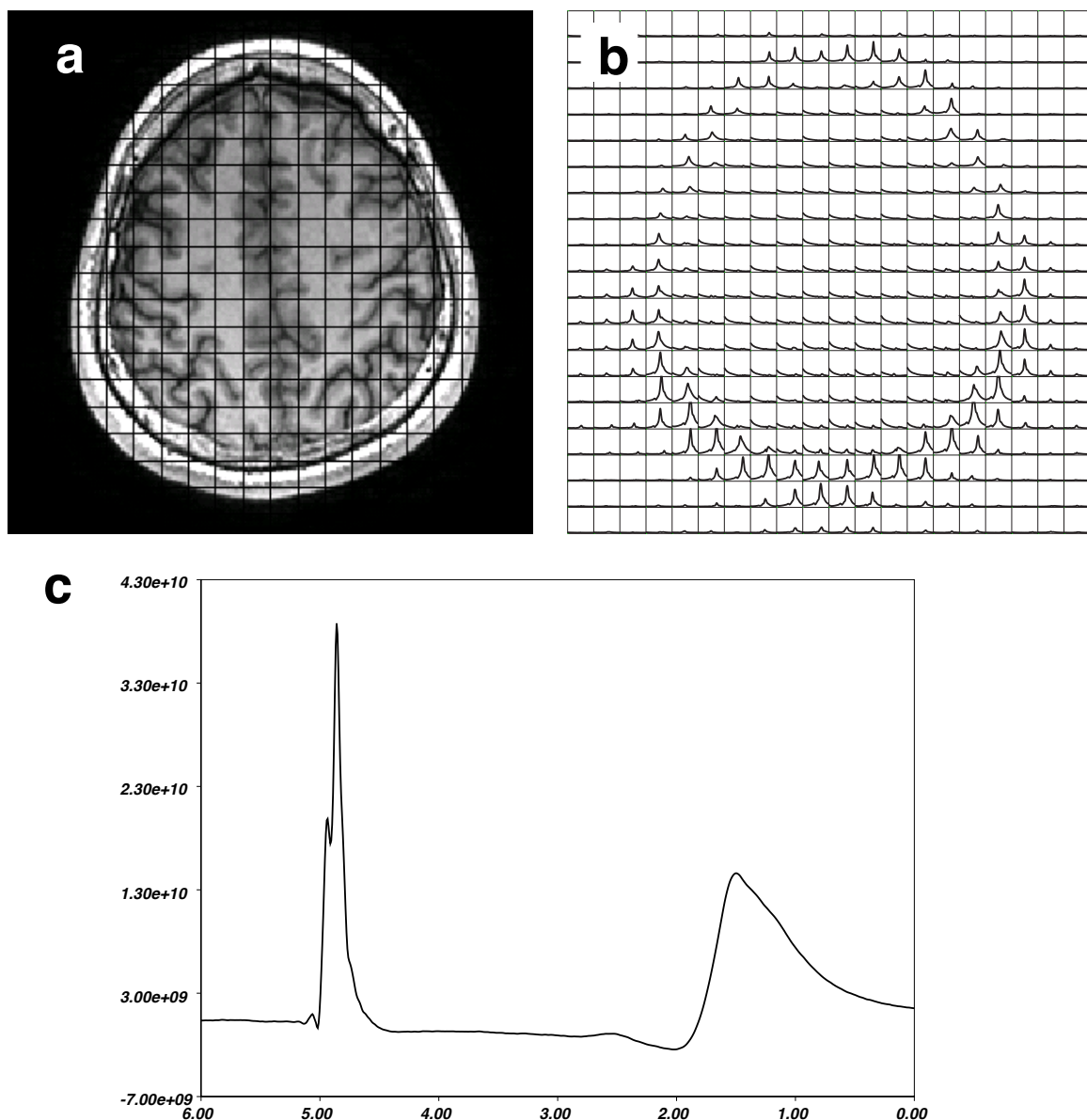


**Figure 2.11.** Lipid spectra.

(a) T1 weighted image showing subcutaneous fat layer; (b) unsuppressed lipid spectra

(c) unsuppressed water and lipid peaks

Based on the reported concentration of NAA in the normal brain of approximately 10 mM (18), the total number of NAA protons contributing to the signal in 1 kg of brain tissue is estimated to be about  $18 \times 10^{21}$ . Assuming that lipid has approximately the same proton density as water (98 for fat, 100 for CSF) (19)

and the molar mass of water of 18 g/mol, the number of contributing protons in a kg of lipid tissue would be on the order of  $6.54 \times 10^{25}$ . Since average thickness of the subcutaneous lipid layer is 3 mm (20), the effective concentration of lipid in 1 cm<sup>3</sup> voxel is would be 3 mM. Based on observed lipid spectra, since the area under the peak is proportional to the number of protons, for the same number of protons the lipid peak will be 4x wider and approximately 4x shorter. Lipid has a shorter T2 (85 ms) than Cho, Cre, NAA (200-300 ms), so after TE=144 it will have attenuated about 3x more. If the artifact were required to be less than 10% of the NAA peak, the total suppression of lipid required would be around 23-fold.

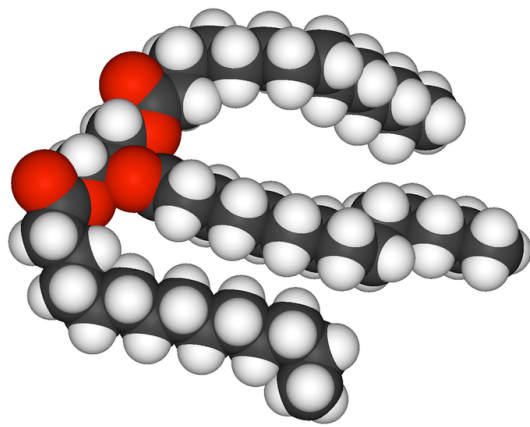


**Figure 2.12.** Lipid molecule.

*Image created by Ben Mills, published under public domain at  
<http://commons.wikimedia.org/wiki/File:Trimyristin-3D-vdW.png>*

### General Lipid Suppression Methods

Lipid signal is sufficiently separated by frequency from the water signal, so chemically selective suppression methods, such as CHESS have been used for fat

suppression in MRI imaging. The BASING technique (12) discussed above in the sections on water suppression and lactate editing, could also be used to perform lipid suppression. Hypergeometric dualband (HGDB) pulses were designed by Zhu et al. (21) to perform simultaneous suppression of water and lipids for MR spectroscopic imaging. Chemically selective fat suppression is widely used in MRI of organs, other than head and neck. It is versatile, relatively fast, applicable to most pulse sequences and is highly effective where B0 and B1 fields are relatively homogenous, such as knee, pelvis and abdomen. It is, however, very sensitive to B0 and B1 inhomogeneity, which can cause incomplete suppression of fat or accidental suppression of water signal. Since metabolites of interest in the brain, such as NAA and Lactate have resonant frequencies close to that of lipid, these techniques are not well suited for MR spectroscopy of the brain.

A different approach is to avoid exciting the fat peak, instead of suppressing it. Spectral-spatial pulses use a train of selective RF sub-pulses following an envelope and can limit excitation both in space and in frequency domain. They are insensitive to B1 variation, versatile, relatively fast. At the same time they are also very sensitive to B0 inhomogeneity and require very long excitation pulses that reduces overall efficiency of the sequence. Spectral-spatial excitation is commonly used in many MRI and MRS application, except those of head, neck and extremities (22).

Another set of methods relies on phase shifts due to the differences in fat and water resonance frequencies to spatially separate the water and fat images. They are commonly known as "Dixon" water-fat separation methods (23) and are often

used when the lipid image itself provides valuable information, such as in the MRI of liver.

Short TI Inversion Recovery (STIR) technique uses the difference in T1 times between water, fat and metabolites to suppress the fat signal (24). After inverting the longitudinal magnetization, it is allowed to regrow (fig. 2.13). At some point the magnetization of the lipid protons will be at zero, while water protons would still have negative longitudinal magnetization. If an excitation pulse were played at that moment, there would be no contribution of lipid in the detected signal.

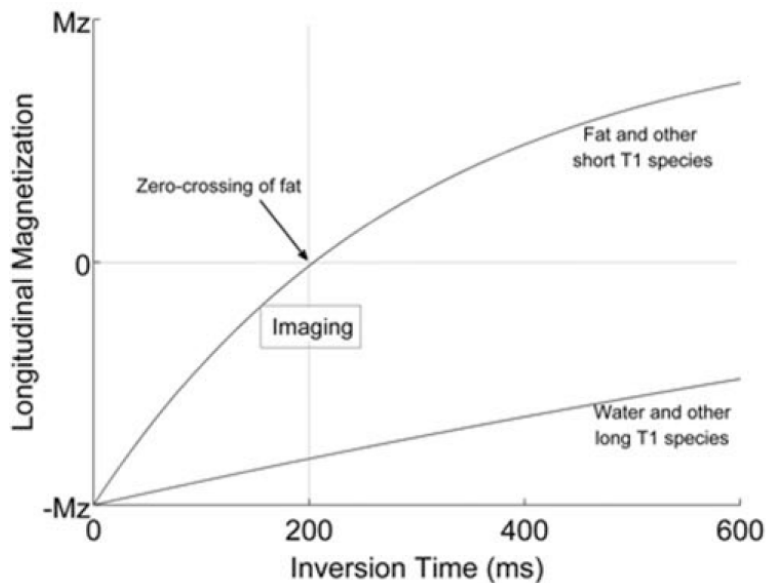


**Figure 2.13.** Longitudinal magnetization of fat and water in relation to the inversion pulse.

Reprinted from Bley et al. Fat and Water Magnetic Resonance Imaging (22) with permission from Wiley.

This method is robust to  $B_0$  and  $B_1$  inhomogeneity, reliable and produces uniform fat suppression. It has been widely used for both imaging and spectroscopy

(25-27). The limitations of STIR include inherent T1 weighting, low SNR efficiency.

It alters image contrast in MRI and the peak ratios in MR spectroscopy. The variability of T1 values of in vivo lipids makes their complete suppression difficult.

When applied to the spectroscopic imaging of the brain, all of these methods not only suppress the subcutaneous lipid signal, but also signal from the lipids within the brain. This would make it impossible to quantify the lipid within the lesion, which is a valuable biomarker of tumor malignancy (28).

Another approach is to reduce the Gibbs ringing from subcutaneous lipids in the brain tissue by improving effective spatial resolution or by applying spatial filtering to the data. Spatial filtering by itself, while effective in reducing the ringing artifacts, leads to the loss of effective spatial resolution. To improve spatial resolution, a larger phase encoding matrix could be used, but that would result in even longer acquisition times. To overcome that, sequences with spiral k-space trajectories, that provide fine sampling in the center of the k-space and sparse sampling in the periphery have been proposed (29). Another proposed approach involves k-space extrapolation by estimating high spatial frequency components of the lipid signal.

To obtain optimal lipid suppression, these methods are often used in combination. For example, Maudsley et al. used a combination of lipid inversion nulling, increased in-plane resolution (50x50) and iterative k-space extrapolation to reduce ringing artifacts from subcutaneous lipids (30).

## Outer-Volume Suppression

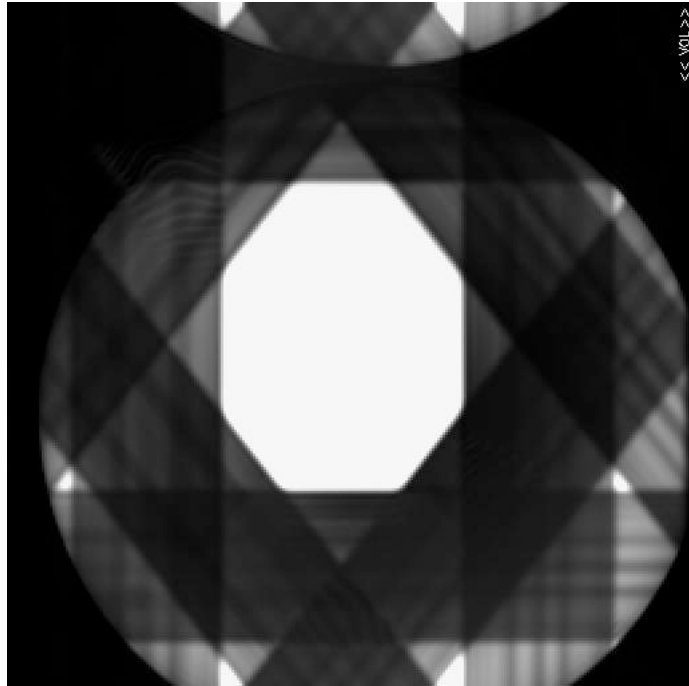


**Figure 2.14.** Image of a phantom with OVS bands.

For the brain MR spectroscopy and MR spectroscopic imaging, outer-volume suppression is widely used to suppress the signal from subcutaneous lipids. Its goal is to suppress the signal from the area outside the volume of interest, minimizing the aliasing and ringing artifacts from those areas.

Outer volume suppression is usually implemented with a number of saturation bands or sat bands with each sat band eliminating most of the MR signal from a slab of space. It is accomplished by exciting this slab using an RF pulse in a presence of slice-selection gradients and de-phasing excited spins using crusher gradients. When PRESS excitation is performed, the areas under the sat band cannot be excited any more until their longitudinal magnetization recovers.

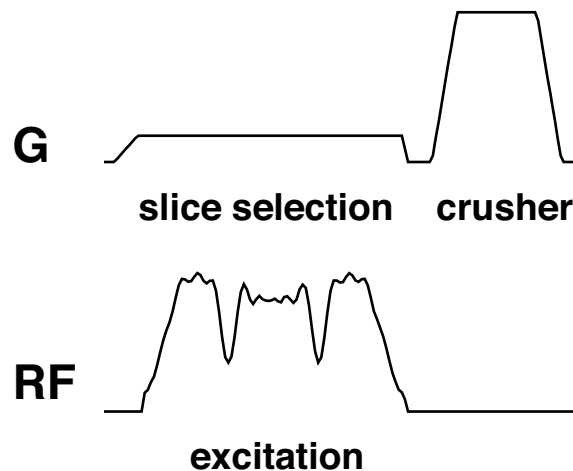


**Figure 2.15.** Saturation pulse (VSS).

Conventional sinc-shaped pulses for OVS bands have relatively low bandwidth and high peak amplitude. These limitations result in poor edge profiles, B1 and T1 sensitivity, chemical shift effect and long excitation times.

Unlike regular excitation pulses, saturation pulses do not have to have a linear phase response, since the spins do not need to be refocused later. That makes it possible to design shorter pulses with higher bandwidth that spread the energy evenly throughout the entire pulse.

Tran et al. used Shinnar-Le Roux algorithm to design short quadratic-phase pulses sharper transition width, while minimizing the peak power (31). High level of B1 and T1 insensitivity was achieved when using two or three VSS pulses per saturation band.

The limited bandwidth of excitation pulses of the PRESS selection makes it difficult to obtain a sharp excitation profile. Moreover, because of the chemical shift effect, the volume of excitation for lactate and lipid is significantly shifted from that

of choline. To overcome that, an overprescribed OverPRESS method was developed in which the PRESS volume is automatically enlarged by a factor of 1.2 - 1.5 over that prescribed (32). That ensures that all metabolites are excited within the prescribed volume. Outer-volume suppression is used to sharpen the profile of the excited area. Because of their much higher bandwidth, the saturation pulses are less susceptible to chemical shift.

Several MRSI acquisition methods that did not use PRESS selection have been proposed to increase the brain coverage. All of them required additional steps to minimize the lipid contamination. Henning et al. (33) presented the spin-echo MRSI localized by OVS (SELOVS) technique that used two cycles of OVS (10 suppression pulses in each cycle) with numerically optimized flip angles to minimize the residual lipid signal in the regions where OVS bands crossed. The technique was applied to slice selected 2D MRSI at 3T and later to free-induction decay MRSI at 7T (34). Similarly, Posse et al. described their proton echo-planar spectroscopic imaging (PEPSI) sequence with a nine-band OVS module and 32x32 spatial matrix for slice-selected 2D MRSI within clinically acceptable acquisition times ((35)). Application of PEPSI to 3D MRSI (36) applied filtering of data in spatial domain to reduce the lipid ringing.

## Image Segmentation

Segmentation is a fundamental problem of image analysis. It helps to extract information from a digital image by classifying pixels of an acquired digital image into objects. Its applications lie in such diverse fields as computer vision and optical character recognition. In medical imaging, segmentation is used for identifying anatomical structures, image registration and quantitative image analysis.

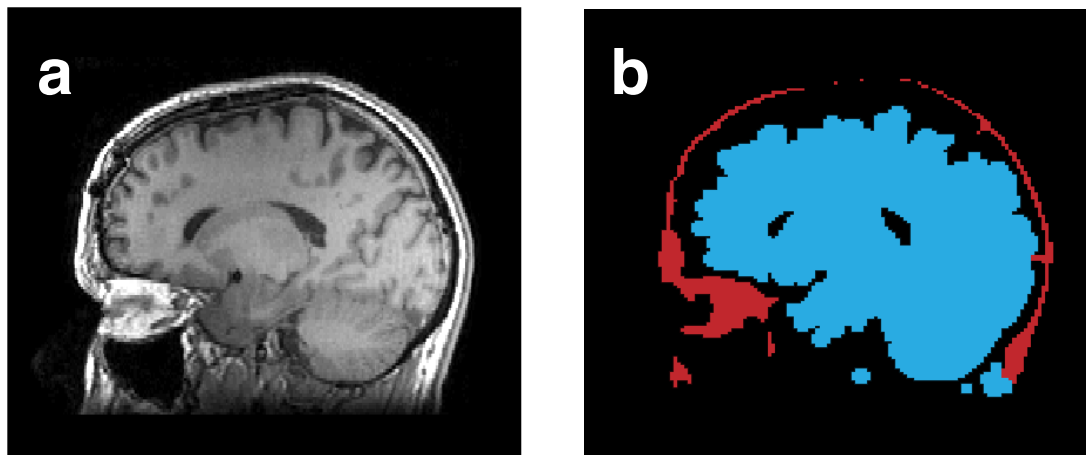


**Figure 2.16.** Segmentation of an MR Image.

(a) original image (b) segmented image

Segmentation techniques can roughly be classified into manual, semi-automated and automated. Manual segmentation requires an operator to outline the objects he or she sees on the images. Semi-automated techniques make some steps automatic, but require operator input or corrections at some stages of the process. Automated techniques perform entire segmentation without human input.

The segmentation usually involves the following steps:

1. *Preprocessing.* Filters, such as noise suppression and contrast enhancement are applied to the image being segmented to enhance features.

*2. Feature extraction.* Segmentation algorithm uses features of the image that range from simple (pixel intensities) to complex (edges, textures, shape)

*3. Segmentation.* Pixels are group together into objects, based on similarity, shape constraints or statistical models. The algorithms can take into account a-priori knowledge about the data or determine the parameters using the training datasets.

The simplest segmentation algorithm is thresholding. Pixel intensities are chosen as features. An object is defined as all the pixels that have intensities between the predefined thresholds. Thresholding works well only in datasets where the objects are consistently separated by intensity.

Clustering assigns data points to a set number of groups, so that those with similar values are placed in the same group. The similarity is based on some distance metric, in the simplest case – the difference between pixel values.

For example, the K-nearest neighbor algorithm chooses the class for each data point based on the most prominent class among its neighbors. This algorithm requires a well-classified training data as an input. It assumes that each data point tends to belong to the same class as those around it.

The K-means clustering algorithm, used later in this work, requires no training data. It starts with randomly assigned centers of k clusters. At each iteration of the algorithm all the data points are partitioned based on distance to the centers of the current mean. Then the new means are calculated based on the updated clusters. The iteration ends when the cluster means converge, i.e. the change in their values between the subsequent iterations is smaller than a preset threshold. K-

means clustering is guaranteed to converge to a local optimum, although not necessarily to a globally optimal solution. On the other hand it is sensitive to initial mean placement and doesn't work well in case of overlapping regions. It also works only with continuous values and assumes data points should be classified similar to their neighboring points.

The fuzzy c-means clustering algorithm does not assume that a point belongs to a certain cluster, but estimates a degree of belonging to a cluster based on the distance to the centroid of the cluster.

Edge detection algorithms use the abrupt changes in intensity as features to determine object boundaries. An approximation of the derivative is usually used to find areas where the boundary is likely to be present.

Region growing algorithms avoid the problem of multiple objects having similar intensities by choosing a seed pixel and then iteratively adding neighboring pixels that are similar to it. When growth stops, the algorithm chooses another seed pixel and starts growing another region. The weak point of these algorithms is that their results are biased, depending on the selection of the initial seed. To overcome that, simultaneous region growing, where the regions from several randomly chosen seeds are being grown in parallel have been proposed.

Among other segmentation approaches is watershed segmentation that treats areas of high gradient magnitude as watershed lines. The objects are defined by catch basins, formed by the topographic surfaces of the image gradient. Statistical shape models use a-priori knowledge about the shape to define an object that can be deformed based on the features, found in an image. The Markov random field

segmentation methods are based on a conditional probability model. The probability of a pixel belonging to an object depends largely on its neighborhood. These methods allow the algorithm to incorporate the a-priori knowledge about the object shape into the model.

*4. Classification and labeling.* The last step of the segmentation process is to assign the labels are to the segmented objects, based on their location, size, shape, signal intensity, or other features.

# Optimization Methods

## Problem

Optimization problems comprise a large area of applied mathematics. Many computational problems can be expressed in terms of minimizing a function  $f_0(x)$ , subject to constraints  $f_i(x) \leq b_i, i = 1 \dots m$ , where:  $x = (x_1, \dots, x_n)$  – variables being optimized,  $f_0$  – objective function, and  $f_i$  – constraint functions. The goal is to find the optimal solution  $x^*$  that gives the smallest value to  $f_0$ , while satisfying the constraints.

## Special Cases of Optimization Problems

The general optimization problem is difficult to solve, but there are algorithms that can solve certain classes of optimization problems very efficiently. For example, the least squares problem is widely used for fitting noisy data to a model. The cost function of the form  $|Ax-b|^2$  is used to minimize the residuals between data points and the model. An analytical solution exists for solving least square problems.

The problems where both the objective function and constraints are linear are called linear programming problems. They can be expressed as:

$$\min c^T x \quad [2.15]$$

$$a_i^T x \leq b_i, i = 1 \dots m$$

Although no analytical solution exists for the linear programming problems, there are algorithms that solve such problems efficiently, for example the simplex algorithm of George Dantzig (37). Many optimization problems can be converted to linear programming problems and be solved using these algorithms.

The problems with quadratic objective function with linear constraint are referred to as quadratic programming. There is a related problem of quadratically constrained quadratic programming, which does not impose linearity requirement on constraints.

The more general problem is that of convex optimization. As with other optimization problems, the objective is to minimize  $f_0(x)$ , subject to  $f_i(x) \leq b_i, i = 1 \dots m$ . The objective and constraint functions are convex, i.e.:

$$f_i(ax + by) \leq af_i(x) + bf_i(y), a + b = 1, a \geq 0, b \geq 0 \quad [2.16]$$

Linear constraints can be imposed as well:

$$a_i^T x = b_i, i = 1 \dots p \quad [2.17]$$

The least squares and linear programming problems are special cases of the general convex optimization problem. As with linear programming, there is no analytical solution for this class of problems, but there are reliable and efficient algorithms for solving them. Many problems can be transformed to convex problems in order to be solved more efficiently. The biggest advantage of convex problems is that any locally optimal point is globally optimal.

For the non-convex problems, there is an inherent compromise between the optimality of the solution and efficiency. Local optimization requires an initial guess and finds a point that minimizes the objective function nearby. It is fast and can handle large-scale problems. Finding the global solution requires iteratively solving convex subproblems and has complexity that grows exponentially with the size of the problem.

## Unconstrained Minimization

The optimization problems can also be classified into constrained and unconstrained, depending on whether constraints are imposed on the parameter vector  $x$ . The unconstrained optimization problem is simply a problem of finding a vector  $x$  that gives a local minimum to a scalar function  $f(x)$ .

This problem is solved iteratively, by producing a sequence of points  $x_k \in \text{dom } f: f(x_k) \rightarrow p^*$  where  $p^*$  is the local minimum of  $f(x)$ . An initial point  $x_0 \in \text{dom } f$  is provided to the algorithm.

Descent methods approach the minimum by picking the next point that results in a lower value of  $f(x)$  using the step direction and step size that depend on the properties of  $f(x)$  at the current point:

$$x(k+1) = x(k) + t(k)\Delta x(k) \quad [2.18]$$
$$f(x(k+1)) < f(x(k))$$

where  $\Delta x$  – step or search direction,  $t$  – step size

## Gradient-Based Methods

The gradient descent method uses the negative gradient as the step direction, based on the observation that a smooth function decreases the fastest in that direction:

$$\Delta x = -\nabla f(x) \quad [2.19]$$

$$x(k+1) = x(k) - t \nabla f(x(k))$$

The stopping criterion for the iteration is when the absolute value of step size becomes less than a predefined value  $E$ :  $|\nabla f(x)|^2 \leq E$ . That happens in the

vicinity of the function extremum,  $f(x)$  needs to be differentiable for this algorithm to work.

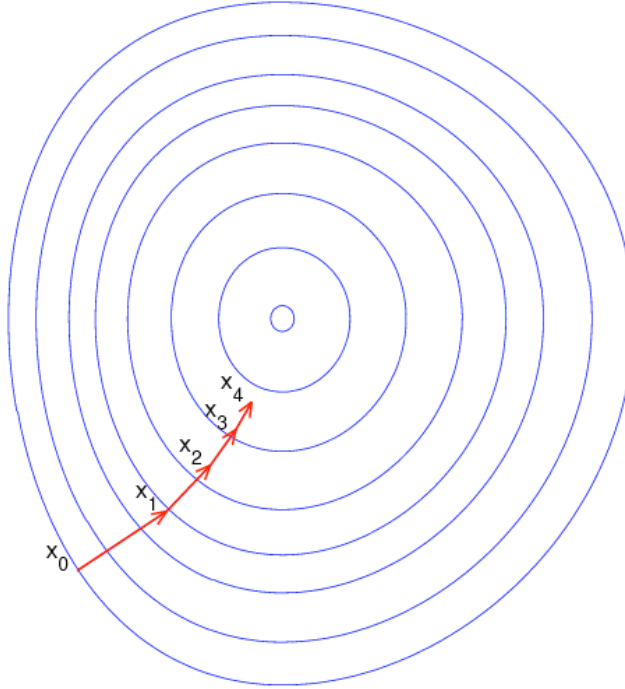


**Figure 2.17. Gradient descent.**

*Image created by Oleg Alexandrov, published under public domain at [http://commons.wikimedia.org/wiki/File:Gradient\\_descent.png](http://commons.wikimedia.org/wiki/File:Gradient_descent.png)*

The Newton's method achieves faster convergence than gradient descent by using the second derivative of  $f(x)$ . It does that by approximating  $f(x)$  as a quadratic function around  $x(k)$ . In one-dimensional case it can be expressed as:

$$x_{n+1} = x_n - \frac{f'(x_n)}{f''(x_n)} \quad [2.20]$$

This method requires the objective function to be twice differentiable.

The Newton method requires a Hessian matrix of second derivatives to be computed at each step of the iteration. Quasi-Newton methods estimate this matrix

by analyzing the gradient vectors. The gradient of the function, if not provided explicitly can be estimated based on the function values at the points nearby.

$$f(x_k + \Delta x) \approx f(x_k) + \nabla f(x_k)^T \Delta x + \frac{1}{2} \Delta x^T B \Delta x \quad [2.21]$$

where  $B$  is the approximation of the Hessian matrix.

There are multiple methods for iteratively updating the  $B$  matrix. One of the most widely used algorithms has been developed by Broyden, Fletcher, Goldfarb and Shanno and is referred as BFGS method. In this method,  $B$  is expressed as:

$$B_{k+1} = B_k + \frac{y_k y_k^T}{y_k^T \Delta x_k} - \frac{B_k \Delta x_k (B_k \Delta x_k)^T}{\Delta x_k^T B_k \Delta x_k} \quad [2.22]$$

### **Non-Gradient-Based Methods (Heuristics)**

When it is impossible to calculate or estimate the derivative (or gradient) of the objective function, the methods that rely on it would not work. That could happen if the objective function has breaks or bends. This problem arises if the cost function measures properties that are inherently discrete, such as a number of objects that satisfy some condition.

There is a number of algorithms for solving such problems, albeit not nearly as efficient as with the differentiable functions. These methods are referred to as metaheuristics. They do not make any assumptions about the objective function and search for the solution by searching the parameter space for the values that make the objective function lower. These algorithms, however, do not guarantee convergence on an optimal solution.

One of the widely used heuristic search techniques is the Nelder-Mead technique (38). It searches the parameter space using a "simplex" or an object of  $N+1$  vertices for  $N$ -dimensional space. For example for a 2D space, the simplex would represent a triangle.

At each step, the algorithm finds the worst point among the simplex vertices, i.e. the one that makes the objective function have the biggest value:

$$f(x_1) \leq f(x_2) \leq \dots \leq f(x_{n+1}) \quad [2.23]$$

Then, that point is compared to its reflection through the centroid of the remaining points.

$$x_r = x_0 + \alpha(x_0 - x_{n+1}) \quad [2.24]$$

If that point is better than the second worst ( $f(x_1) \leq f(x_r) < f(x_n)$ ), it can replace the worst one in the simplex.

If the reflected point is better than all the points in the simplex ( $f(x_r) < f(x_1)$ ), the algorithm tries to expand the simplex by stretching the simplex along the same line:

$$x_e = x_0 + \gamma(x_0 - x_{n+1}) \quad [2.25]$$

If the reflected point is not better than the second-to-worst points ( $f(x_r) \geq f(x_n)$ ), it might mean that there was a valley between the reflected point and the rest of the simplex, so the simplex is contracted along the same direction:

$$x_c = x_0 + \rho(x_0 - x_{n+1}) \quad [2.26]$$

Finally, if neither expansion nor contraction has been performed, the simplex is shrunk by moving all the points towards the best one:

$$x_i = x_1 + \sigma(x_i - x_1), i = 2 \dots n+1 \quad [2.27]$$

The algorithm terminates if the difference between the x values or between the function values in subsequent iterations becomes less than a pre-defined tolerance or if the algorithm exceed the predefined number of iterations. Nelder-Mead algorithm can handle discontinuity, but can converge on a local minimum.

### **Multi-Objective Optimization**

Many real-world problems involve two or more competing objectives. For example, in economics, it is desirable to achieve as much profit as possible while minimizing the cost of the product. A good solution would achieve a compromise between these objectives. The techniques for solving such problems are called multi-objective optimization or "Pareto" optimization algorithms.

The concept of Pareto efficiency comes from economics and refers to a solution where no one can be made better off without making someone else worse off. The solution to the multi-objective optimization problem is a set of Pareto points, or a Pareto frontier.

A common way to apply standard optimization methods to a multi-objective problem is to define an aggregate objective function. The function contains weighted contributions from the competing objectives. The optimal solution will depend on the values of the weight constants. This adds subjectivity to the algorithm, but allows precise fine-tuning. Problems could also arise if the Pareto frontier is not globally convex.

Other algorithms, such as Normal Boundary Intersections have been proposed for solving multi-objective optimization problems. They focus not on obtaining a single compromise solution, but on identifying an evenly distributed set

of Pareto points that give a good approximation of the complete set of solutions.

Evolutionary algorithms, which are a subset of meta-heuristic algorithms, have been also used to solve complex multi-objective problems.

# **Chapter 3. Development of Software for Prescription, Acquisition and Processing of MRSI Data**

## **Introduction**

The goal of this dissertation project was to develop, implement and validate techniques to automate the prescription of MRSI examinations, as well improve the coverage of the brain and consistency of prescription without compromising the quality of the data.

Implementing the automated prescription algorithms, described in the following chapters, and obtaining data with the new protocols required adding complex features to several software components. The MRSI pulse sequence was modified to add support for novel outer-volume suppression (OVS) schemes and an ability to load externally generated prescription geometry. Dualband radiofrequency (RF) suppression pulses were added to the pulse sequence to allow for more complex OVS configurations. The automated scan prescription software was integrated into the scanner user interface to be used during a patient examination. Data transfer, processing and visualization pipeline were modified to accommodate processing of the data, acquired with the new automated protocols. Development of those features and ensuring their seamless interoperability was a significant part of this dissertation work.

This chapter discusses the challenges in acquiring high quality MRSI data and describes the development the pulse sequences and scanner software to enable the

automated acquisition of 3D MRSI data. It focuses on important design choices and technical details of the implementation that may be of interest to those working on extending the functionality of MR scanners.

## Pulse Sequence Considerations

Acquiring high quality MRSI data is not easy. Many factors and limitations need to be considered and addressed in order to develop appropriate pulse sequences and protocols for MRSI. Most of the features of the MRSI pulse sequences are interrelated. That means that improving one aspect of acquisition may require a compromise in another. To achieve clinically acceptable results, a delicate balance between those factors must be found. Among those factors are:

- Fat. As mentioned earlier, fatty or lipid tissues are commonly found under the skin throughout the body, including the scalp. The ringing artifact from subcutaneous lipids affects the spectra within the brain, and, if not sufficiently suppressed, makes it impossible to quantify the metabolites of interest. At the same time, lipids may be present in necrotic tissues of a tumor. Their presence has been shown to be a potential biomarker for tumor malignancy (28). Lipid suppression methods have been discussed in detail in the previous chapter.
- Water. Water is the most prevalent MR-visible compound within the brain. MR signal of water molecules is a foundation of most of the MR Imaging acquisitions, but is a problem for MR spectroscopy. If not suppressed, the large water peak causes baseline distortions and obscures small signals at other resonances. Methods for water suppression were mentioned in Chapter 2.

- Signal to Noise Ratio. SNR measures how the intensity of the acquired MR signal compares to the level of the noise. The motion of electrons within the body, the imperfections within the coil and electronics of the scanner and the radio waves from outside the scanner are among the main factors, causing noise in the data. If the peaks of interest cannot be reliably detected above the noise floor, they cannot be accurately quantified. SNR is proportional to the square root of the total acquisition time and to the size of the voxel. Because of that, SNR could be improved by scanning the same tissue multiple times and averaging the results, or by using larger voxels. On the other hand, accelerating the acquisition or increasing the resolution leads to loss in SNR. Acquiring data with a multi-channel RF coils can also help improve SNR.
- Acquisition Time. Acquiring high-resolution data with large field of view requires long acquisition times. Accelerated techniques, such as echo-planar spectroscopic imaging, described in chapter 2 can accelerate the acquisition, but result in worse SNR of acquired data. A clinical exam consists of a number of anatomic, functional and metabolic imaging sequences and must take into consideration patient comfort and cost. Typical clinical exams are scheduled in 30 or 60 min slots, while clinical research exams can be up to 90 minutes long. The patient has to lie perfectly still during the acquisition of each image series, which is especially difficult in the case of longer acquisition times. Any motion during the scan can significantly compromise the data quality.
- Resolution. Achieving higher spatial resolution is desirable since it allows better characterization of the extent of disease and its heterogeneity. It also reduces the

ringing artifact of the subcutaneous fat. Increasing resolution adversely affects SNR and increases acquisition time.

- B0 inhomogeneity. Variation of the main magnetic field (B0) within a voxel leads to peak widening and loss of SNR. The oral and nasal cavities, ear canals and sinuses cause significant nonlinear variations of the local magnetic field, especially in the anterior and inferior parts of the brain.
- B1 variation. The power of RF from the excitation pulses varies due to the inhomogeneity of the transmit coil profile and attenuates within the tissue. This causes variation of the achieved flip angles and results in sub-optimal SNR, water and lipid suppression.
- Phase. Phase of the signal varies between voxels within the brain due to variation in the magnetic field. It also varies between the signal from different channels of a multi-channel receive coil. Consistent phase is needed for interpretation and quantification of spectra, and, in case of multi-channel data, to avoid SNR loss due to the signals from different channels canceling each other.
- Multiple channels. Combining the data from multiple channels significantly increases the SNR throughout the brain and, with the use of parallel imaging is able to reduce acquisition times. Both of these require phase and sensitivity profile information for each coil element for a given subject.
- Echo Time (TE) is an important parameter of spin-echo-based pulse sequences, as described in chapter 2. Shorter echo time allows to detect more metabolites, such as myo-inositol, glutamine and glutamate. It also results in higher water and lipid signals and uneven baseline from the contributions of the macromolecules.

- SAR. Specific Absorption Ratio reflects the heating of the tissue due to the RF energy deposited. Keeping SAR within the safe limits often requires limiting the number and power of RF pulses or increasing the repetition time, which, in turn, leads to the increase in the total acquisition time. This is especially a problem on the high-field scanners and when using complex RF pulses for excitation or suppression of water and lipids.
- Brain Coverage. The MRSI exam needs to cover the complete lesion and as much as possible of the apparently healthy tissue that may still exhibit signs of metabolic abnormality. Increasing the field of view results in longer acquisition times and increases the risk of lipid contamination and problems due to the inhomogeneity of the main magnetic field (B0) and radio-frequency excitation (B1). Achieving high brain coverage while using outer-volume suppression (OVS) to suppress the lipid signal requires complex OVS configurations with a large number of saturation bands.
- Prescription. MRSI acquisition is controlled by dozens of parameters, including placement of the selected volume and OVS bands, shimming currents, etc. Choosing optimal parameters that result in high quality data for a particular subject requires a skilled operator and can take a long time. Suboptimal prescription often results in poor data quality and incomplete coverage of the lesion. Automating the prescription while improving brain coverage, without sacrificing acquisition time, resolution or data quality are the main goals of this work.

## Pulse Sequence Development

Commercial pulse sequences allow both single voxel and 2D/3D MRSI.

Different versions of the pulse sequence are customized for acquiring data from brain, prostate and breast. The data is reconstructed on the scanner itself. For single-voxel datasets an image with the graphical representation of the spectrum is created. Multi-voxel reconstruction produces image files that encode spectral data within the pixel data for transmission and storage. Special software, available on the scanners and imaging workstations is required to visualize the spectral data. The reconstruction and processing parameters are hard-coded and cannot be customized.

Over the years UCSF researchers have added many features to the branches of the product pulse sequences. Among them were Very Selective Suppression (VSS) bands, BASING scheme for lactate editing, spectral spatial RF pulses, 2D-j technique to detect additional metabolites and accelerated acquisitions using reduced k-space, parallel imaging and echo-planar techniques. Some of these features have been incorporated by the vendor into the product sequence and are now available on clinical scanners around the world.

The software development toolkit is provided to institutions that have research agreements with the vendor. Pulse sequences are developed in a custom programming language that is preprocessed into C-code. The preprocessor expands macros, pulls sections of the code, specified by the "include" statements and generates two sets of source files: one for the Linux-based console computer and the other one for the embedded computers, responsible for pulse generation, data

acquisition and real-time control over the sequence being run. The toolkit also handles the conversion and transfer of variables and data structures between those systems. The executable and object files, produced from the C-code can be installed on the MRI scanner, running in a "Research" mode.

For my dissertation project I have developed a number of new features in the MRSI pulse sequence, including externally prescribed OVS bands, dualband VSS pulses, octagonal OVS scheme and externally prescribed PRESS box.

### **Externally Prescribed OVS bands**

The automated prescription algorithms were implemented as a software module, separate from the pulse sequence running the scan. This provided flexibility in the choice of programming language and computing resources. It also allowed the prescription software to use the anatomical images of the patient, acquired during the MRI/MRSI exam and to provide a user interface for visualization of generated prescription.

Development and implementation of an automated prescription of outer-volume suppression (OVS) bands has required the MRSI pulse sequence to support loading the geometric parameters of these bands from a file rather than from a graphic prescription.

The product pulse sequence had support for 6 fixed saturation bands at the edges of the ROI and up to 6 saturation bands, graphically prescribed by the operator. This was insufficient for implementing a robust OVS scheme. Hence the sequence was modified to include up to 16 additional VSS pulses. These pulses could

be used in combination with both the fixed and graphically prescribed saturation bands.

A user control variable, toggled by the operator on the scan prescription screen, controlled loading of the externally prescribed OVS band parameters into the pulse sequence. These parameters were saved by the prescription software as an ASCII text file with a name of "sat\_bands.dat" in a special directory on the scanner's hard disk and were loaded by the pulse sequence before the start of the acquisition.

Below is the example of the externally generated saturation band prescription file. The first line indicates the number of saturation pulses to use. Each subsequent line contains parameters of one saturation pulse. The parameters include  $\alpha$ ,  $\beta$  – Euler angles of the normal vector to the sat band,  $d$  – distance from origin to the mid-plane of the band,  $t$  – thickness of band,  $w$  – width of the pair of bands for dual-band pulses. If  $w = 0$ , a single-band pulse is used.

```
9
1.570796 -1.326038 121.171225 45.000000 0
1.570796 1.542745 65.054501 45.000000 0
1.570796 0.673211 63.006700 45.000000 0
1.570796 -0.234809 76.120524 45.000000 0
0.407685 1.570796 66.226700 45.000000 0
-0.390754 1.570796 83.598588 45.000000 0
2.733907 1.570796 64.848054 45.000000 0
3.532346 1.570796 82.210059 45.000000 0
1.570796 3.232481 38.891777 45.000000 0
```

*Example of the file format for OVS band prescription.*

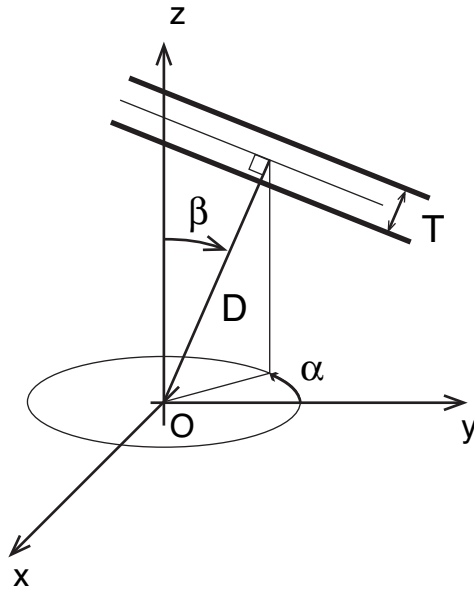


**Figure 3.1.** Parameters of a saturation band.

The scanner software operates with the coordinates in several coordinate systems. Coordinates in the patient coordinate system (L - left, P - posterior, S - superior) do not depend on the table position. The physical coordinate system has the origin in the isocenter of the magnet. If  $D$  is the distance from the origin to the sat band in the patient coordinate system, in the physical coordinate system it would be  $L = D + \cos(\beta) \Delta$ , where  $\Delta$  is the table position.

The scanner also supports multiple logical coordinate systems and allows "slice" rotation matrix to be loaded into the hardware. When gradient pulses are played out all the amplitudes are automatically converted into physical coordinates. For the externally prescribed saturation pulses, the matrix can be expressed as:

$$\begin{array}{ccc}
 \cos \alpha \cos \beta & -\sin \alpha & \cos \alpha \sin \beta \\
 \sin \alpha \cos \beta & \cos \alpha & \sin \alpha \sin \beta \\
 -\sin \beta & 0 & \cos \beta
 \end{array}$$

All the saturation bands become orthogonal to the Z axis in their respective logical coordinate systems. The logical Z gradient strength required to achieve the specified band thickness and the frequency offset to place the band at the specified distance from origin are then calculated.

Each OVS pulse is followed by a crusher gradient pulse, intended to dephase the excited spins. In the areas of saturation band overlap, the spins experience two or more sets of excitations and crushers. To prevent stimulated echoes in those areas, the X, Y, and Z gradients of the crusher pulses were made to follow offset cosine envelope patterns. This was based on the work by Henning et al. (34) and ensures that no two bands had exactly the same combination of crusher amplitudes.

## Dualband VSS Pulses

Achieving a selected volume of a complex shape requires many OVS bands. There is a limit, however, on the length of the OVS pulse train due the loss of effectiveness of the pulses with the increase of the delay between the pulse and the excitation. To create more bands with the pulse train of the same length, dualband pulses can be used. A single dualband VSS pulse can generate two parallel saturation bands.

Cosine-modulated dualband pulses were first implemented for brain 3D MRSI pulse sequence by Joseph Osorio (39), based on the work of Charles Cunningham and Adam Kerr in John Pauly's group at Stanford University. Multiplying a waveform by a cosine function results in doubling of the excitation profile after the Fourier transform:

$$FT(\cos 2\pi f_0 t) = \frac{\delta(f - f_0) + \delta(f + f_0)}{2} \quad [3.1]$$

The distance between the pulses is determined by the modulation frequency.

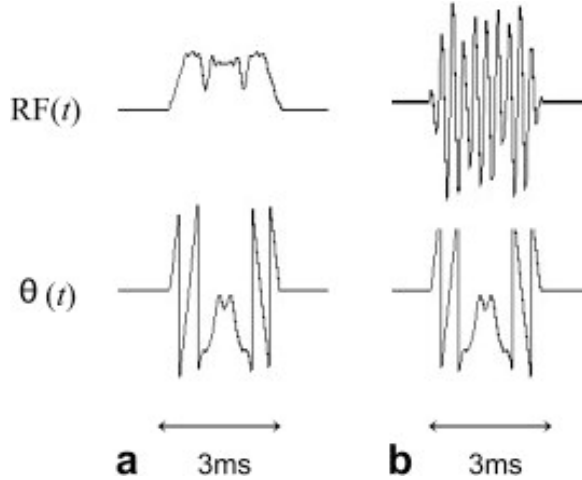


**Figure 3.2.** Cosine-modulated dualband VSS RF pulse.

(a) RF pulse without cosine modulation. (b) Cosine modulated VSS pulse.

Reprinted from Osorio et al. Design of cosine modulated very selective suppression pulses for MR spectroscopic imaging at 3T (39) with permission from Wiley.

In the previous work (39), the dualband pulses were implemented as a part of the fixed ROI-edge OVS scheme. In the present project, any of the 16 additional OVS pulses could be made dualband. This allowed for more flexibility in the design of the OVS scheme.

The drawback of the cosine-modulated VSS pulses is that they require double of the B1 of a single-band pulse to achieve the same flip angle. This could be achieved by doubling the amplitude of each pulse. This does, however, often lead to exceeding the peak power limit of the scanner's RF amplifier.

The necessary increase in  $B_1$  can be also achieved by stretching the pulse in time, while keeping the amplitude the same. While it negates some of the benefits of the dualband pulses, there is still a significant time savings due to the time required for crusher gradients and intervals between pulses.

Another approach to designing reduced peak-power dualband VSS pulses was presented by Adam Kerr in his 2009 ISMRM abstract (40). Nonlinear phase profiles for saturation pulses can be optimized by manipulating the roots of the  $B(z)$  polynomial (41,42) that describes the slice profile in an SLR-based RF design (43).

This approach allows dualband pulses to be designed with peak RF amplitude that is only increased by a factor of  $\sqrt{2}$ , compared to single-band pulses with the same parameters. On the other hand, it requires the complex RF design process to be performed after scan prescription. In the present work, the approach outlined in (40) was modified to allow for much simpler implementation into a pulse sequence.

The  $B_s(z)$  polynomial of an SLR pulse for exciting a single band is designed as described by A. Kerr (40). The filter has a ratio of passband to transition width of 15 with profile ripples  $(\delta_1, \delta_2, \delta_3)$  of (.007, .141, .003) as shown in figure 3.3a. The ripples  $(\delta_1, \delta_2)$  are chosen to give  $M_z$  in-slice ripple of 0.02 and out-of-slice ripple of 0.02, while the small  $\delta_3$  is required to prevent in-slice interference when a dualband pulse is formed.

An exhaustive search of root flipping zeros in the passband of  $B_s(z)$  is made to find which resultant RF pulse  $B_{1,s}(n)$ ,  $n=1\dots N$  yields the lowest peak amplitude in the worst-case dualband envelope  $|B_{1,d}(n)|/\max = |B_{1,s}(n)| + |B_{1,s}(N-n+1)|$ . The

dualband RF pulse is easily formed at scan time by independently modulating the RF pulses  $B_{1,s}(n)$  and  $B_{1,s}(N-n+1)$  to the desired frequencies with complex exponentials and then summing. Figure 3.3b shows the magnitude of the single-band RF pulse, while Figures 3.3c-d show the simulated saturation for a dualband pulse as well as the worst-case dualband envelope.

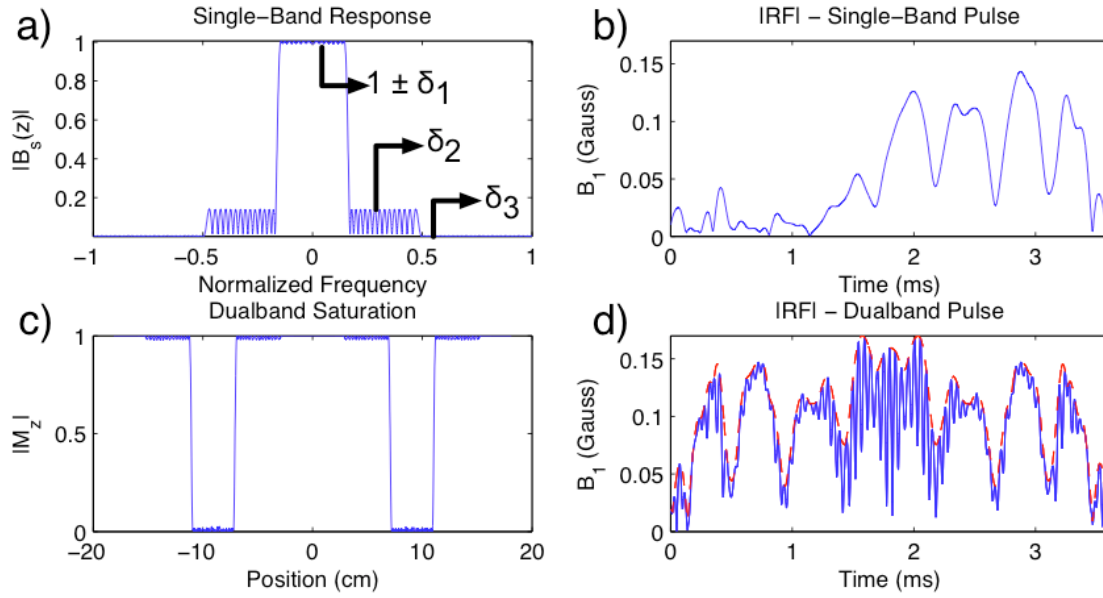


**Figure 3.3.** Exponential-modulated dualband VSS RF pulse.

(a)  $B_s(z)$  polynomial describing single-band excitation evaluated on unit circle. (b) Magnitude of single-band RF pulse. (c) Simulated saturation  $M_z$  profile for (d) a dualband pulse (blue) and the worst-case dualband envelope (red).

In their earlier work, Osorio et al. implemented octagonal OVS scheme using cosine-modulated dualband pulses that was used to acquire a stack of single slice MRSI datasets from the brain.

In this work, I implemented an octagonal scheme using 5 out of the 16 additional suppression pulses that were described earlier. The octagonal VSS scheme could be turned on in the pulse sequence with a control variable. In this

scheme the pulse sequence code placed 6 bands along the faces of the PRESS box and 4 bands, covering the corners. This approach allowed for flexibility in using the octagonal OVS with any combination of fixed, graphically prescribed and externally calculated sat bands.

## **Externally Prescribed PRESS box**

Loading the externally prescribed PRESS box works in a similar manner to loading the sat band configuration. When the operator toggles a control variable "read\_box," the pulse sequence looks for a file, called "press\_box.dat" in a special directory.

The file is expected to be in an ASCII text format and to contain 3 lines. The first line specifies the L, P and S coordinates of the center of the PRESS volume, separated by whitespace. The second line contains the X, Y and Z dimensions of the PRESS volume. The third line contains the rotation angles ( $\alpha, \beta, \gamma$ ) of the PRESS volume around L, P and S axis.

```
2.031139 -26.312620 17.098119
89.685463 124.225689 62.062219
0.090888 0.000000 0.000000
```

*Example of the PRESS box prescription file:*

The angles of rotation are used to calculate the slice orientation matrix that is loaded into the hardware during the excitation:

$$\begin{array}{lll}
 \cos \gamma \cos \beta & \cos \gamma \sin \beta \sin \alpha - \sin \gamma \cos \alpha & \cos \gamma \sin \beta \cos \alpha + \sin \gamma \sin \alpha \\
 \sin \gamma \cos \beta & \sin \gamma \sin \beta \sin \alpha + \cos \gamma \cos \alpha & \sin \gamma \sin \beta \cos \alpha - \cos \gamma \sin \alpha \\
 -\sin \beta & \cos \beta \sin \alpha & \cos \beta \cos \alpha
 \end{array}$$

The S coordinate of the PRESS box center determines the position of the patient table, so that the PRESS box ends up in the same axial plane as the magnet isocenter. The coordinates of the PRESS box center are then converted to the logical coordinate system using the table position and the rotation matrix, calculated earlier. They are used to determine the center of the field of view by modifying the offsets for the phase encoding gradients.

## Automated Prescription Software on the Scanner

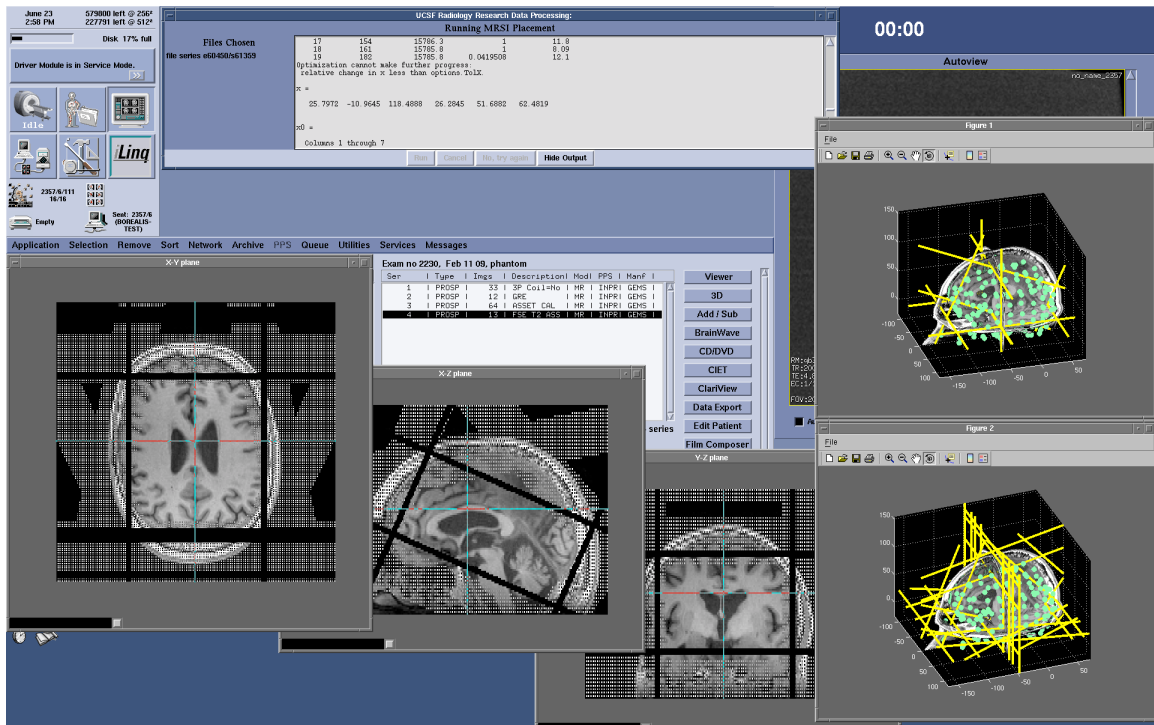


**Figure 3.4.** Automated prescription software running on the scanner console.

The automated prescription software relies on a custom computing infrastructure that was developed in our laboratory by Jason Crane. The application, implemented in Matlab, is compiled into an executable for the Linux operating system and installed on the scanner console computer.

Pressing one of the custom tool buttons on the scanner console invokes a "More Software" menu that lists the research software packages installed on the scanner. A custom Data Browser graphical user interface (GUI) is used to select images that are required for the automated prescription software to run. This tool prompts the user to select an image series in the scanner "Browser" and allows the user to specify options for running the custom software. While the software is running, the console output is displayed within the Data Browser window. If the software encounters an unresolvable problem, the Data Browser provides the user with diagnostic information about the problem. The software being run can display its own GUI for interaction with the user.

Our software library also provides an option to run the application on the scanner host machine, on its Volume Reconstruction Engine, or on the department's high-performance computing grid. In the latter case, the library handles copying image data to and from the scanner file system. If the application generates images, these can be imported into the scanner database and become part of the patient exam.

The automated prescription software uses custom routines to visualize image data and the configuration of OVS bands and PRESS volume in 3D during optimization. These allow the user to see the changes to the prescription while the algorithm is working. For the final review of the prescription, a 3D image volume is generated with OVS bands and PRESS volume embedded into the pixel data. It is displayed using an interactive 3D visualization tool OrthogonalSlicer (L. Balkay, Univ. of Debrecen, Hungary) that allows the user to scroll through axial, sagittal and

coronal slices of the image volume. The application generates OVS and PRESS prescription files that are read by the pulse sequence and subsequently transferred from the scanner together with the spectroscopy raw files.

## **Data Transfer**

The vendor's software supports automated transfer of MR images via the network from the scanner to one or more DICOM image archives. For raw data files, a custom script that periodically checks for the creation of new raw files and copies them to the research data archive is installed on the scanners at our institution.

The raw file header does not provide sufficient information for reconstruction and visualization of datasets, acquired with automated prescription. For instance, it has no records of the coordinates of additional OVS bands and does not contain information on which fat suppression features were used.

To preserve a record of the pulse sequence configuration, a routine was added to the pulse sequence to save the values of all control variables to file, based on the code, distributed by V. Ramanan (University of Toronto). The raw file transfer script was modified to enable transfer of those files, the OVS and PRESS box prescription files together with the raw files, containing spectroscopic data.

## **Shimming**

The product MRSI pulse sequence supports manual linear shimming and automatic linear shimming. Additionally, there is an option to turn off linear shimming and run a separate high-order shimming sequence. It performs a fast spiral proton-density acquisition of a large field of view within the scanner bore and launches the shim optimization GUI. The user can then manually outline the area

over which the shim would be optimized. There is an option to load the parameters of a previously prescribed MRS ROI, change the shape of the ROI and tilt the ROI around the RL axis. After calculating the shim, the software displays the predicted root mean square variation of the main magnetic field and allows the calculated shim currents to be downloaded to the hardware.

To further automate the shimming process, I have added the "Load Oblique ROI" button. It works similarly to "Load MRS ROI," but loads the PRESS box coordinates from the prescription file, generated by the "MRSI Placement" software. It also sets the oblique angle in the shimming routine to that of the MRSI prescription and sets the ROI shape to "Oval." If necessary, the operator has an option to adjust the shim ROI after it has been loaded.

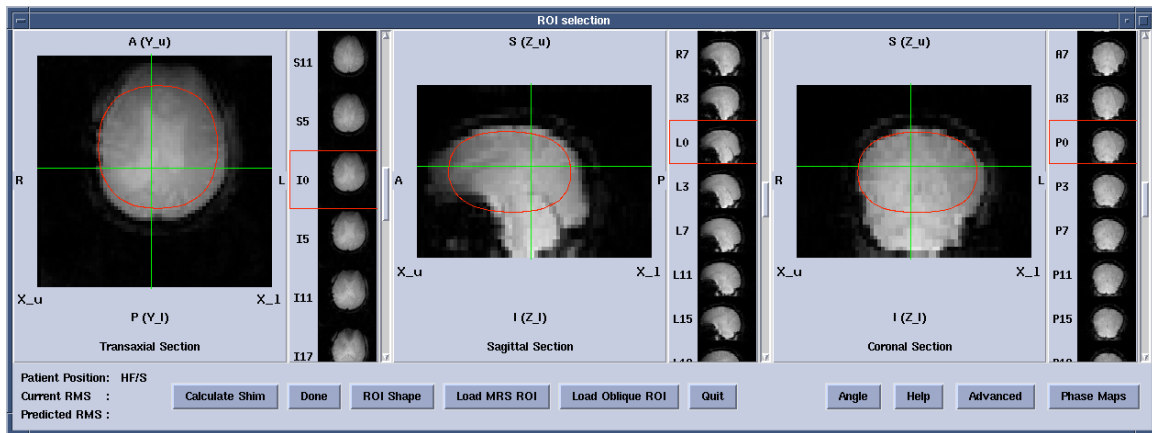


**Figure 3.5.** Shim GUI with "Load Oblique ROI" feature.

## Data Processing and Visualization Pipeline

Our laboratory uses an advanced data processing pipeline to reconstruct, process, quantify and visualized MRSI data (15,16,44). This pipeline was developed over the years and consists of a number of software components that are linked

with batch scripts. A high performance computing cluster is used for concurrent processing of multichannel data. The pipeline allows the operators to easily process datasets, acquired with standard parameters, while allowing the researchers to experiment with novel acquisition and processing technique. The data processing pipeline had to be modified to allow the processing of the oblique 3D MRSI datasets with extended coverage that are acquired with the automated protocols.

The data processing script has first to detect the type of OVS scheme that was used. This is necessary because the parameters of the additional OVS bands were not recorded in the raw data header. The script parses the control variable file, produced by the pulse sequence and looked for the variables, controlling octagonal selection and externally prescribed OVS bands.

If an octagonal OVS scheme is detected, additional bands are generated, based on the same algorithm that the pulse sequence used, and added to the data descriptor file. If externally prescribed bands were used, their parameters are converted from the saturation band prescription file, transferred from the scanner, and are added to the data descriptor file.

Unlike conventional MRSI acquisitions, where the PRESS volume rarely extends beyond the brain tissue, automated MRSI protocols use a much larger PRESS box that usually overlaps with the lipid area, covered by the saturation bands. Reliable quantification of metabolites requires that those areas be excluded from analysis. For that purpose, the processing script generates masks of the PRESS volume and of the area, not covered by the OVS bands. Those masks are combined to

a final voxel mask that is used to select the voxels, used for metabolite quantification.

Finally, the new protocols required changes in the visualization software, to be capable of rendering datasets with oblique orientation and large number of OVS bands. Correct rendering of the OVS bands is necessary for the radiologists to determine whether missing or attenuated peaks are due to the disease, effects of therapy or due to outer-volume suppression. Based on those requirements, the SIVIC visualization application (17) was adopted for visualization of MRSI data and generation of secondary capture images for radiological interpretation.

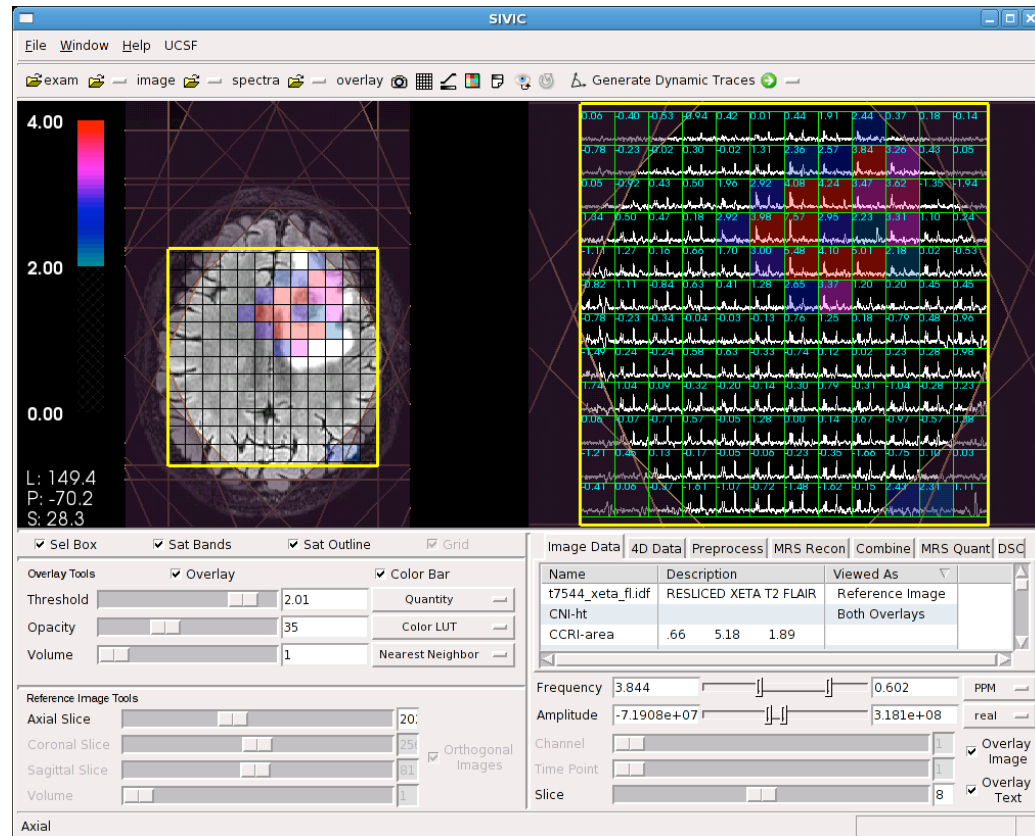


**Figure 3.6.** SIVIC software showing an MRSI dataset, acquired with automated prescription.

The work on data processing was performed in close collaboration with Dr. Sarah Nelson, who developed most of the utilities for processing of imaging and spectroscopy data, Dr. Jason Crane and Beck Olson, who developed and maintained software and scripts for data processing and visualization.

# **Chapter 4. Automated Saturation Band Placement**

This chapter is based on the journal article titled "Improved Spatial Coverage for Brain 3D PRESS MRSI by Automatic Placement of Outer-Volume Suppression Saturation Bands," published in the Journal of Magnetic Resonance Imaging in 2011 (1).

## **Introduction**

Proton Magnetic Resonance Spectroscopic Imaging (MRSI) is an important tool for diagnosis and evaluation of neurological diseases. MRSI data have been used for characterization of disease state, prediction of disease progression, treatment planning and evaluation of response to therapy (45-52). In particular, it has been shown that MRSI can detect the spatial extent of brain tumor more accurately than conventional T1 and T2-weighted MRI pulse sequences (15).

Excitation of subcutaneous lipids has been a major problem in 3D brain MRSI that has limited the coverage obtained. In the head, metabolites of interest, Choline, Creatine, Lactate and N-Acetyl-Aspartate (NAA) appear in concentrations on the order of  $10^4$  smaller than that of water or subcutaneous lipids (fatty tissues under the skin). If subcutaneous lipids are excited, a “ringing” artifact may appear in voxels within brain tissue due to side-lobes of the point-spread function of the excited protons (53).

Current MRSI protocols commonly use Point Resolved Spectroscopy (PRESS) volume selection, where a rectangular excitation volume results from an intersection of 3 infinite slabs, orthogonal to each other. The rectangular shape of the volume of interest requires that the region being excited is kept relatively small

in order to avoid artifacts from the subcutaneous fat and sinuses. This limits the areas that can be evaluated and means that some metabolically abnormal areas may be missed.

Several methods to suppress the subcutaneous lipid signal have been used in the past. Inversion recovery can be used to reduce the lipid signal by discriminating the tissues based on T1 relaxation times (25). This method, however, negatively affects the SNR of the acquisition (26). Other methods (12,21) use frequency-selective pulses to suppress the signal around the lipid resonance frequency. All those methods not only suppress the subcutaneous lipid signal, but also signal from the lipids within the brain. This is not desirable, since lipid in the tumor is a valuable biomarker in diseases, such as glioblastoma multiforme (28).

Manually placed sat bands are used to further reduce the lipid excitation. A sat band can eliminate most of the MR signal from a slab in space by excitation with radio-frequency (RF) pulses, such as the Very Selective Suppression pulses (VSS) (31), in the presence of slice-selection gradients and then de-phasing excited spins using crusher gradients. When PRESS excitation is performed, the area under the sat band cannot be excited any more until its longitudinal magnetization recovers. Manual placement of these sat bands is time-consuming and depends on the skill of the operator. Thus, it is hard to ensure consistently good placement of the sat bands, which is necessary to get useful MRSI data. This is one major reason why MRSI is currently not widely used in a clinical setting.

To improve coverage of the brain and to simplify prescription of 3D MRSI, we have developed a technique for automated optimization of sat band position and

orientation that simultaneously maximizes coverage of subcutaneous fat by the sat bands and minimizes the portion of brain tissue that is suppressed. This allows the prescription of a much larger PRESS box and provides MR spectra from a significantly larger volume of the brain. In this study we examine the performance of this technique.

## Methods

### Overview

The technique that was developed included the acquisition of a volume of anatomic images from the head with high lipid/tissue contrast, obtaining brain and lipid tissue maps, calculation of optimal sat band placement to cover the lipids in that image volume and integration of those parameters into the spectroscopy pulse sequence.

To test the performance of the automatic sat band placement and reproducibility of the results in controlled experimental setup, data were acquired from 3 healthy volunteers (Table 4.2), each receiving two exams on different days, performed by different operators. Each exam contained 2 MRSI acquisitions: one with manually prescribed sat bands (STANDARD protocol, Table 4.1) and one with automatic sat band placement (AUTOSAT+OCTAGONAL protocol).

To evaluate the technique as part of a clinical protocol, data were collected from 29 patients with brain tumors (Table 4.2), often acquiring two datasets per patient exam: one with automatic sat band placement and one without, for comparison. All subjects provided informed consent as approved by the Institutional Review Board (IRB).

## Image Acquisition

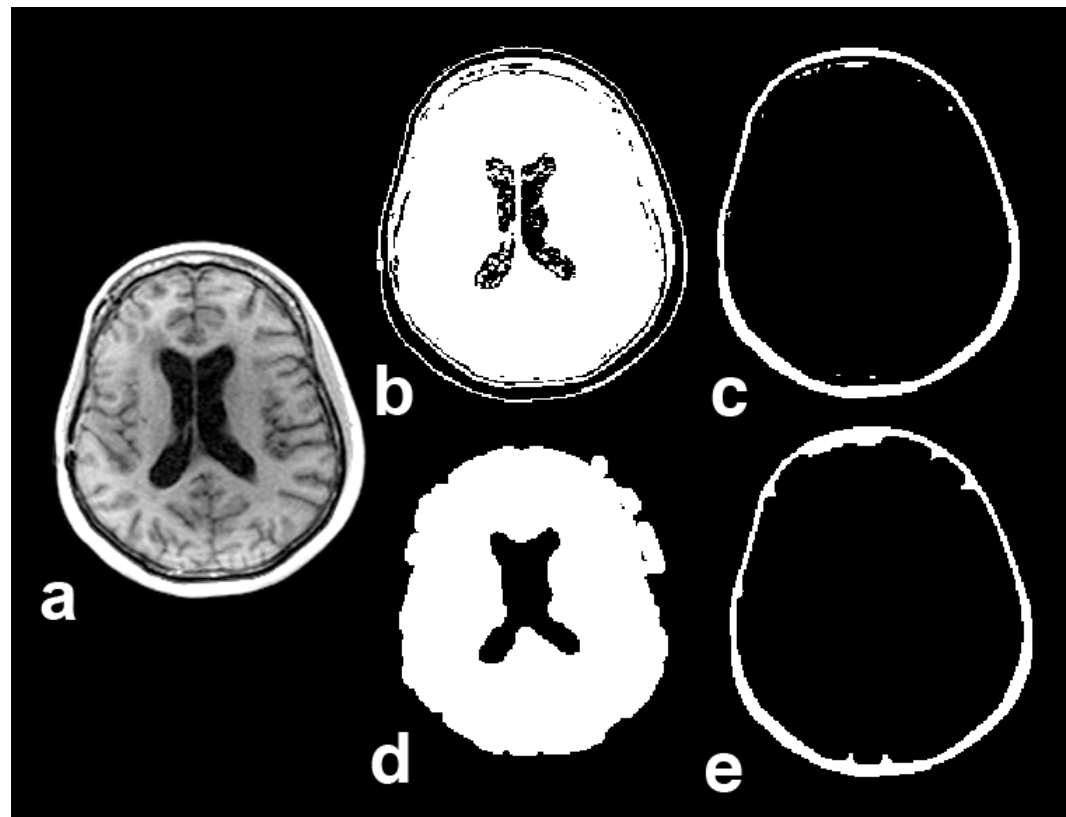


**Figure 4.1.** Anatomical image acquisition and processing.

(a) One slice from acquired image series with high lipid-brain contrast used for saturation band placement calculation; (b, c) initial masks of segmented brain and fat; (d, e) brain and fat masks after post-processing.

T1-weighted spoiled gradient echo axial image series (Fig. 4.1a) was obtained (flip angle = 20°, TE = 2.1 ms, TR = 4.5 ms, acquisition matrix: 256x160, FOV: 240x150 mm slice thickness = 3 mm, 92 slices,  $T_{\text{acq}} \approx 1$  min) on a 3T MR scanner (GE Healthcare, Waukesha, WI, USA). Acquisition parameters were chosen to achieve maximum contrast between subcutaneous lipids and brain tissues. Images were automatically downloaded from the scanner to a separate computer,

running Linux operating system for post-processing. Only the lowest 64 slices were used in the analysis since wrap-around artifacts from the neck were present in the top slices above the head.

### **Automated Sat Band Placement**

Image processing and saturation band optimization algorithms were implemented in Matlab (The MathWorks, Natick, MA, USA). Lipid and brain tissue masks were generated using k-means clustering with k=3 (Fig. 4.1 b, c). K-means clustering is an iterative algorithm that aims to partition a given set of data (in our case, pixel values) into k clusters (e.g., air, brain tissue, lipids) by trying to minimize the distances between data points and cluster centroids (54). The masks were post-processed using morphological closing and opening to remove segmentation artifacts (Fig. 4.1 d, e). To reduce the computation time their resolution was decreased by a factor of 3 in X and Y directions. While more advanced algorithms could obtain more precise segmentation, this simple approach was chosen to achieve acceptable calculation time. Sat band placement algorithm required only a general shape of the brain and lipid layer to work robustly.

Position, orientation and thickness of 9 saturation bands were calculated to achieve optimal lipid coverage. Placement of each band was defined by the following parameters:

$d$  – distance from origin,

$t$  – thickness,

$\alpha$  – rotation angle around Z axis of a normal vector to the sat band plane,

$\beta$  – angle between the normal vector and Z axis.

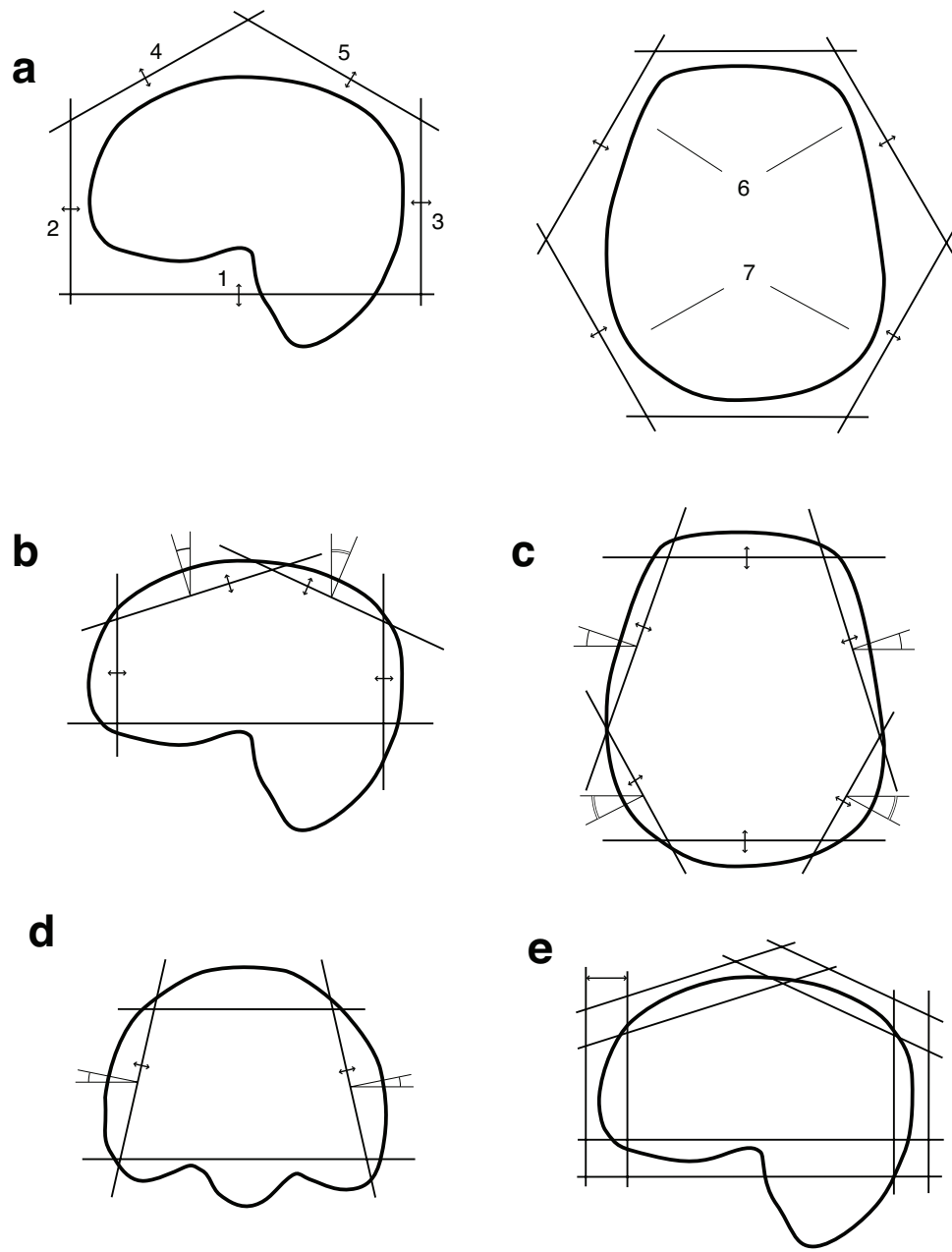


**Figure 4.2.** The sequence of optimizations to obtain the saturation band prescription  
 (a) the distances to individual sat bands were optimized in the order, indicated by the numbers; (b) optimization in the sagittal plane; (c) optimization in the axial plane; (d) tilt angle and distance optimization for side bands (first anterior ones, then posterior ones); second sagittal optimization (not shown); (e) optimization of thickness of individual bands.

The bands were initially placed at the same distance from the center of the head in the following configuration: one band horizontally below the head, six bands forming a hexagon around the head and two bands above the head, tilted 30° in the anterior and posterior directions (Fig. 4.2a).

A cost function, similar to that in (55), was defined to measure the quality of any given sat band configuration for a given image dataset:

$$f = -w_f N_f + w_b \cdot N_b + w_a \cdot N_a + w_d \cdot d \quad [4.1]$$

where:

$w_f, w_b, w_a, w_d$  – weights,

$N_f, N_b, N_a$ , - approximate the number of fat, brain, air pixels, covered by the bands, as described below,

$d$  – measure of distances of all bands from origin.

Intuitively, this function reached its minimum when the sat bands covered most of the lipid, but as little brain tissue and air as possible. The distance term was added for regularization to discourage the configurations where the sat bands were placed far from the origin.

The cost function, as described above, was not continuous; there was a step whenever a sat band started covering a new pixel or stopped covering a pixel that was covered earlier. Non-continuous functions cause problems in optimization when the step size is small. To overcome this,  $N_f$ , which approximated the amount of lipid tissue, covered by sat bands, was redefined as:

$$N_f = \sum_{p_i \in F} \min \left( 1, \sum_j r(p_i, s_j) \right) \quad [4.2]$$

where  $F$  is a set of fat pixels in the image and  $r(p_i s_j)$  was a piecewise-linear function whose value was defined as follows: 0 if pixel  $p_i$  is far outside sat band  $s_j$ , 1 if it was deep inside the sat band; and interpolated linearly between 0 and 1 when the pixel was within distance  $\delta$  of the sat band edge.  $N_b$  and  $N_f$ , which approximated the volume of brain tissue and air, covered by sat bands, were redefined similarly.

To find the optimal sat band placement the algorithm iteratively searched for parameters that minimized this cost function. The Nelder-Mead simplex method was chosen since it did not impose a requirement that the cost function be differentiable.

Due to the large number of degrees of freedom, simultaneous optimization of all parameters was impractical. Instead, optimization was done in several iterations on subsets of parameters (Fig. 4.2). During each step values of some parameters remained fixed, while other parameters were allowed to change to minimize the cost function. The optimum parameters, obtained in each step served as initial values for the next one. The sequence of optimizations included:

- 1)  $d$  (distance from origin) of individual sat bands (Fig. 4.2a);
- 2)  $d, \beta$  of the bands, orthogonal to the sagittal plane (Fig. 4.2b);
- 3)  $d, \alpha$  of the bands, orthogonal to the axial plane (Fig. 4.2c);
- 4)  $d, \alpha, \beta$  of the same bands (Fig. 4.2d);
- 5) repeat of step 2;
- 6)  $t$  (thickness) of individual bands, in the same order as in step 1 (Fig. 4.2e).

For each stage, the weights were tuned to ensure the fastest convergence. To further reduce the number of parameters to optimize, the assumption was made

that the problem was symmetrical in the right-left direction, so that a single parameter could control the distance or orientation of up to two symmetrical saturation bands at the same time. The calculated parameters were written to a file and transferred back to the MRI scanner host computer.

### **MRSI Pulse sequence**

This was modified to add up to 16 additional saturation pulses that could be controlled by externally generated prescription file, as described in chapter 3. The parameters for all saturation bands were read from the file and used to calculate gradient amplitudes, frequency offsets and rotation matrices for saturation pulses. All saturation bands (fixed, manually prescribed and automatically-prescribed) used VSS pulses (31) with the following parameters: nominal  $B_1$ : 0.116 G, pulse width: 3.0 ms, bandwidth: 5868 Hz. VSS pulse flip angles started at  $91.5^\circ$  for the last VSS pulse and increased by  $1.5^\circ$  for each earlier pulse, as implemented in the vendor pulse sequence, to compensate for T1 relaxation and minimize the longitudinal magnetization of saturated areas at the start of PRESS excitation. Cosine modulation could be turned on for any of the 16 additional pulses to achieve two parallel saturation bands from one pulse. This was used to implement octagonal selection within the pulse sequence using 6 saturation pulses (4 cosine-modulated, 2 regular) by automatically placing the saturation bands (width = 4 cm) at the edges of the PRESS box and over the corners of the PRESS box in the axial plane (Fig. 4.4, purple) (39).

## MRSI Acquisition

MRSI data were acquired using a commercially available 8-channel head coil (isotropic nominal voxel size 10 mm, TE = 144 ms, TR = 1100-1500 ms) with an EPSI flyback sequence (10). Raw data were transferred to a Linux workstation, then reconstructed and processed offline using an approach described previously in (15,16). Data from each channel was processed separately with 4Hz apodization, FFT in spatial and frequency dimensions, phase and frequency corrections, residual water and baseline removal. Data from all channels was combined using weights, obtained from low-resolution proton-density images.

The following acquisition protocols were used to acquire patient data (see table 4.1).

### 1. Standard MRSI (STANDARD)

This protocol was previously used for obtaining routine clinical and research brain patient exams. Six fixed sat bands with a width of 40 mm were implicitly applied by the pulse sequence at the superior, inferior, left, right, anterior and posterior edges of the PRESS box. PRESS box (SI dimension: 40 mm) was prescribed by the operator to cover the tumor and a portion of healthy brain tissue, while avoiding subcutaneous lipids as much as possible. Six additional sat bands were manually prescribed at the sides of the PRESS box to further suppress the signal from subcutaneous lipids. The OVS bands were rotated or rearranged to improve suppression in areas where PRESS box was located close to the lipids, according to operator's skill and experience. J-difference lactate editing scheme with dual BASING pulses (13) was used to provide summed data for Cho, Cre, NAA, lipids and

difference data for lactate (not used in the current study, but needed for the clinical protocol). This scheme required two excitations for each k-space point, resulting in an acquisition time of 9 min.

#### *2. MRSI with octagonal selection (OCTAGONAL)*

Octagonal selection (39) was used in place of fixed ROI edge sat bands to provide additional suppression of signal at the corners of the PRESS box. The operators were instructed to allow the corners of the PRESS box to extend over the lipid layer, while ensuring that those corners were covered by one or two additional manual sat bands.

#### *3. MRSI with automatically generated sat band placement (AUTOSAT)*

The PRESS box (SI dimension: 60 mm) was prescribed to cover as much of the brain as possible, with corners that often extended outside the brain. Operators used the images that overlaid the automatically placed sat bands over the brain anatomy to put the PRESS box over the area, enclosed by the sat bands. The matrix size was increased to 18x18x16 to accommodate the larger PRESS box. Fixed sat bands were implicitly placed at the edges of the PRESS box by the pulse sequence and there were 9 automatically optimized sat bands applied. Acquisition time was 6.5 minutes with one excitation per k-space point.

#### *4. MRSI with automatically generated sat band placement and octagonal selection. (AUTOSAT+OCTAGONAL)*

This was the same as option 3 but with octagonal selection instead of fixed sat bands.

	STANDARD	OCTAGONAL	AUTOSAT	AUTOSAT+ OCTAGONAL
Fixed ROI-edge sat bands	✓		✓	
Manually prescribed sat bands	✓	✓		
Octagonal selection		✓		✓
Automatically prescribed sat bands			✓	✓
FOV (cm)	16x16x16	16x16x16	18x18x16	18x18x16
Lactate Editing	✓	✓		
TR	1104	1134	1500	1500
T <sub>acq</sub> (min)	9	9	6.5	6.5
Slices in PRESS box	4	4	6	6

**Table 4.1.** 3D MRSI acquisition protocols that were compared in this study.

*STANDARD = standard lactate edited MRSI, OCTAGONAL = lactate-edited MRSI with octagonal selection, AUTOSAT = MRSI with automatically generated sat band placement, AUTOSAT+OCTAGONAL = combination of automatic sat band placement and octagonal selection*

## Data Analysis

The data were analyzed to determine whether the new technique allowed increased coverage of the brain and whether the acquired data had similar quality to the data obtained with the standard protocol.

To determine the coverage volume, masks of PRESS volume and sat bands were generated using the parameters, extracted from the MRSI raw files and sat

band prescription files. The coverage volume of an MRSI acquisition was defined as the number of 1cc voxels that lied within the PRESS box, but not in the areas, suppressed by sat bands. A voxel was considered to be suppressed by a sat band if more than 50% of its volume was within a sat band.

To quantify the quality of data and the amount of lipid contamination, peak height, linewidth and metabolite ratios of choline, creatine, NAA and lipid peaks were calculated within the healthy brain tissue (defined by white-matter mask, obtained with FMRIB's Automated Segmentation Tool, FAST (56)) based on predefined peak descriptor files that were adjusted using frequency correction parameters. Noise level was determined from the variance of the signal at the lower ppm end of the spectra. To correct for differences in protocol parameters, SNR efficiency values were calculated using total acquisition times and repetition times for each protocol and metabolite T1 relaxation times, estimated earlier (57,58). Mean, median values and pooled variances were calculated for each of the protocols that were compared.

To measure reproducibility of the results, the two exams from each volunteer were aligned to the same coordinate system using software, developed in or laboratory. For each pair of exams of the same subject, the overlap volume was calculated as the intersection of the volumes, covered by the AUTOSAT +OCTAGONAL acquisitions. Metabolite ratios were calculated within the volume, defined as intersection of the covered volumes of all 4 datasets of the same subject.

## Results

Figure 4.3 shows an example of a standard 3D MRSI dataset. Fixed ROI edge sat bands are shown in gray and manually prescribed sat bands in green. The PRESS box is 7x8x4 cm. Figure 4.4 shows an example of a dataset with octagonal selection, using cosine modulated sat bands (purple). Manual sat bands are shown in green. The PRESS box was made larger (10x10x4) due to better suppression in the corners. Figure 4.5 shows a dataset with automatic placement of sat bands (orange) and octagonal selection (purple). The prescribed PRESS box was 10x14x6 cm.

To quantify the observed improvement in coverage in patients, the results from the protocols were compared to those from the standard clinical 3D MRSI protocol. Table 4.3 shows mean, median and standard deviation for coverage volumes, metabolite signal-to-noise ratios (SNR), linewidth and metabolite ratios. Mean coverage for AUTOSAT protocol was 621.8 cm<sup>3</sup> (s.d. = 121.93 cm<sup>3</sup>), compared to 227.67 cm<sup>3</sup> for STANDARD protocol (s.d. = 30.86) – a 2.7 fold improvement. Pairwise coverage and average metabolite SNR of protocols with automatic and manual prescriptions for exams that had two MRSI acquisitions are shown on figure 4.6. In every case automatic prescription resulted in a larger coverage volume, while the average SNR values were consistent within each exam.

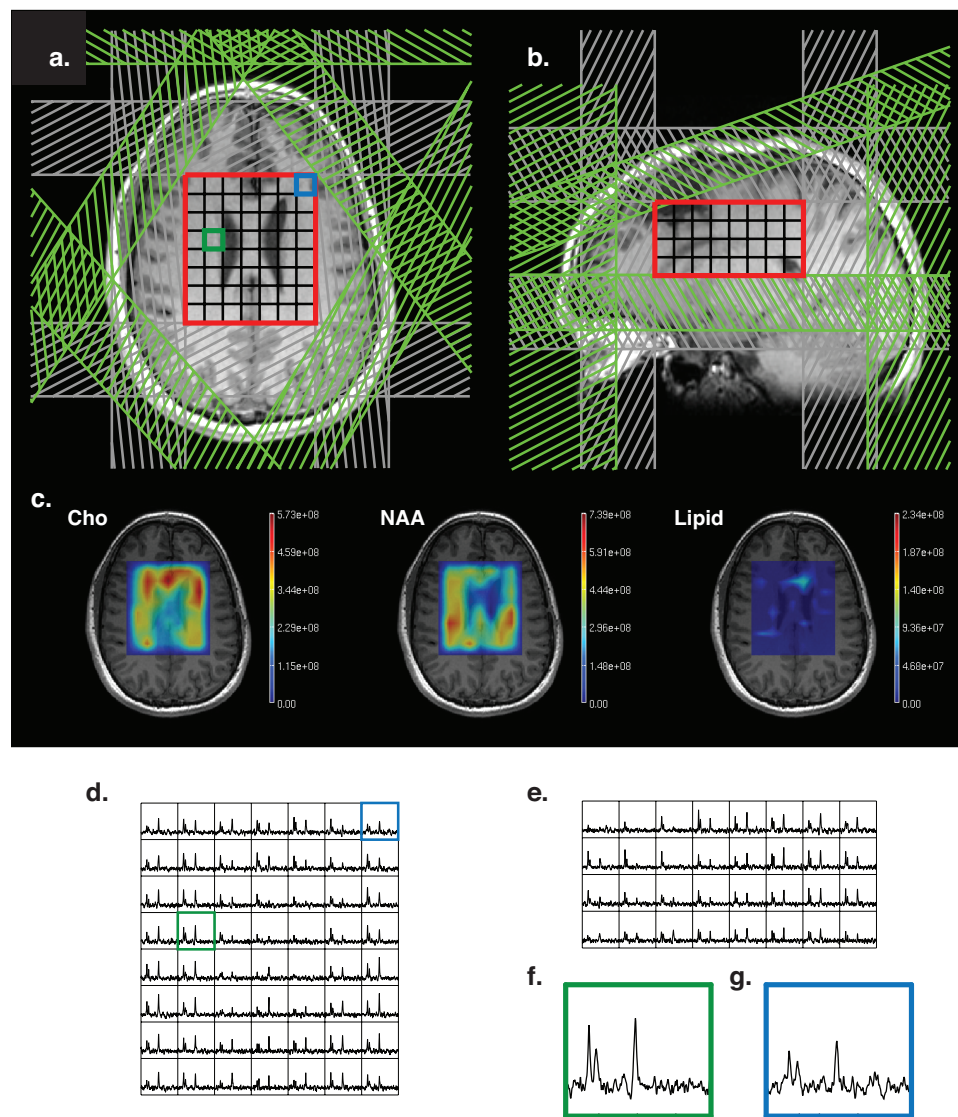


**Figure 4.3.** MRSI dataset acquired with STANDARD protocol.

(a, b) Standard MRSI prescription with sat bands (gray) at the edge of the PRESS volume (red) and manually prescribed sat bands (green); (c) metabolite maps, overlaid on the anatomical images; (d, e) axial and sagittal slices through 3D MRSI data; (f, g) sample central (green) and periphery (blue) voxels (location is shown in (a) and (d)).

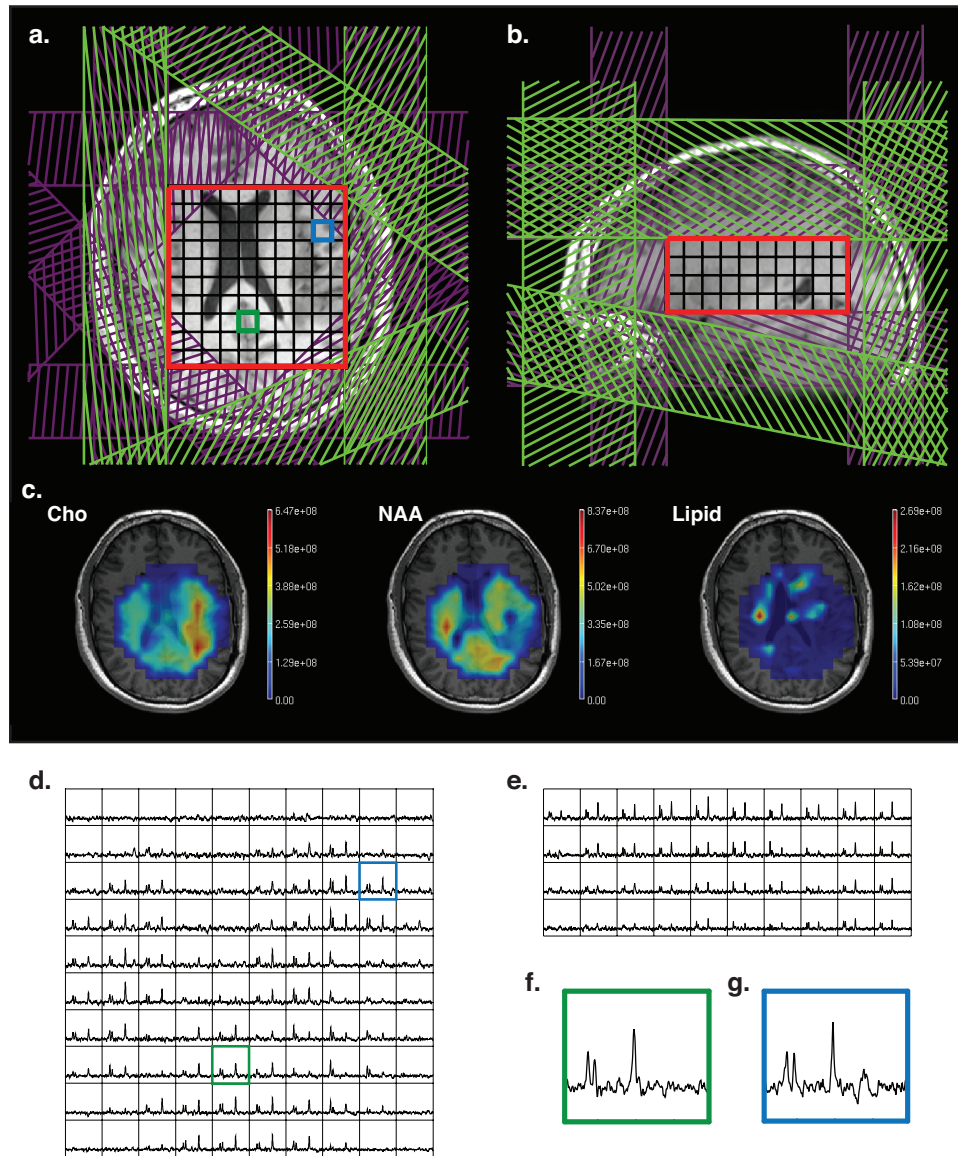


**Figure 4.4.** MRSI dataset acquired with OCTAGONAL protocol.

(a, b) MRSI prescription with octagonal VSS sat bands (purple) and manually prescribed sat bands (green). PRESS volume is shown in red; (c) metabolite maps, overlaid on the anatomical images; (d, e) axial and sagittal slices through 3D MRSI data; (f,g) sample central (green) and periphery (blue) voxels (location is shown in (a) and (d)).

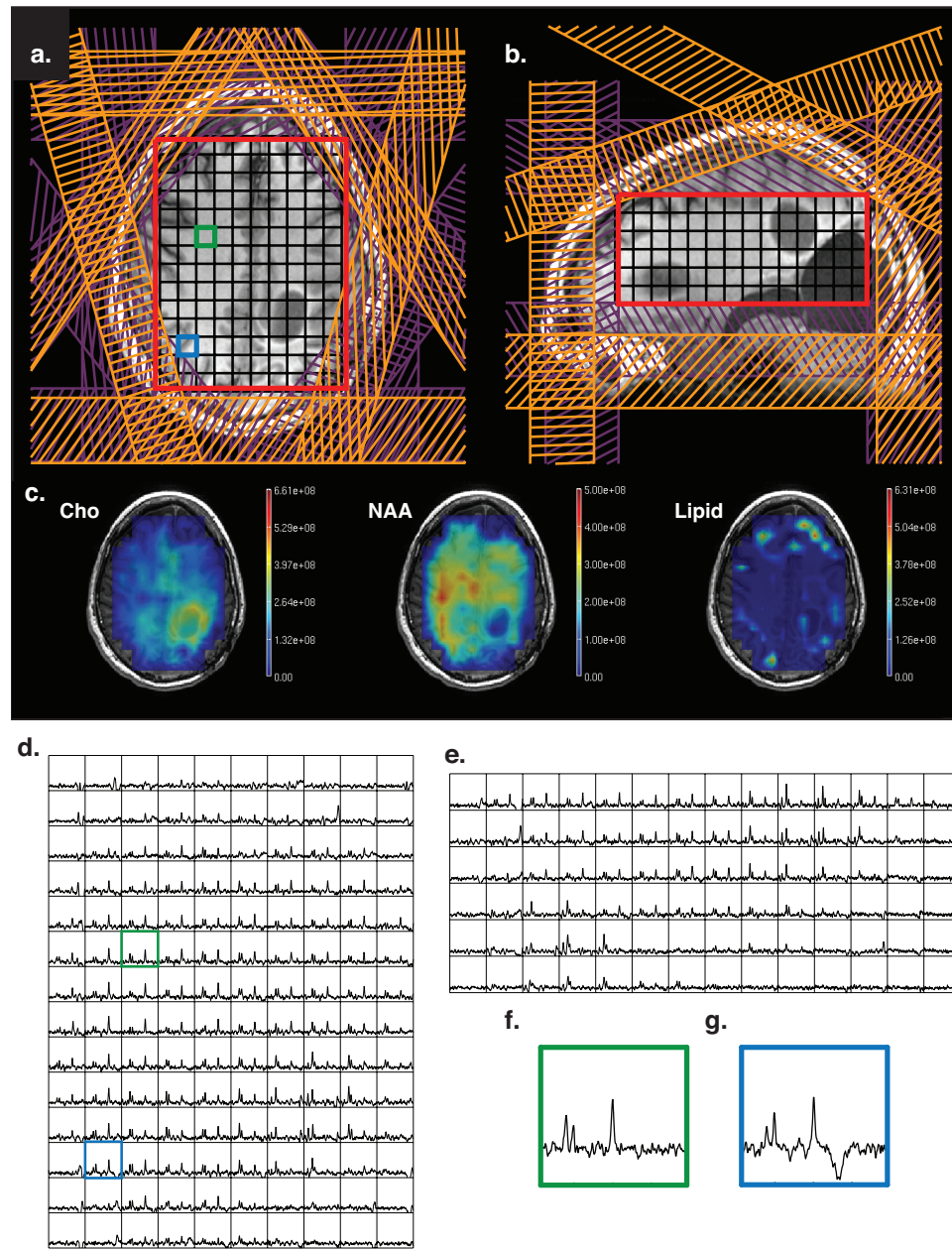


**Figure 4.5.** MRSI dataset acquired with AUTOSAT protocol.

(a, b) MRSI dataset with automatically prescribed sat bands (orange), PRESS volume in red and octagonal selection in purple. (c) Metabolite maps, overlaid on the anatomical images. (d, e) Axial and sagittal slices through 3D MRSI data. (f,g) Sample central (green) and periphery (blue) voxels (location is shown in (a) and (d)).

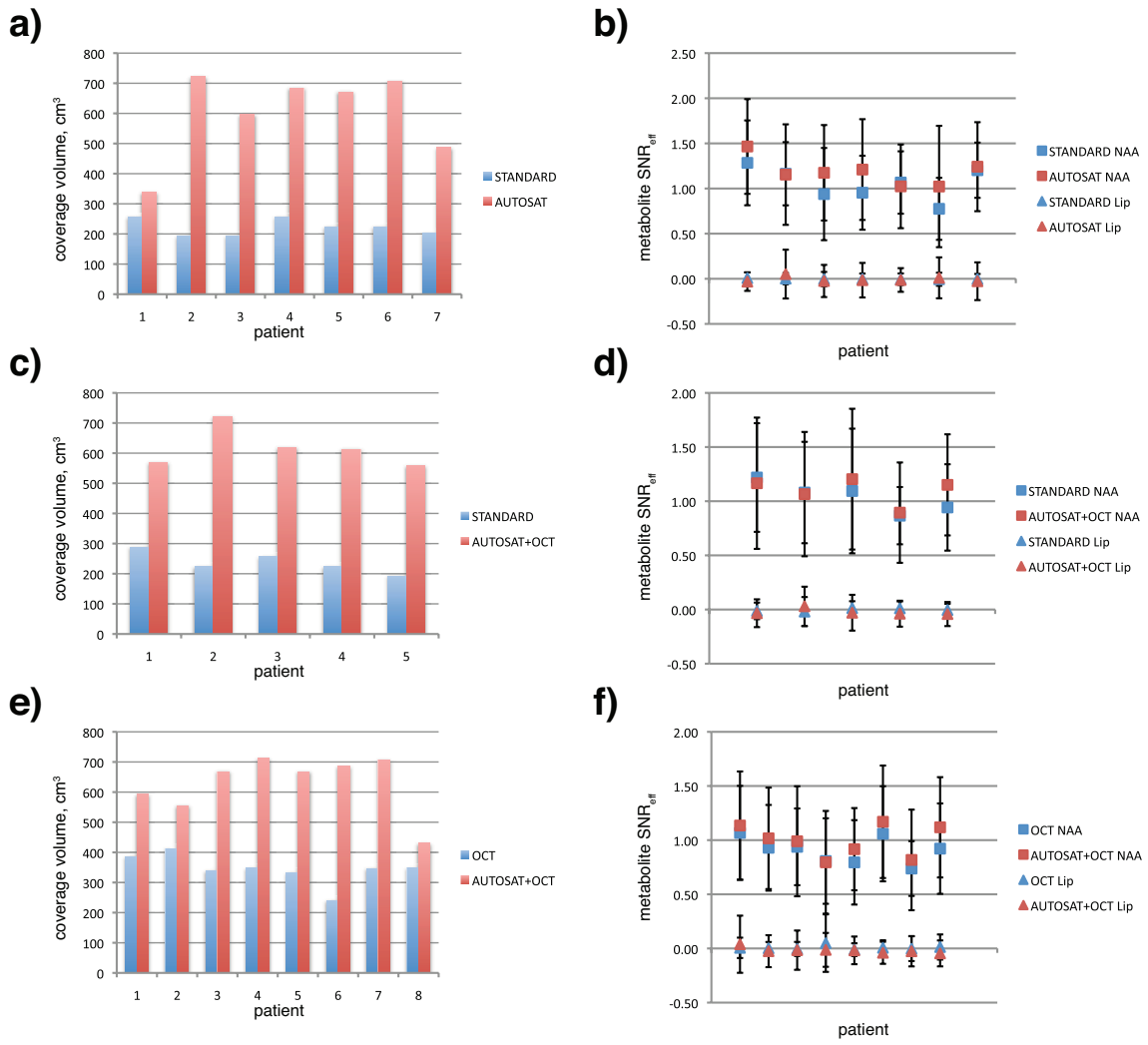


**Figure 4.6.** Pairwise comparison of coverage volume ( $\text{cm}^3$ ) and SNR efficiency of NAA

and lipid peaks for exams with two MRSI acquisitions.

(a, b) STANDARD and AUTOSAT, (c, d) STANDARD and AUTOSAT+OCT, (e, f)

OCTAGONAL and AUTOSAT+OCTAGONAL.

The NAA signal shows no decline in data quality in datasets with bigger coverage. There was no serious increase in lipid contamination, although the variance of the lipid signal was slightly bigger in those datasets. Lipid leakage could be detected in voxels adjacent to the sat bands, but was small enough not to affect the NAA peak (Fig. 4.5g). That was expected due to increased lipid excitation, caused by proximity and overlap between the PRESS box and lipids. It also demonstrated satisfactory ability of the sat bands to minimize this excitation. Metabolite linewidth values show no degradation in spectral resolution in protocols with automatic sat band placement. Although the data does not show major difference in terms of coverage and data quality between AUTOSAT and AUTOSAT+OCTAGONAL protocols, the use of octagonal sat band configuration together with automatically-placed sat bands made the protocol more robust to PRESS box placement without any additional drawbacks.

To test the reproducibility of the protocol with automatic sat band placement in a controlled setting, results from the AUTOSAT+OCTAGONAL protocol, as well as STANDARD protocol were compared with those, acquired from the same healthy volunteer on a separate date (Table 4.2). The high overlap volume for exams with AUTOSAT+OCTAGONAL protocol indicated that the technique was able to cover much of the same volume despite different head position and different operators, running the scan. In all cases very similar metabolite ratios within the same anatomical region were observed.

	volunteer 1		volunteer 2		volunteer 3	
	1	2	1	2	1	2
$V_S$ , cm <sup>3</sup>	224	324	324	288	324	324
$V_A$ , cm <sup>3</sup>	404	515	403	500	505	570
$V_{overlap}$ , cm <sup>3</sup>	427		327		502	
Cho/Cre (S)	1.009	1.044	1.198	1.177	1.286	1.290
Cho/Cre (A)	1.067	1.09	1.211	1.162	1.287	1.291
NAA/Cre (S)	1.985	2.093	2.103	2.078	2.196	2.139
NAA/Cre (A)	2.163	2.168	2.138	2.131	2.275	2.293

**Table 4.2.** Reproducibility of technique, measured by acquiring data from 3 healthy volunteers.

Each volunteer received two exams, prescribed by two different operators. Each exam contained STANDARD (S) and AUTOSAT+OCTAGONAL (A) MRSI acquisitions. Covered volumes ( $V_S$ ,  $V_A$ ) were defined as the volumes within the PRESS box, not covered by sat bands.  $V_{overlap}$  was calculated as intersection between the volumes, covered by AUTOSAT+OCTAGONAL acquisitions. Mean metabolite ratios were calculated within volumes, covered by all four acquisitions of the same subject.

		STANDARD	OCTAGONAL	AUTOSAT	AUTOSAT+ OCTAGONAL
N datasets		12	13	10	14
Coverage (cm <sup>3</sup> )		227.67±30.86 (224)	322.62±60.01 (340)	621.8±121.93 (672.5)	612.64±88.33 (616.00)
Cho	SNR	8.27±3.27 (8.16)	8.04±3.43 (8.14)	8.41±3.43 (8.58)	8.30±3.97 (8.06)
Cre	SNR <sub>eff</sub>	0.56±0.22 (0.56)	0.54±0.23 (0.55)	0.62±0.25 (0.63)	0.61±0.29 (0.59)
linewidth (Hz)		6.65±2.21 (6.63)	6.80±2.16 (6.76)	6.78±2.15 (6.86)	6.97±2.10 (7.11)
Cho	SNR	6.81±3.00 (6.97)	6.36±3.01 (6.57)	7.33±3.23 (7.57)	6.49±3.42 (6.45)
Cre	SNR <sub>eff</sub>	0.55±0.24 (0.56)	0.50±0.24 (0.52)	0.61±0.27 (0.63)	0.54±0.29 (0.54)
linewidth (Hz)		5.96±2.27 (5.80)	6.09±2.26 (6.20)	5.59±1.97 (5.69)	5.70±2.02 (5.76)
NAA	SNR	13.07±5.33 (13.37)	11.29±4.98 (11.69)	14.67±6.05 (14.63)	12.43±6.09 (13.03)
NAA	SNR <sub>eff</sub>	1.05±0.43 (1.07)	0.89±0.39 (0.92)	1.23±0.51 (1.23)	1.04±0.51 (1.09)
linewidth (Hz)		7.20±2.05 (7.22)	7.31±2.30 (7.12)	7.43±2.63 (7.58)	7.60±2.49 (7.66)
Lipid	SNR	-0.04±1.55 (-0.07)	0.15±2.48 (0.12)	-0.10±3.79 (-0.26)	-0.35±2.78 (-0.45)
	SNR <sub>eff</sub>	0.00±0.07 (0.00)	0.01±0.11 (0.01)	-0.01±0.21 (-0.01)	-0.02±0.16 (-0.03)
Cho/Cre		1.22±0.35 (1.24)	1.26±0.41 (1.26)	1.16±0.34 (1.13)	1.28±0.41 (1.29)
NAA/Cre		1.91±0.56 (1.94)	1.76±0.61 (1.78)	1.99±0.57 (2.01)	1.91±0.59 (1.92)

**Table 4.3.** Performance of the protocols in patients.

Mean coverage volumes, uncorrected metabolite SNR, SNR efficiency, linewidth and metabolite ratios and their standard deviations for the datasets, acquired from patients using the protocols that were compared (see table 4.3). Median values are shown in parentheses.

## Discussion

Achieving large coverage volume, while maintaining low lipid contamination of the data by manually placing sat bands is time-consuming and requires a highly skilled operator. Previously in our group, Osorio et al. developed an OVS scheme using octagonal selection with cosine-modulated VSS pulses (39). This allowed an increase in coverage within plane, but the curvature of the skull meant that it was only sufficient for single-slice acquisitions. Nevertheless, we found that using the octagonal sat band configuration together with manual sat bands (OCTAGONAL protocol) in place of a rectangular configuration (STANDARD protocol) improved the lipid suppression in the corners of the volume of interest in multi-slice MRSI acquisitions and allowed the operator to place a larger PRESS box closer to the edges of the brain, improving brain coverage.

Hovdebo and Ryner developed a technique that achieved non-cuboidal excited volume for single-voxel MRS by iteratively simplifying the polyhedral shape and using its faces to prescribe sat bands (59,60). 3D sat band optimization based on image data for spectroscopic imaging was introduced by Li et al. in their 2006 ISMRM abstract (55) and later elaborated in a paper by Martinez-Ramon (61).

While initially based on the same idea of maximizing the number of lipid pixel and minimizing the number of brain pixels covered by the sat bands, described in (55), the technique used in our study had several major differences from the one implemented in (61).

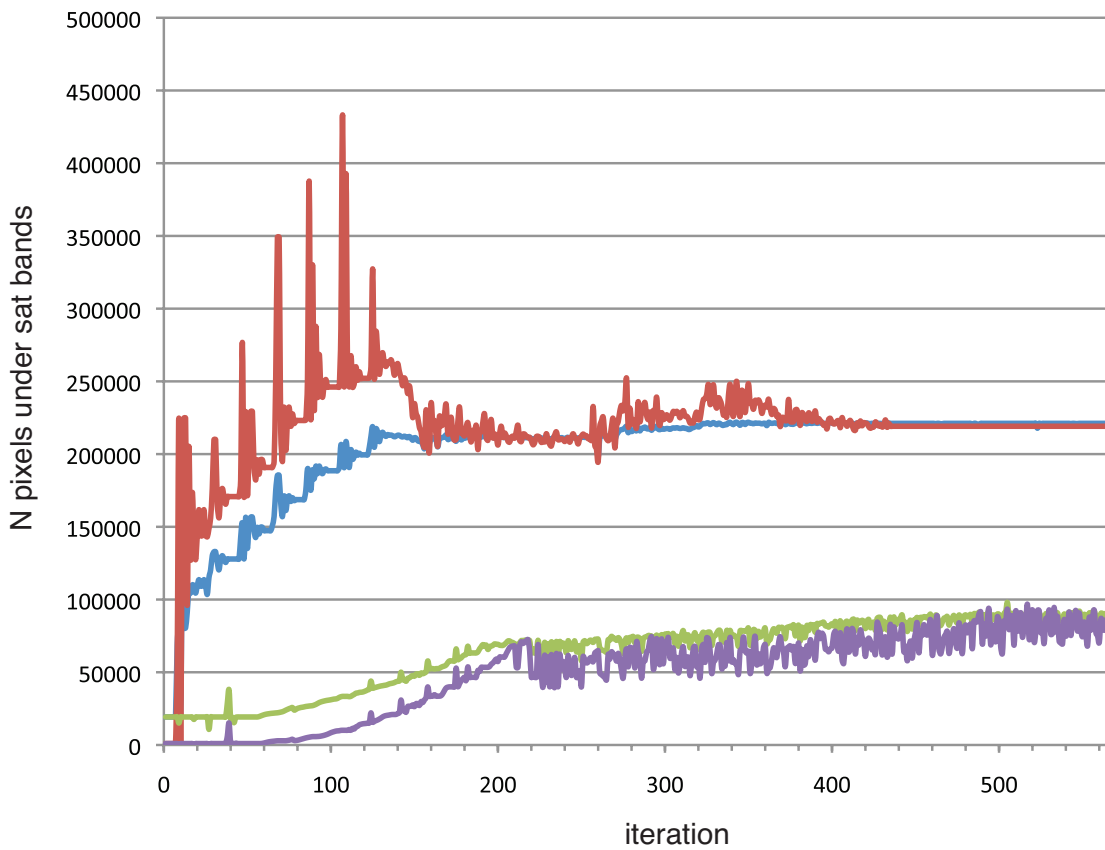


**Figure 4.7.** Convergence of the optimization algorithm.

Blue and red: number of lipid and brain pixels, covered by sat bands using a multistage algorithm; green and purple: number of covered lipid and brain pixels using an algorithm in which all parameters are optimized simultaneously.

One difference of our algorithm was that optimization was performed in several steps on subsets of parameters. Resulting values from one step were used as starting conditions for the next one. This made the algorithm find the optimal solution faster and, more importantly, prevented it from getting stuck in a local minimum. Figure 4.7 (red, blue) shows how the algorithm converged on an optimal solution in a reasonable number of iterations. The other two curves (green, purple) show what would happen if all 36 unknowns were optimized simultaneously, using

the same cost function and starting with the same initial configuration. While it was able to achieve some initial improvement, the optimization got stuck in a configuration that was likely a local minimum of the cost function and was not able to make much improvement after that. Also the cost function (eq. 4.1) contained the regularization term that discouraged configurations where no brain or lipid pixels were covered and the sat bands were far away from the origin. This obviated the need for a separate coarse placement of sat bands as in (61), since the initial distances to the sat bands could be calculated as a part of multi-step optimization with the same cost function.

Another difference of this technique was the use of linear interpolation of covered volume to achieve a continuous cost function, since the number of covered pixels was inherently discrete. Even with interpolation, the cost function was not differentiable, so the gradient-based optimization methods could get stuck in areas where the gradient was not continuous. Instead, we chose to use Nelder-Mead simplex method, which did not use the gradient of the cost function.

A major part of the study was development of the pulse sequence that could use additional calculated sat bands. While the technique in (61) calculated the placement of 16 sat bands, only 8 could be used by the pulse sequence. In contrast, the pulse sequence used in the in-vivo experiments, described in this paper, used 9 calculated sat bands in addition to 10 fixed bands in octagonal configuration, implemented using cosine-modulated RF pulses. This allowed us to effectively cover the top of the head, as well as provide additional suppression in the corners of the PRESS box.

The study in (61) presented MRSI data from six healthy volunteers and showed sat band placement very similar to that of a highly trained operator. The techniques developed in our study were able to achieve more optimal placement of sat bands than human operators did. That made possible to acquire good quality 3D MRSI data from a much larger volume of the brain than the current protocols. Optimal placement of the sat bands allowed the acquisition of MRSI data from tissues near the edge of the brain that were previously difficult to cover due to the curvature of the skull. It also ensured effective lipid suppression and allowed the PRESS box to extend beyond the boundary of the brain. Automatic placement of the sat bands was also designed to reduce the variability in the quality of the scan that is inherent for manual prescription. Repeated acquisition of data from the same subject with different head position and different operators (Table 4.2) shows very good reproducibility in terms of data quality and covered volume.

To verify that the technique works robustly in a clinical setting and allows for larger coverage volumes, we added an additional MRSI acquisition to the routine exams of patients with brain tumors. The data quality parameters (metabolite peak SNR, peak width, metabolite ratios) were calculated within the areas of healthy white matter to measure the effects of the technique itself on data quality as opposed to the variation in the parameters caused by the disease. These data show no compromise in data quality, while achieving significantly larger coverage volume. It was observed that the technique would bring the most benefit to the cases with multi-focal and heterogeneous tumors. Figure 4.5 shows one such case, which would

have required two standard MRSI acquisitions to cover both disease sites, while the AUTOSAT+OCTAGONAL covered both areas of interest at the same time.

One limitation of the study was that the authors had no control over the population of patients, scheduled to receive scans at our facility, so few patients in the study had challenging tumors like this. Also, due to experimental nature of the protocols with automatic sat bands, acquired data was not used by the physicians treating the patients. Future studies will assess the effects of the technique on radiological interpretation of tumor spectra.

The protocols with automatic sat band placement may add time to the patient exam. The optimization algorithm can be made to work with standard T1-weighted images, making it unnecessary to acquire an extra image series for sat band optimization. Calculation for the sat band placement took around 3 minutes (2.8 GHz Intel Xeon computer), which was usually less time consuming than adjusting sat bands manually and was usually run while another image series was being acquired.

The largest limiting factor encountered in our study was signal drop-off in the anterior of the lower slices, presumably due to field inhomogeneity caused by tissue-air interface in sinuses. This meant that tumors below the level of the eye-sockets could not be covered. This effect can be reduced by placing the PRESS box obliquely and performing high-order shimming over an oblique volume.

In conclusion, the technique described in this study has helped solve two of the most significant problems with brain PRESS-MRSI acquisitions: limited brain coverage and difficulty in prescription. The improved coverage will be useful for

evaluating heterogeneous and infiltrative tumors, as well as tumors at the periphery of the brain, which are difficult to evaluate with current protocols. It should make possible a more accurate assessment of the progression of tumors in serial studies. The use of this technique reduces the need for extensive operator training, thus facilitating wider utilization of MRSI in the clinical setting.

# **Chapter 5. Automated Oblique Prescription**

This chapter is based on the journal article titled called "Automated Prescription of Oblique Brain 3D Magnetic Resonance Spectroscopic Imaging," published in Magnetic Resonance in Medicine in 2012 (2).

## **Introduction**

Proton Magnetic Resonance Spectroscopic Imaging (MRSI) is a valuable modality for diagnosis and evaluation of brain diseases. It allows the measurement of relative concentrations of brain metabolites and hence evaluation of functional behavior of the tissue. MRSI has been successfully used for tumor classification, evaluating the extent of infiltrative gliomas, evaluating tumor malignancy, planning radiation and surgical treatments and predicting response to therapy and disease progression (62). It has also been used in evaluating patients with neurodegenerative diseases such as multiple sclerosis (MS) and Alzheimer's disease (63).

Two major difficulties with implementing MRSI in a clinical setting are limited coverage and difficulty in prescription. Clinical MRSI protocols typically keep the excited area (PRESS box) small to avoid exciting subcutaneous lipids and sinuses that could result in signal contamination in voxels far from the skull due to the "ringing" artifact and off-resonance artifacts due to magnetic susceptibility effects. Outer-volume suppression (OVS) with saturation bands, such as the previously developed Very Selective Suppression (VSS) bands (31) is typically used to suppress the signal from those areas.

In order to evaluate disease progression, the area covered by the MRSI data needs to match in subsequent exams from the same patient, which can be a challenge if the coverage volume is small and if there are differences in head position. Small coverage presents a problem when imaging multifocal and highly diffuse lesions, such as the ones commonly seen in patients receiving anti-angiogenic treatment. Improving coverage is also important for imaging patients with MS, since lesions often occur in multiple regions of the brain.

Several methods, besides OVS have been proposed for lipid suppression in MRSI and were described in Chapter 2. All of these approaches have benefits and tradeoffs that must be considered in the context of the requirements of a clinical protocol. While effective in lipid suppression, inversion recovery negatively affects the SNR of other metabolites and suppresses the lipid peak within the lesion, which is a valuable biomarker of tumor malignancy (28). Spatial filtering can reduce ringing artifacts, but leads to loss of spatial resolution. Using a large phase encoding matrix results in longer acquisition times that may be unacceptable for a clinical exam. Over-prescribed PRESS selection together with effective OVS scheme can help avoid the major downsides of PRESS (chemical shift artifacts, rectangular shape), while still preventing the excitation of a large part of the subcutaneous lipids.

The delicate balance between coverage volume and quality of data is difficult to achieve for any operator. An oblique PRESS box should usually cover the tumor and as much of the healthy tissue as possible, while avoiding the skull and sinuses. A number of saturation bands require manual adjustment. The use of high-order

shims (14) significantly improves the quality of the data, but usually requires an operator to outline a region of interest over which the shim would be optimized. Finally, the operator usually does not receive immediate feedback on the quality of prescription, since the data are often reconstructed offline. All of this makes acquiring 3D MRSI data a challenge in the clinical setting.

Earlier I developed a technique for optimization of the OVS saturation band placement for 3D MRSI (1). While allowing the acquisition of data from a larger volume of interest, this technique still requires manual adjustment of the PRESS box size and position. The PRESS box was kept in the axial orientation, making it possible to cover only the regions of the brain above the level of the orbits. In their recent paper Martinez-Ramon et al. proposed using a manually prescribed para-axial slab with automatically placed saturation bands (61).

Automated prescription has been used in brain MRI previously to ensure the consistency of image orientation. Among the proposed approaches was calculation of mid-sagittal planes (64,65), surface matching (66), active shapes (64,67), aligning to earlier images from the same subject (68) and to an atlas (69). Yung et al. proposed transforming an atlas-based manual prescription of the selected slice and OVS bands for MRSI (36).

The goal of this project was to completely automate the process of 3D PRESS MRSI prescription, including placement of the selection box, saturation bands and shim volume, while maximizing the coverage of the brain. Unlike MR imaging prescriptions, where the whole brain can be easily covered, defining the MRSI prescription requires calculation of the optimal size and position of both the PRESS

volume and OVS saturation bands, while taking into account the constraints imposed by the anatomy. This makes robust automated prescription crucial for acquiring good quality MRSI data from a large volume of the brain.

## Methods

### Overview

The automated prescription technique used in this study included acquisition of an anatomical MRI image (Fig. 5.1a), optimization of the oblique PRESS box geometry, optimization of the placement of OVS saturation bands (Fig. 5.1d, Fig. 5.2), and loading the calculated parameters into a customized 3D MRSI pulse sequence (Fig. 5.1e).

To validate the technique and compare its performance with existing protocols, 3D MRSI data were acquired from 6 exams of 3 healthy volunteers. To assess the performance of the automated 3D MRSI prescription for patients with brain tumors, the data were collected from 16 exams of 8 subjects with gliomas.

### Image Acquisition and Processing

A series of axial T1-weighted 3D IR-SPGR anatomic images without lipid suppression (Fig. 5.1a) was acquired as part of the clinical imaging protocol (256x256x120 matrix, 240x240x180 mm FOV, 15° flip angle, TE = 2.5 ms, TR=7.8 ms) using a 3T MR scanner (GE Healthcare, Waukesha, WI). Image processing and automated prescription were performed by a custom software package that was implemented in Matlab (MathWorks, Natick, MA), compiled into executable code and installed on the scanner console. The images were segmented into 3D lipid and brain tissue masks using the k-means clustering algorithm (54) with k=3 (Fig. 5.1b).

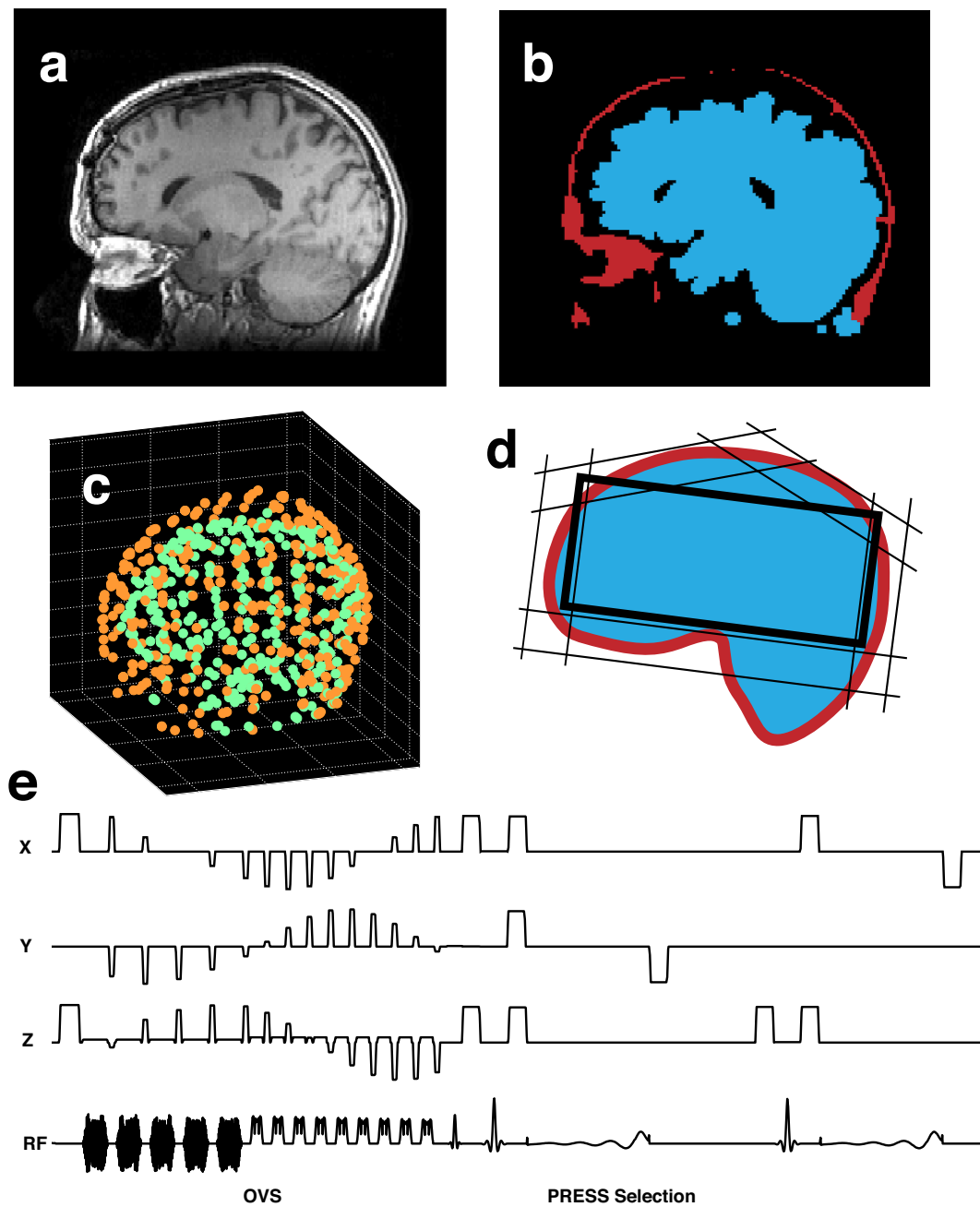


**Figure 5.1.** Technique overview.

(a) anatomical MRI image, (b) segmented lipid and brain tissue masks, (c) sets of points, defining the brain and lipid surfaces (d) calculated OVS saturation band and PRESS box configuration, (e) saturation band and PRESS box parameters loaded into the MRSI pulse sequence.

Morphological opening (brain mask) and closing (lipid mask) were performed to remove segmentation artifacts. The opening operation uses erosion, followed by dilation (70) to remove thin and small structures, while preserving the size of large objects. The closing operation (dilation followed by erosion) fills in the holes and gaps in the images. A number of inferior slices were removed by finding a cutoff level where the area of the brain mask was less than 10% of the total area of the image.

Two sets of 3D points, approximating the lipid and brain surfaces, (Fig. 5.1c) were generated by casting rays onto the brain and lipid tissue masks from the superior, left, right, anterior and posterior directions with a step of 10 pixels. The coordinate system was defined as X - right-left, Y - anterior-posterior and Z - inferior-superior with the center of mass of the brain surface as the origin.

### **Optimization of PRESS Box Placement**

An oblique plane was defined using anterior-inferior and posterior-inferior landmarks on the brain tissue mask (Fig. 5.2a). The anterior landmark was defined as the most inferior point of the brain mask, in which the Y coordinate lay within 5 mm of the minimum Y-value among all the points of the mask. Similarly, the posterior landmark was defined as the most inferior point, in which the Y-coordinate lay within 5 mm of the maximum Y-value. These two landmarks defined the inferior face of the PRESS box.

To find the optimum PRESS box placement, the algorithm iteratively searched for parameters that minimized the following cost function (Fig. 5.2b):

$$f(S) = -w_{dist} \sqrt{\prod_{i=1}^6 d(o, S_i)} + w_{pen} \sum_{p \in V_{in}} \left( \min_i d(p, S_i) \right)^2 \quad [5.1]$$

$S_i$  – faces of the PRESS box

$o$  – origin (center of mass of the brain surface)

$V_{in}$  – volume inside the PRESS box

$d(p, S_i)$  – distance from point  $p$  on the lipid surface to face  $S_i$

$w_{dist}, w_{pen}$  – weights for distance and penalty terms

Intuitively, the first term of the cost function approximates the volume of the press box, and if the volume were larger, the cost function would be lower. The second term balances the effect of the first one by adding a penalty, proportional to the square distance to any points on the lipid surface within the PRESS box. This discourages the PRESS box from growing outside the skull. The adjustable parameters were the distances from origin to the faces of the PRESS box. They were initialized with the standard deviations of X, Y and Z coordinates of points on the brain surface. The weights were fine-tuned manually to achieve convergence of optimization to an acceptable configuration. The active-set optimization algorithm, implemented by Matlab *fmincon* function (71) was used to find the parameters that minimized the cost function. The dimensions of the PRESS box were constrained by the maximum absolute values of X, Y and Z coordinates of the points of the lipid surface.

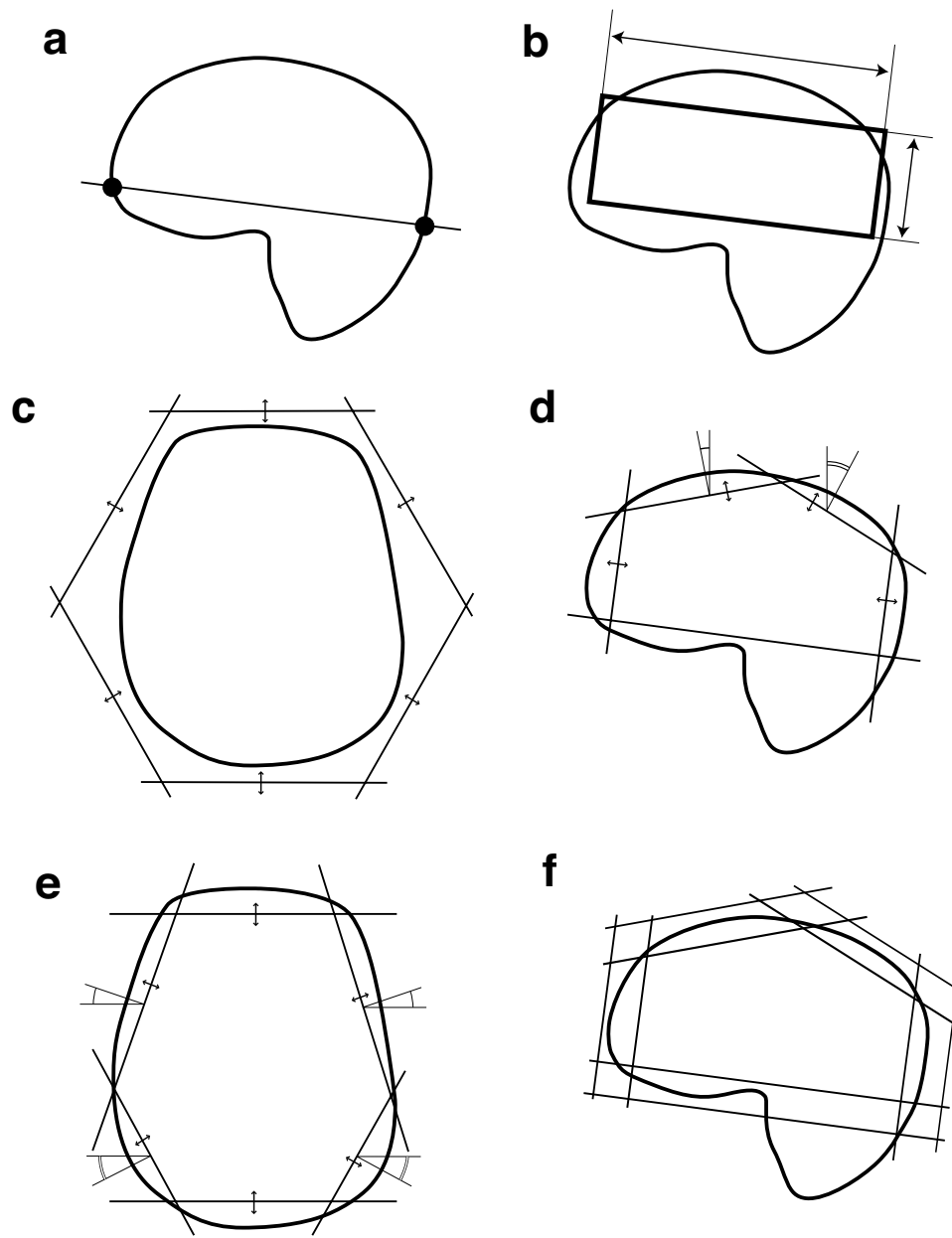


**Figure 5.2.** The stages of prescription optimization.

(a) the lower oblique plane was defined using anatomical landmarks, (b) optimization of dimension of the PRESS box, (c) optimization of distances to individual saturation bands, (d) fine optimization of saturation bands in the sagittal plane, (e) fine optimization of saturation bands in the axial plane, (f) defining the inner and outer surfaces of the saturation bands.

## OVS Saturation Band Placement Optimization

The algorithm that optimized the saturation bands searched for a configuration where the bands closely approximated the skull surface. Placement of each band was defined by  $\alpha$  – angle around inferior-superior axis,  $\beta$  – angle between the saturation band normal and the inferior-superior axis and  $d$  – distance from origin to the plane of the saturation band. The inferior band was placed obliquely along the inferior face of the PRESS box. The other eight bands were initially placed with six bands, forming a hexagon in the axial-oblique plane (Fig. 5.2c) and two bands placed superior and tilted in the anterior and posterior direction by 30°.

The OVS saturation band configuration was optimized in 3 stages by minimizing the following cost function with different constraints:

$$f(S) = \sum_p \left( \min_i d(p, S_i) \right)^2 + w_{dist} \sqrt{\sum_i d^2(o, S_i)} + w_{pen} \sum_i \sum_{p \in V_{out,i}} d(p, S_i) \quad [5.3]$$

where:

$S_i$  – planes of sat bands

$d(p, S_i)$  – distance from point  $p$  on the lipid surface to saturation band  $i$

$o$  – origin (center of mass of the brain surface)

$V_{out,i}$  – outer volume of band  $S_i$

$w_{dist}, w_{pen}$  – weights for distance and penalty terms

Intuitively term 1 of the cost function would be minimal when the planes lie closest to the lipid surface. The distance term (term 2) added regularization when the planes were far from the surface. The penalty term (term 3) insured that the planes remained on the outer side of the lipid surface during optimization.

At the initial stage, only the distances to the bands were allowed to vary (Fig. 5.2c). In the second stage, the distances to the bands, orthogonal to the sagittal plane along with the tilt angles of the superior planes were optimized (Fig. 5.2d) In the third stage the placement of bands, orthogonal to the axial-oblique plane was optimized (Fig. 5.2e). Additional constraints ensuring that the configuration was symmetrical in right-left direction were imposed throughout the optimization. At the end of the optimization, the saturation bands ended up approximately tangential to the lipid surface. The inner plane of each saturation band was then set 15 mm inward and the outer plane – 30 mm outward from the tangent plane (Fig. 5.2f). This enclosed the lipid surface between the polyhedrons, defined by the inner and outer planes of the saturation bands.

The calculated PRESS box and saturation bands were overlaid on the anatomical MR images and displayed using an interactive 3D visualization tool OrthogonalSlicer (L. Balkay, Univ. of Debrecen, Hungary). If required, the user had an option to override the automated prescription and place PRESS box and OVS saturation bands manually.

### **Shimming**

The vendor-supplied high-order shimming routine (14) was modified to automatically define an ROI based on the calculated MRSI PRESS box. This was defined as an ellipsoid fitting within the PRESS box. The shim currents were calculated to minimize the B0 field inhomogeneity within the ROI and downloaded to the hardware before the MRSI acquisition.

## **Pulse Sequence**

The MRSI pulse sequence was modified to allow PRESS box parameters to be loaded from a file: center (L, P and S), size (X, Y and Z) and rotation angles ( $\alpha$ ,  $\beta$ ,  $\gamma$ ). These parameters were used to calculate the gradient amplitude and RF frequency offsets for PRESS excitation.

The sequence also allowed the parameters of up to 16 saturation bands to be loaded, as described in (1). Octagonal selection volume was implemented within the MRSI pulse sequence by using 5 cosine-modulated saturation pulses (39) to produce 10 saturation bands: 6 along the faces of the PRESS box and 4 over the corners of the PRESS box in the axial-oblique plane. A protocol could utilize any combination of these OVS methods.

## **MRSI acquisition**

Data were acquired using a commercially available 8-channel head coil and an EPSI flyback sequence (10) (TE = 144 ms, TR = 1100 ms, 1 cm<sup>3</sup> isotropic voxels, NEX=1). J-difference lactate editing with dual basing pulses was used to provide summed data for Cho, Cr, NAA, and lipids and difference data for lactate as required by the clinical protocol. The PRESS volume was over-prescribed (OverPRESS) by the factor of 1.5 to minimize the chemical shift artifact of PRESS excitation.

Raw data were reconstructed offline using an approach that has been described previously (15,16). Data from each channel were filtered with 4 Hz apodization, Fourier-transformed in spatial and frequency domains. Phase and frequency corrections, residual water and baseline removal were performed. Data

from different channels were combined using the weights, obtained from a low-resolution proton-density calibration image.

### **MRSI Protocols**

The data obtained with automated prescription were compared with two existing protocols (table 5.1):

#### *Manually Prescribed MRSI (MANUAL)*

This protocol used a manually prescribed PRESS box (superior-inferior dimension: 4 cm) with 6 fixed saturation bands along the edges of the PRESS box and 6 additional saturation bands that were manually placed by operators to cover regions of lipid.

#### *MRSI with Automatically Generated Saturation Band Placement (AUTOSAT)*

This protocol used the automatically prescribed saturation bands together with octagonal selection (1). The PRESS box (SI dimension: 6 cm) was prescribed manually by the operator in the axial plane. Since the algorithm placed the lower saturation band to cover the nasal cavities and orbits, the PRESS box was placed above the eye-level.

#### *Automatically Prescribed MRSI (AUTO MRSI)*

This protocol used the automatically prescribed oblique PRESS box, together with an improved implementation of automated OVS (9 bands). The optimal X, Y and Z dimensions of the PRESS volume were determined automatically as described above. Octagonal selection (10 bands, 5 OVS pulses) was used for additional suppression in the corners of the selected volume.

	MANUAL	AUTOSAT	AUTO MRSI
Scan Plane	axial	axial	axial-oblique
Automated PRESS box placement			✓
Fixed ROI-edge saturation bands	✓		
Manually prescribed saturation bands	✓		
Automatically prescribed saturation bands		✓	✓
Octagonal selection		✓	✓
FOV (cm)	16x16x16	18x18x16	18x18x16
TR (ms)	1104	1500	1140
T <sub>acq</sub> (min)	9	13	13

**Table 5.1.** 3D MRSI acquisition protocols that were considered in this study.

*MANUAL = MRSI with manual prescription, AUTOSAT = MRSI with automatically generated saturation band placement, AUTO MRSI = automated oblique PRESS box and saturation band placement.*

## Subjects

The data was collected from three healthy volunteers. Each volunteer received two MRSI exams on different days with different operators within the period of two weeks. Both exams included MRSI acquisitions with all the protocols listed above.

The automated MRSI protocol has been implemented in a clinical research protocol for patients with brain tumors and was performed on 54 subjects during the study timeframe (June 2010 - January 2011). In total, the technique was used in 62 MRSI exams and was successful in 52 cases. The automated prescription failed in 2 cases. In 5 cases the tumor was not covered by AUTO MRSI due to its inferior location and

MANUAL protocol had to be used instead. In 3 cases interpretable data could not be acquired due to scanner hardware or software failures.

The 8 patients who received two MRSI examinations with the automated protocols during the study timeframe were selected for this study. The exams were performed after the patients had undergone surgery and were 3-4 months apart from each other. The patients were undergoing a course of treatment that included radiotherapy, temozolomide and other chemotherapy agents. Since the patients were not part of any clinical study, their detailed medical history was not available. All subjects provided informed consent as approved by the Institutional Review Board.

### **Data analysis**

Parameters that were used to evaluate the data included the coverage volume, consistency of prescription and the quality of spectral data. The coverage volume of the MRSI acquisition was calculated by generating masks from the parameters, obtained from the headers of raw data files, produced by the MRSI acquisition. The coverage volume was defined as the number of spectroscopy voxels within the PRESS box excluding those covered by a saturation band by more than 50%. Coverage volumes between the STANDARD, AUTOSAT and AUTO MRSI protocols were compared with 1-tailed t-test with unequal variances.

To estimate the consistency of the prescription, the volume of brain tissue that was covered by two MRSI exams from the same subject was calculated as the volume of the intersection of the aligned coverage masks. For this purpose, the exams were aligned to the same coordinate system based on the anatomic images

using VTK CISG Registration Toolkit (Computational Imaging Science Group, King's College London). Bland-Altman repeatability coefficient  $RC = 1.96 \sigma\Delta V$  and mean  $\Delta V$  were calculated for covered volumes for exams from the same subjects (72). Assuming the differences between measurements are approximately normally distributed, the absolute difference between them is expected to differ by no more than the RC for 95% of the time.

To compare data quality, the spectroscopic parameters, such as peak SNR, metabolite ratios and peak linewidth were calculated within the whole covered volume and within the intersection of all volumes covered by different protocols using software developed in our laboratory (15,16). Spectral quality within the tumor (for patients with brain tumors) was assessed by analyzing the same parameters within the T2 lesions as defined by manually outlined ROIs. The peak heights (real and magnitude) were measured based on predefined peak regions in spectral data that had baseline, phase and frequency corrections applied, as described by Nelson et al. (15). The SNR of individual peaks was calculated using the tail end of the spectra for noise estimation. The SNR values were corrected for the difference in acquisition times and repetition times (SNR efficiency) using the relaxation constants for individual metabolites (57,58). Bland-Altman repeatability coefficients and mean differences (72) were calculated for changes in metabolite ratios within the whole brain (volunteers) and T2 lesions (patients) using the same AUTO MRSI protocol (test-retest experiment) and for comparing the values obtained with AUTO MRSI and MANUAL protocols (measurement technique validation).

## Results

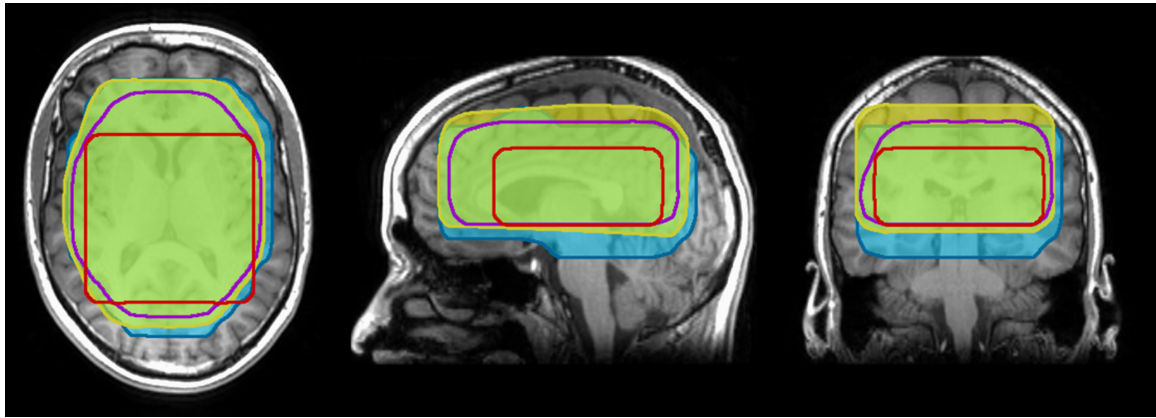


**Figure 5.3.** Example of the covered volumes acquired from a healthy volunteer using the following protocols: red – MANUAL, purple – AUTOSAT, yellow and blue – AUTO MRSI (from different exams).

All three protocols showed good quality data for the six exams from the three normal volunteers. Figure 5.3 shows an example of the covered volumes from different protocols, overlaid over an anatomical image. Figure 5.4 shows the calculated coverage volumes of those protocols in healthy volunteers. The mean fraction of the total brain volume (including the cerebellum), covered by MRSI was  $21\pm2\%$  for MANUAL,  $32\pm3\%$  for AUTOSAT and  $53\pm7\%$  for AUTO MRSI. Two of the previously used protocols (MANUAL and AUTOSAT) had PRESS volume dimensions determined by the operators with default SI dimensions of 4 and 6 cm, respectively. These values were considered optimal by the operators performing routine clinical-research scans with these protocols and could be changed on a case-by-case basis. The mean coverage volumes for these protocols in patients were  $227.67 \text{ cm}^3$  for MANUAL and  $621.8 \text{ cm}^3$  for AUTOSAT, as published previously (1). The resulting covered volumes in these protocols, however, were likely suboptimal and biased by

the operators' fear of compromising the quality of data and limited time to prescribe a scan. In contrast, the AUTO MRSI protocol always tailored the prescription to the subject's anatomy. While it was not possible to compare the automated prescription to an ideal manual prescription, our results show that by avoiding the biases, resulting from the predefined protocol parameters and manual prescription, AUTO MRSI achieved significantly larger covered volume than the MANUAL protocol with manual prescription ( $p<0.0005$ ) and the semi-automated AUTOSAT protocol ( $p<0.005$ ).

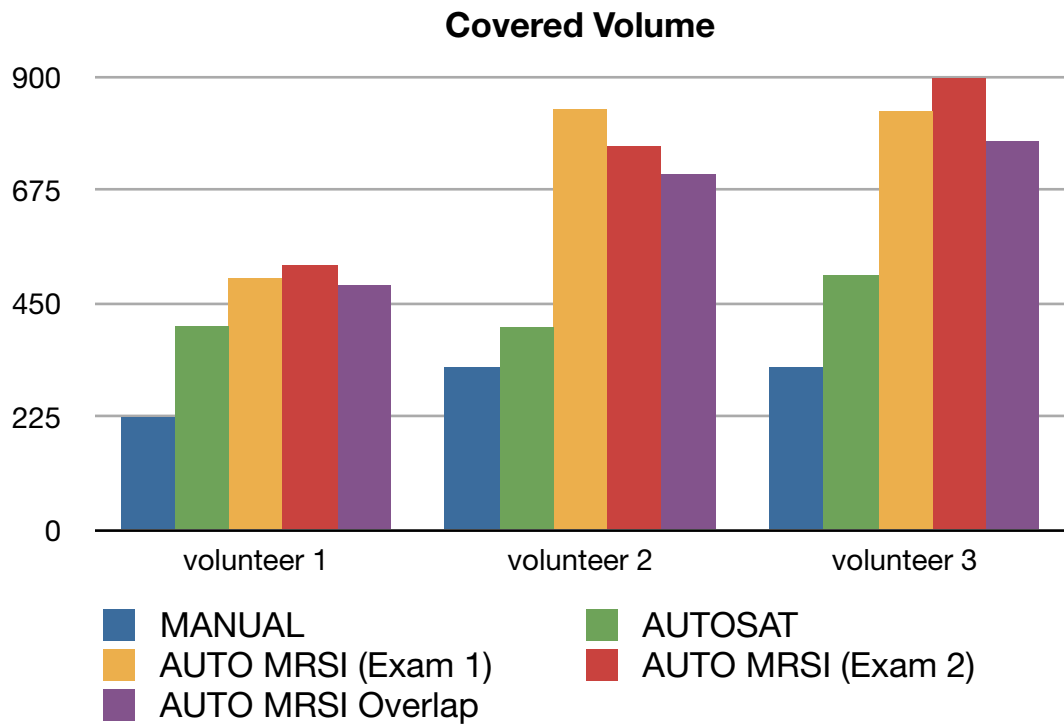


**Figure 5.4.** Covered volume of the three volunteers using the three protocols that were compared.

The volunteers received two AUTO MRSI acquisitions on different days (yellow and red). Purple column shows the volume that was covered by both of those acquisitions.

Figure 5.5 shows an example of a dataset, acquired from a patient using the AUTO MRSI protocol. The automated prescription was able to cover most of the supratentorial brain, including almost all of the T2 lesion. The oblique PRESS box covered inferior areas of the brain posteriorly, while avoiding the orbits and sinuses in the anterior areas of the brain. Figure 5.5c shows one slice of the metabolite maps for Cho, NAA, Lipid and Choline to NAA Index (CNI)(73). Figures 5.5d-g show axial and sagittal slices through the spectral data as well as sample voxels from the tumor and healthy tissue. The Cho and NAA metabolite maps show decreased metabolite concentrations throughout the anterior-right side of the brain, beyond the region of elevated choline, which could be attributed to the effect of the radiation therapy. The lipid map shows that only a few voxels on the periphery of the brain had noticeable lipid contamination. There is a region of elevated lipid within the T2 lesion, which appears to be coming from the necrotic core of the tumor.

The algorithm was able to achieve high consistency of prescription despite differences in subject positioning. The purple column on figure 5.4 shows that in the exams of the same healthy volunteers, the covered volume was largely the same (average overlap: 91%). In patients, the technique also demonstrated very good consistency of prescription (average overlap: 88%). Figure 5.6a shows the covered volume for two exams from each patient as well as the volume of the overlap area between the two of them. Mean fraction of the total brain volume (including the cerebellum) that was covered by MRSI was  $56\pm10\%$ .

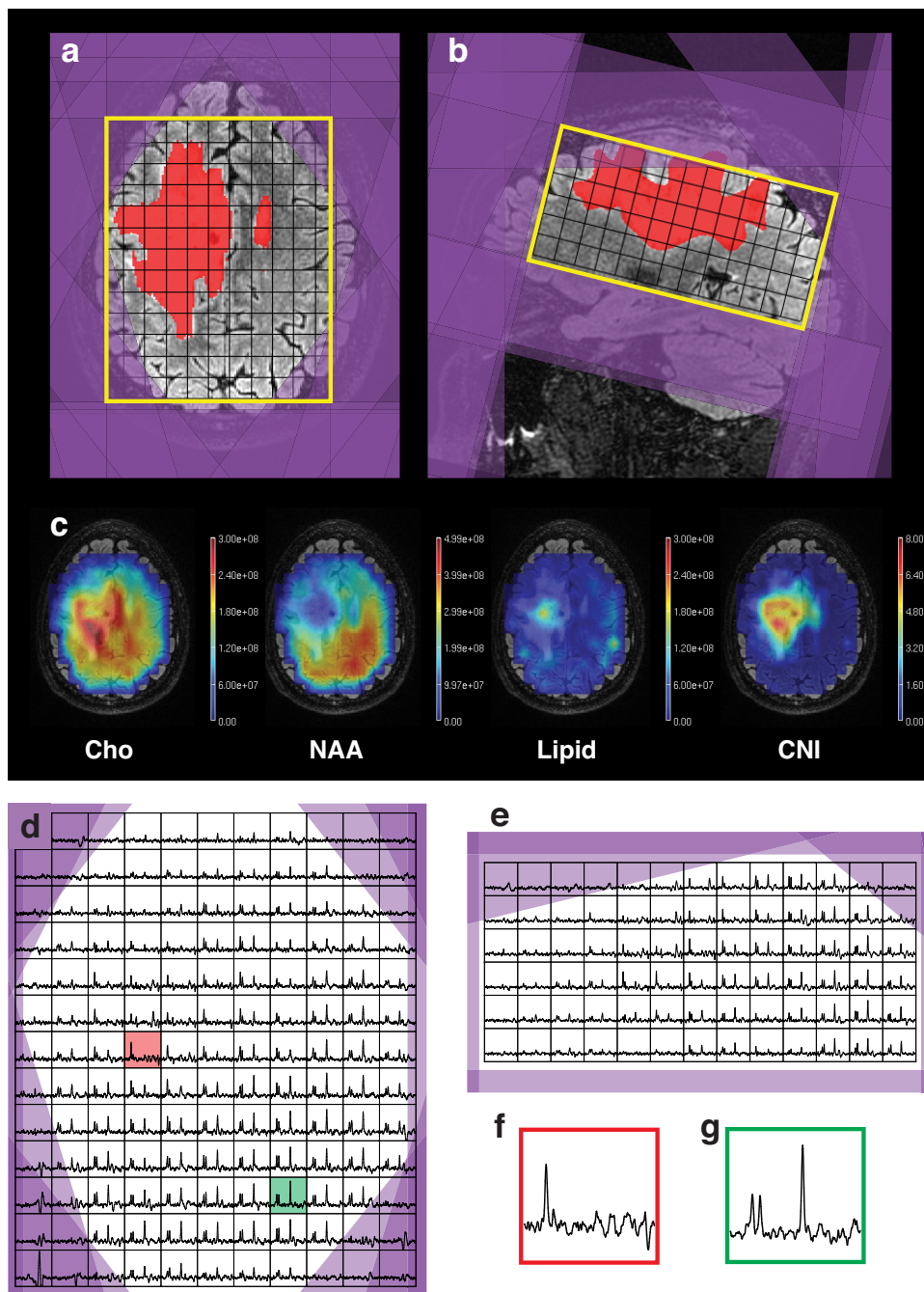


**Figure 5.5.** Dataset, acquired from a patient using the AUTO MRSI protocol.

(a, b) Automatically generated MRSI prescription (yellow – PRESS box, purple – saturation bands), overlaid on top of T2 FLAIR images and T2 lesion mask (red); (c) metabolite maps; (d, e) axial and sagittal slices through the spectral grid; (f, g) sample spectral voxels from T2 lesion (red, location shown on (d)) and healthy tissue (green).

The volumes of the T2 lesions and their coverage by MRSI are presented on figure 5.6b. In almost all exams the T2 lesion was well covered by the MRSI volume of interest. There was only one exam (patient 8, exam 1) where a large part of the lesion could not be covered because most of it was in the inferior regions of the brain. Changes in the T2 lesion volumes between exams could be attributed to response to therapy or disease progression.

The mean metabolite ratios, calculated within the T2 lesion areas are shown on figure 5.6c. In most cases they show very consistent results between exams of the same patient. Unlike the healthy volunteers, most patients showed choline that was elevated relative to NAA. For patient 4 it was not possible to reliably quantify the ratios due to the T2 lesion being very small (less than 7 cm<sup>3</sup>). For patient 7 choline became less elevated in the second exam. This could be attributed to averaging over a much larger T2 lesion. Bland-Altman reproducibility coefficients and mean differences for coverage volumes and metabolite ratios (test-retest for AUTO MRSI and comparison to MANUAL) from volunteers and patients are shown in table 5.2. All parameters show good reproducibility and small bias for measurement in the same subjects, compared to standard deviations of parameters within subjects with an exception of Cho/Cr ratio in patients. This is to be expected, since choline is a major metabolite that changes due to treatment and disease progression.

		Mean	RC	Mean $\Delta$
V, cm <sup>3</sup>	volunteers	725.33	141.07	6.67
	patients	758.5	184.51	37
Cho/Cr	volunteers	1.24	0.045	0.031
	volunteers (AUTO MRSI vs. MANUAL)		0.041	0.059
	patients	1.77	1.683	0.043
NAA/Cr	volunteers	2.23	0.018	0.002
	volunteers (AUTO MRSI vs. MANUAL)		0.027	0.13
	patients	1.20	0.57	0.009

**Table 5.2.** Mean values across all subjects, Bland-Altman reproducibility coefficients and mean differences between measurements of the same subject for coverage volumes and metabolite ratios.

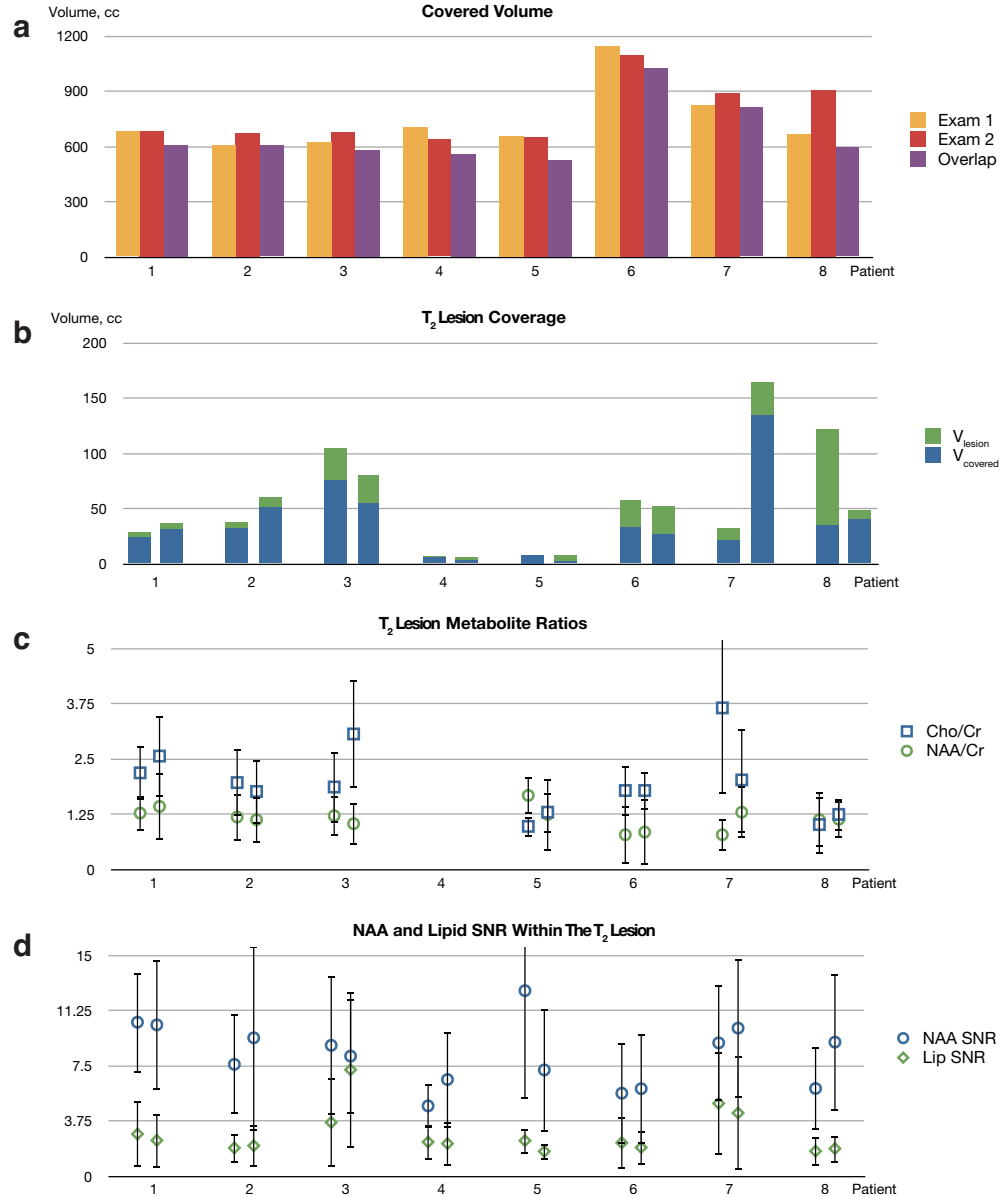
The mean NAA SNR efficiency for the whole covered volume in all exams was  $0.92 \pm 0.63$ , and for the T2 lesions it was  $0.58 \pm 0.31$ . These numbers were comparable to those of the healthy volunteers (table 5.3) and were expected to be lower in the patients due to the effects of the disease and therapy. Mean NAA linewidth was  $12.01 \pm 2.81$  Hz throughout the whole volume and  $11.43 \pm 2.87$  Hz within the T2 lesion, which are similar to the linewidths, observed in volunteers with existing protocols.

Figure 5.6d shows the mean SNR of the magnitude NAA and lipid peaks within the T2 lesions in all datasets and their standard deviations. It indicates that

the lipid signal was much smaller than the signal from NAA and did not interfere with NAA quantification, which is crucial for interpretation of brain MRSI data.

	MANUAL	AUTOSAT	AUTO MRSI
NAA SNR <sub>eff</sub>	1.25±0.54	1.38±0.53	1.34±0.48
NAA linewidth (Hz)	10.53±2.1	10.67±1.94	10.92±1.89

**Table 5.3.** Mean SNR efficiency and linewidth and their standard deviations of the NAA peak in the datasets, acquired from healthy volunteers with the protocols that were compared.



**Figure 5.6.** Consistency of prescription and data quality.

(a) Covered volume ( $\text{cm}^3$ ) for the two exams of the patients with brain tumors (yellow and red) and the volume of the overlap area between those exams (purple); (b) The volume in  $\text{cm}^3$  of the T2 lesion (green) and T2 lesion covered by MRSI acquisition (blue); (c) Mean Cho/Cr (blue) and NAA/Cr (green) metabolite ratios and their standard deviations, calculated within the T2 lesion; (d) Mean magnitude NAA (blue) and lipid (green) SNR within the T2 lesion and their standard deviations.

## **Discussion**

Realizing the true clinical value of brain MRSI requires that data are acquired from the whole brain as easily as conventional imaging data. The technique developed in this project came closer to this goal than any of the previous approaches (1,36,61). The data from patients and volunteers showed that automated prescription was able to achieve much larger coverage volumes while allowing the acquisition of high-quality data from both the lesions and the healthy tissue.

The approach taken in this study was different from that of Yung et al., which included affine transformation of a manually placed MRSI slice and OVS saturation bands from an atlas coordinate space to that of the patient exam (36). Our technique used a multistep iterative algorithm to achieve a configuration optimal for the anatomy of each individual subject. The cost functions were designed for faster convergence using a gradient-based optimization method. Constraints were imposed on the parameters, which were subdivided into groups and optimized in multiple steps to minimize the dimensionality of the parameter space and to avoid converging on a local minimum. That allowed us to achieve a much shorter calculation time (about 30 sec) than the previous approaches and made it possible to run the automated prescription software directly on the scanner console. The optimization of the PRESS box size enabled acquisition of data from the largest possible volume for a given brain. Finally, in the present technique, the pulse sequence was customized to read all the prescription parameters from files, automating the entire scan prescription.

Fully automated prescription of MRSI exams has resulted in more comprehensive and consistent MRSI datasets and reduced the need for time-consuming operator training. A large coverage volume reduced the risk that some of the diagnostically relevant tissues would be left outside the volume of interest, while the oblique orientation of the PRESS box ensured better coverage of the inferior regions of the brain. This is especially critical for diseases such as multifocal gliomas, where previously a single acquisition was not enough to cover all parts of the tumor. Including a large number of healthy voxels in the volume of interest also improved statistical quantification of metabolic abnormality parameters, such as Choline to NAA Index (CNI, (73)), which estimates how different a given spectrum is from that of a "normal" brain.

Automated prescription also improved the consistency of prescription. This is especially important for serial scans of the same patient. The tissue, that is unremarkable in an earlier scan might become of interest in a later one. A large overlap between the covered volumes in these scans will improve the detection of metabolic changes as disease progresses.

Manual prescription of MRSI exams is a difficult and time-consuming task. It took an experienced operator about 5 minutes to set up a regular MRSI acquisition, compared to calculation time for automated prescription of about 30 seconds. The use of automated prescription software will ensure that in most cases the operators could acquire good quality data by following a simple protocol. This will make adding MRSI to clinical protocols much easier and will solve many problems in organizing multi-center clinical trials that employ MRSI.

The proposed technique gave rise to a number of new challenges. Since the volume of interest is much larger than in conventional methods, B0 variations over the volume of interest can cause peak broadening and loss of spectral resolution. This was addressed by automated high-order shimming over an ellipsoidal shim volume that was based on the oblique PRESS box and produced excellent results in most cases.

The algorithm could fail to achieve a good prescription in some cases. This could be due to failures of segmentation logic or failure of the optimizations to converge. These cases were rare and often corresponded to the subjects with unusual brain structure, such as large portions of the brain tissue missing due to prior surgery. The automatically prescribed volume of interest may fail to cover the lesion, or the lesion may be obscured by OVS saturation bands. That could happen, for instance when the lesion is located in the extremely superior or inferior regions of the brain. In such cases, the protocol can fall back to manual prescription. While no automated image analysis algorithms succeed 100% of the time, effective quality assurance, together with the option of the manual alternative, ensured that data could be obtained in all cases, as required in the clinical setting.

In some datasets, as with conventional methods, lipid contamination was detectable within the brain, usually in the voxels adjacent to the skull. Usually the lipid peak was not big enough to affect the NAA peak. This could be minimized by making saturation band placement more aggressive. There is an inherent tradeoff, however, between the increase of the lipid coverage and the decrease of the area from which MRSI data can be acquired. In this work we aimed to achieve balance

between these competing effects by making the usable volume as large as possible, as long as the level of the lipid contamination was low enough for data interpretation.

In conclusion, the automated prescription technique described here provided larger coverage volumes than previous manual protocols while maintaining high quality of data. It also yielded consistent prescription quality, not dependent on operator skill, and made possible to include 3D MRSI into the clinical research protocols without the need for extensive operator training.

# **Chapter 6. Slice-Selected 3D MRSI with Automated Prescription**

This chapter is based on the work, presented at the 19th annual meeting of the International Society for Magnetic Resonance in Medicine (ISMRM) in 2011 (3).

## **Introduction**

Automated prescription of 3D Magnetic Resonance Spectroscopic Imaging (MRSI) helps solve a major problem of translating spectroscopic imaging into the clinical setting the need for operator training. It can also improve brain coverage and reproducibility compared to manual prescription. In chapter 5, I described how the calculated placement of an oblique Point-Resolved Spectroscopy (PRESS) box together with a number of outer-volume suppression (OVS) sat bands, based on an already acquired anatomic image, was used as input to the MRSI pulse sequence.

Traditionally, PRESS selection has been used to perform a 3D volume selection when doing MRSI acquisition. Its main limitations were blurred selection profile and chemical shift artifacts due to low bandwidth of the selection pulses. To overcome that, the PRESS box was often "over-prescribed" to cover a larger volume, while outer-volume suppression (OVS) sat bands were used to define the volume of interest. In the exams with the large volume of interest, the PRESS box often covered the whole head, reducing the benefits of selection in X and Y directions.

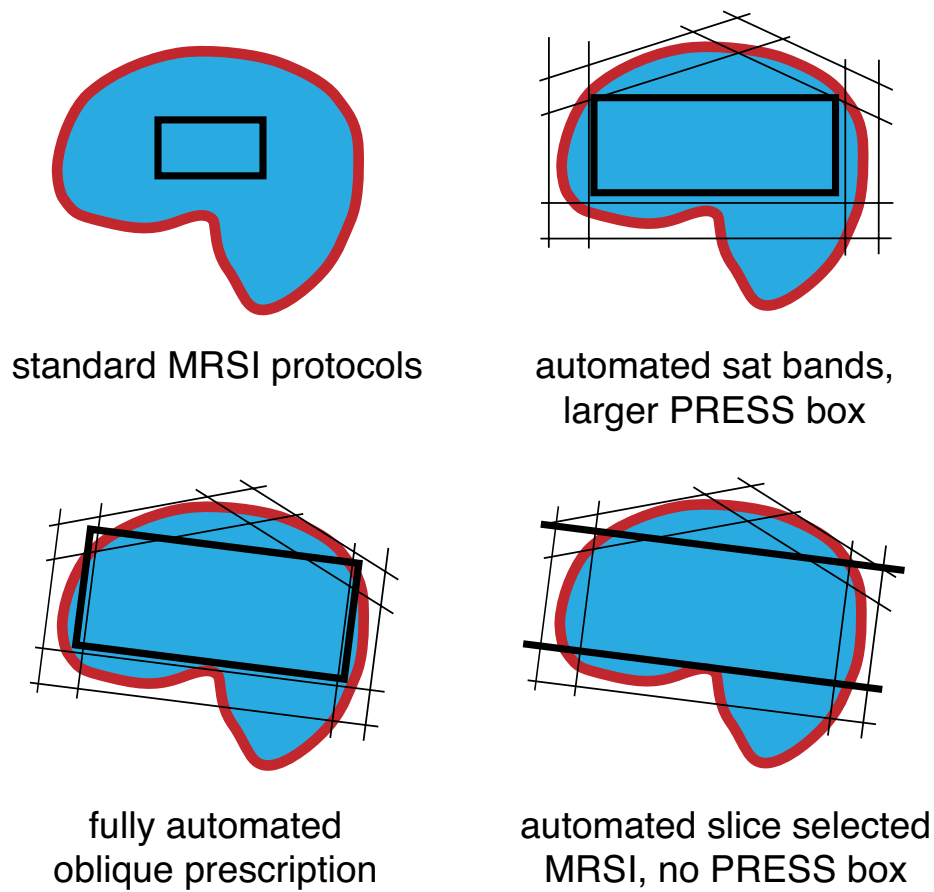


**Figure 6.1.** MRSI localization techniques.

*(manual PRESS selection, automated saturation band placement (ch. 4), automated oblique prescription (ch. 5) and automated slice selected acquisition (this chapter))*

Outer-Volume Suppression (OVS) and slice selection have been used previously instead of PRESS in 2D MRSI (33,34). For 3D MRSI, this approach could allow for a non-cuboidal volume of interest, better approximating the shape of the brain, but would require a large number of OVS sat bands. Cosine-modulated VSS pulses have been used previously to simultaneously suppress two parallel bands (39) but doubled the required peak RF amplitude. While lower peak-power

dualband VSS pulses can be designed with root flipping (41,42) as in (40), this approach required the complex RF design to be performed at scan time.

The present work has combined a new automatic prescription algorithm with an MRSI protocol that uses slice selection in place of PRESS. The VSS pulse design was modified to allow for simpler pulse sequence implementation.

## Methods

### Automated Prescription

The automated prescription technique was based on the one described in chapter 5 and included acquisition of T1-weighted anatomical images, segmentation to obtain brain and lipid surfaces, landmark-based definition of the inferior oblique plane, optimization of the excited slice and optimization of OVS sat band placement.

The automated prescription software used T1-weighted 3D IRSPGR images that are acquired as part of the standard clinical examination. The technique could also be adapted to use any other anatomical MR images with high enough brain-lipid contrast. The image volume was segmented into lipid and brain tissue masks using k-means clustering with k=3. Artifacts of segmentation were removed with morphological opening and closing. Two sets of points that define the lipid and brain surfaces were defined by casting rays from 6 directions onto the segmented masks. Since anatomical surfaces are smooth, they could be approximated with a smaller number of points, making possible to perform the calculation in an acceptable time.

Lower oblique plane defined using anterior-inferior and posterior-inferior landmarks, as described in the previous chapter. Slice thickness optimized by minimizing the following cost function:

$$r = -w_d \sqrt{d} + w_p \sum_{d_i < 0} d_i \quad [6.1]$$

where:

$d$  – thickness,

$d_i$  – distance from point  $i$  to the upper slice boundary ( $d_i < 0$  if the point is below the boundary),

$w_d, w_p$  – weights.

Intuitively, this cost function tries to maximize thickness, while avoiding surface points inside the selected slice.

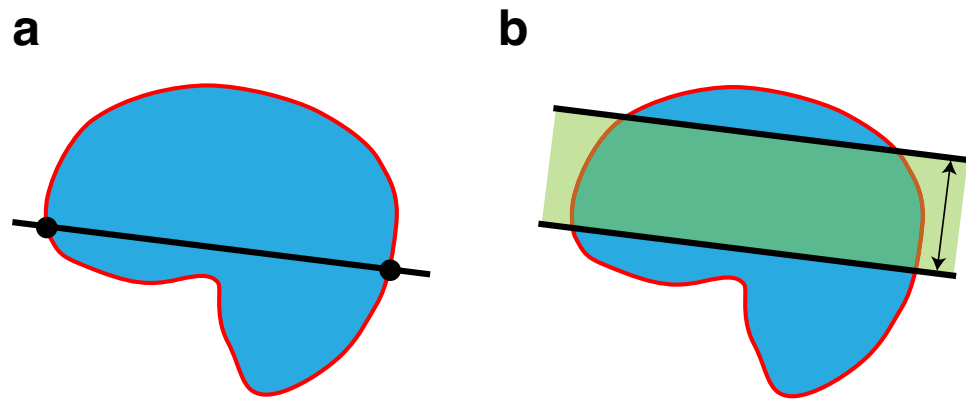


**Figure 6.2.** Automated placement of the selected slice.

(a) placement of the lower oblique plane using anterior and posterior landmarks. (b) optimization of the selected slice thickness.

The OVS prescription (Fig. 6.3) included 5 pairs of parallel bands, implemented with dualband pulses (dashed lines) and 4 tilted sat bands in a

pyramid configuration (solid lines). The position and orientation of the OVS planes were optimized by minimizing a cost function, as described in chapter 5.

As in the previous methods, the position and orientation of the bands was constrained to be symmetrical. The use of dualband pulses, introduced additional constraints to the geometry of the planes, ensuring that the bands that were to be generated by a single pulse remained parallel. On the other hand, an additional degree of freedom – a global angle of rotation around the Z axis was added to the model to accommodate for the head tilt.

The optimization of the saturation bands were performed in the following sequence:

1. Optimizing Distances Only (Fig. 6.3a)
2. Optimization in sagittal plane. (parallel bands are shown as dashed lines)  
(Fig. 6.3b)
3. Optimization in coronal plane (Fig. 6.3c)
4. Optimization in axial plane.(includes rotation around Z axis to accommodate head tilt) (Fig. 6.3d)

Saturation bands were generated from planes by adding thickness.

The automated prescription software was run on the scanner console during the MRI/MRSI exam, as described in chapter 3. Total optimization time was around 30 seconds.

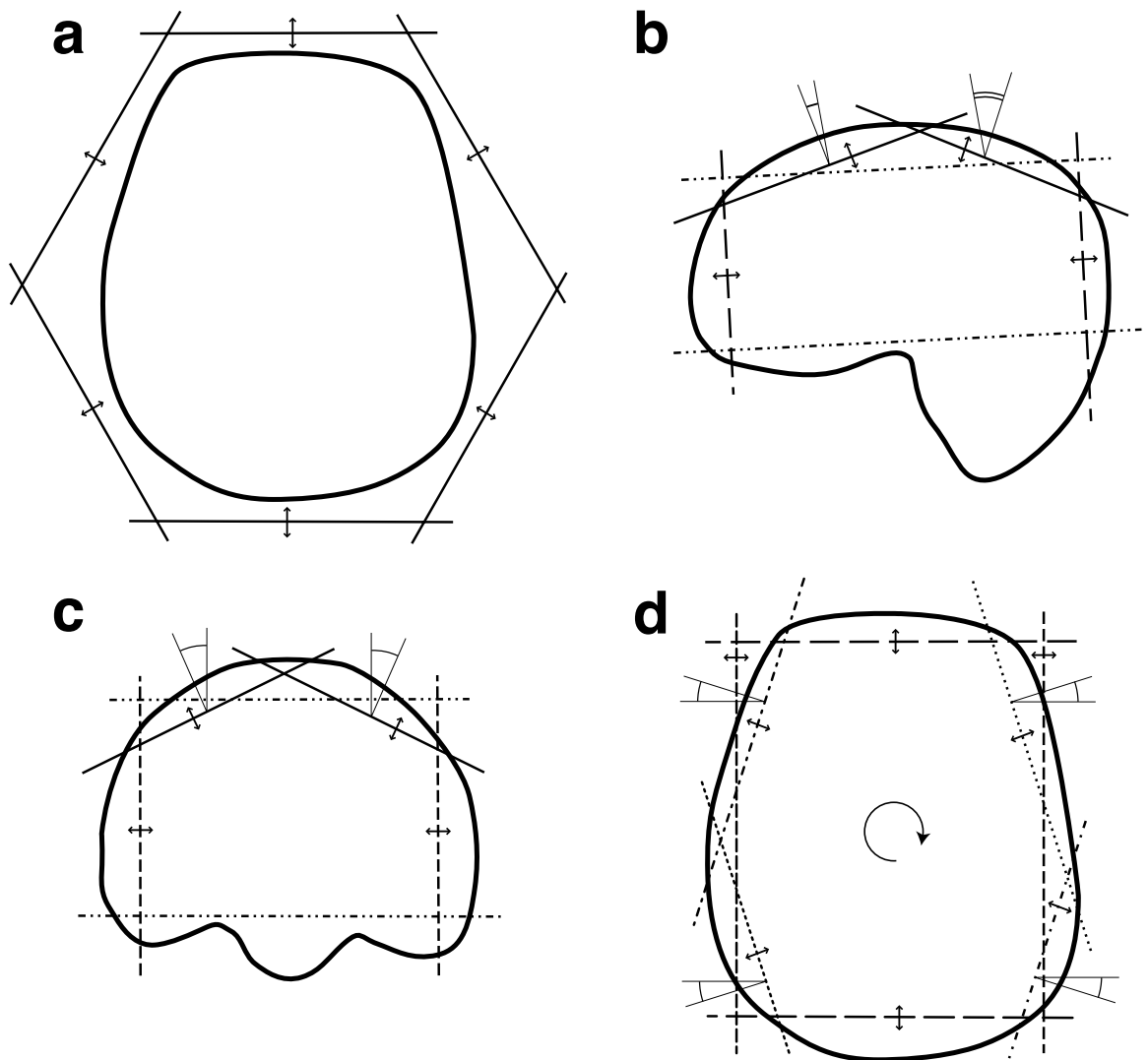


**Figure 6.3.** Saturation band optimization sequence.

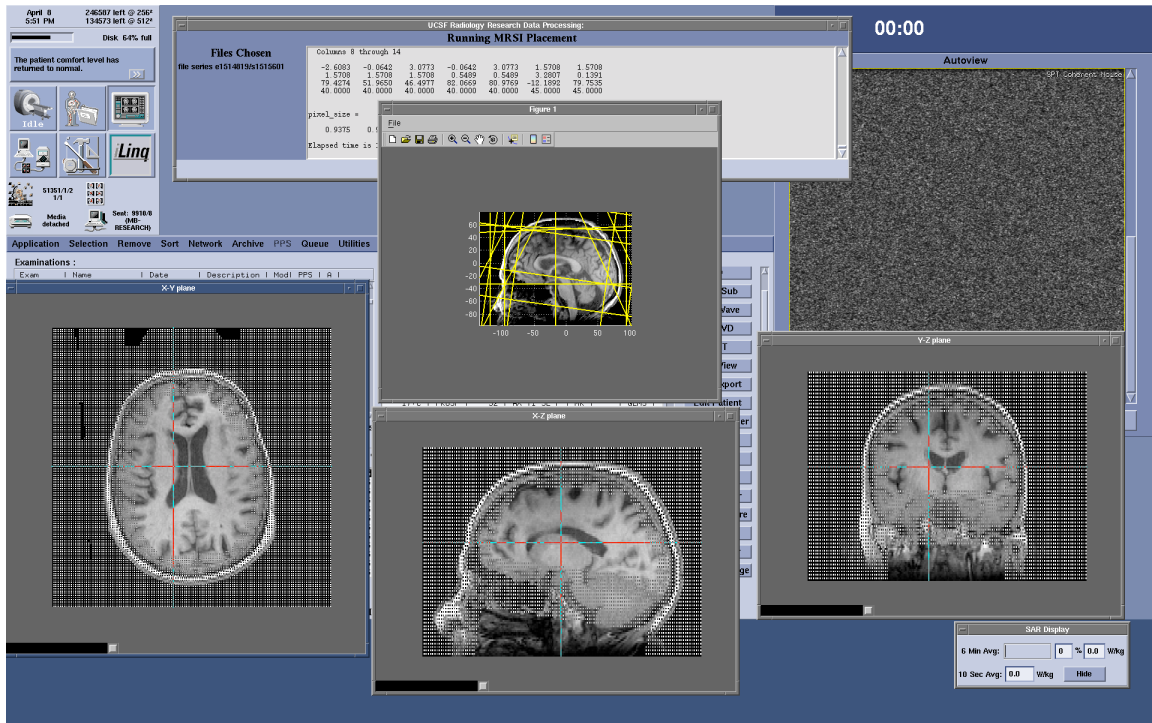


**Figure 6.4.** Software on the scanner console.

### Pulse Sequence

To achieve slice selection, the PRESS MRSI pulse sequence (Fig. 6.5) was modified to make the X and Y refocusing pulses non-selective. The slice selection and OVS band parameters were defined by files generated by the automatic prescription software. For dual-band pulses, the waveform of the pulse was calculated within the pulse sequence, based on the distance between the pair of bands. To minimize the chance of the artifacts caused by stimulated echoes in the areas, covered by more than one sat band, the crusher gradients in X, Y and Z followed cosine patterns, offset by 120 deg. phase from each other similar to the method in (34).

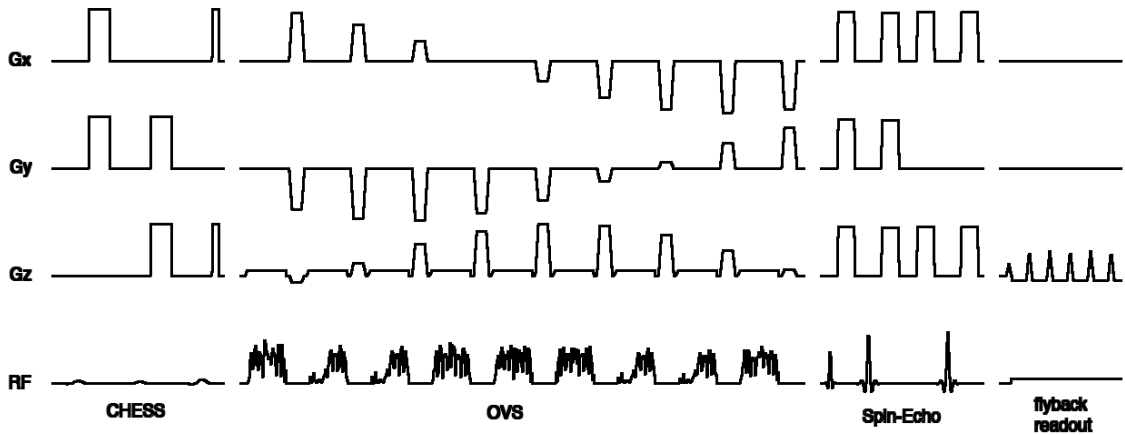


**Figure 6.5.** MRSI pulse sequence with single- and dual-band OVS pulses (sections scaled differently).

### RF Pulse Design

Exponential-modulated dualband VSS pulses were implemented in collaboration with Adam Kerr (Stanford University), as described in chapter 3. More efficient RF pulse design allowed to reduce the duration of a dualband pulse from 6 ms to 3.6 ms without exceeding the RF power limit of the hardware.

Each dualband pulse generated a pair of parallel OVS bands. That allowed to reduce the number of RF pulses in saturation train, reducing the total duration of the OVS block to 51 ms and ultimately reducing the T1 sensitivity of water and lipid suppression.

### MRSI Acquisition

Long echo (TE = 144 ms) and short echo (TE = 35 ms) MRSI data were acquired on a 3T GE scanner with an echo-planar flyback sequence (18x18x16, 1cc isotropic voxels,  $T_{\text{acq}} = 6.5 \text{ min}$ ). Raw data were reconstructed and processed offline, using methods, described previously (15).

## Results and Discussion

To assess the behavior of the dualband pulses, phantom images were acquired with the same excitation and OVS as in the MRSI acquisition. Exponential modulated dualband pulses exhibited a much sharper transition band than the cosine modulated pulses, with a slight increase in out-of-slice ripple. The observed ripple had a wavelength, much shorter than the dimensions of the voxel (1 cm) and did not cause inter-voxel variation of the signal.

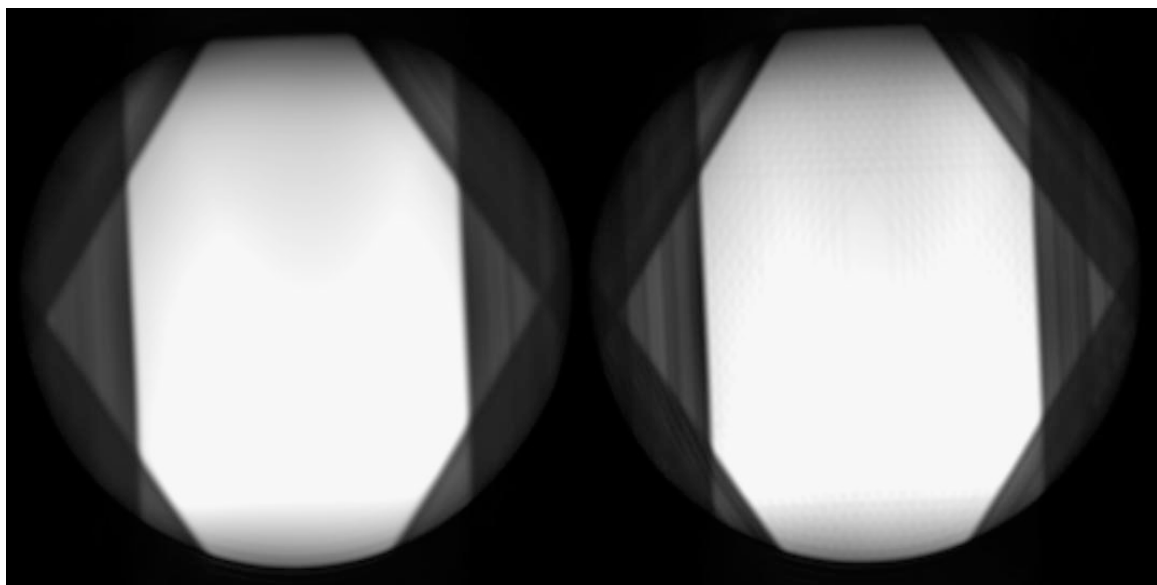


**Figure 6.6.** Comparison of images of a phantom with cosine-modulated dualband pulses (left) and exponential-modulated dualband pulses (right).

Long echo and short echo MRSI data were acquired from 2 healthy volunteers and 2 patients with brain tumors. For long echo MRSI (Fig. 6.7b,d), the technique achieved good spectral quality, with Cho, Cr and NAA peaks clearly visible. The metabolite map shows that data was acquired from almost the whole volume of the supratentorial brain, a much larger volume than that shown in earlier

approaches. In short-echo data (Fig. 6.7c,e), the lipid peak was more prominent due to its short T2, but did not overlap with the NAA peak in most voxels. Additional peaks, such as mI and Glx, could be resolved.

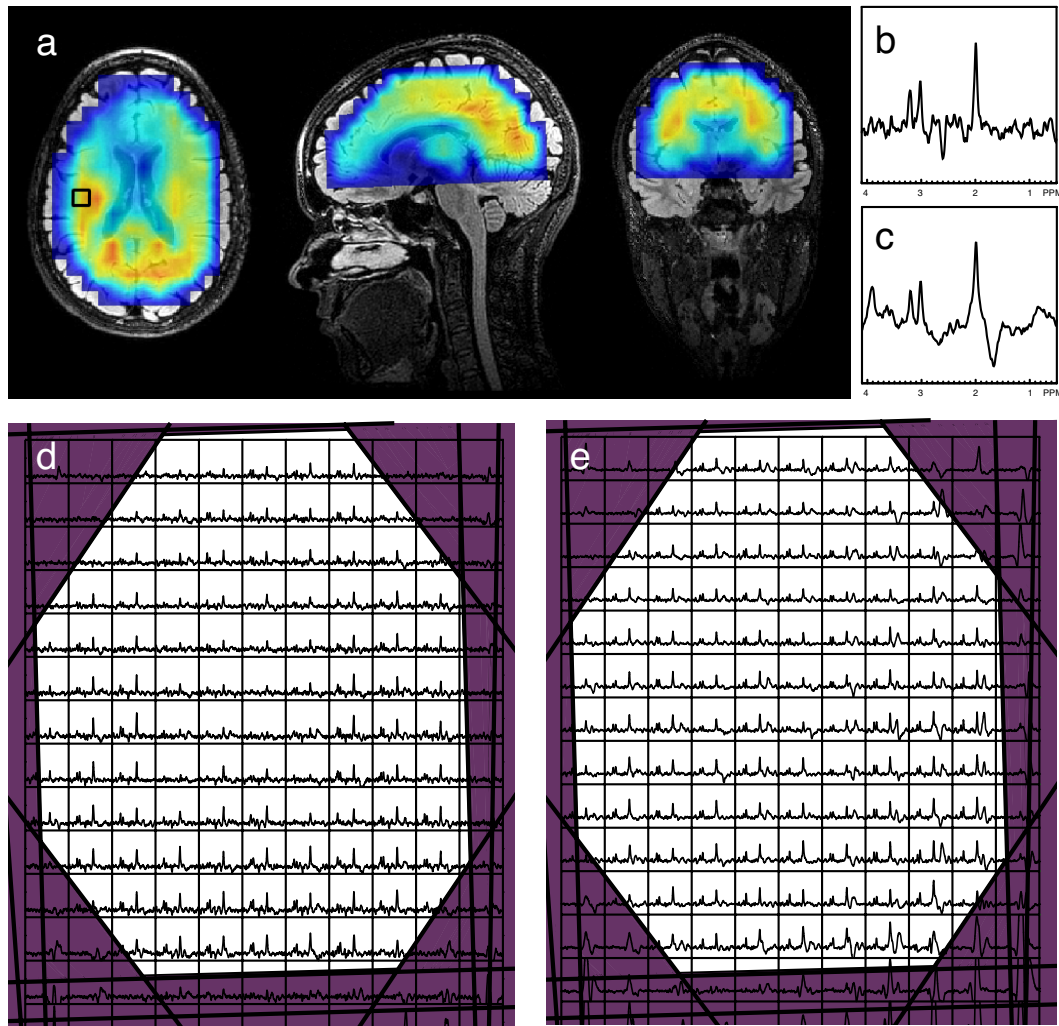


**Figure 6.7.** Healthy volunteer MRSI acquisition.

(a) NAA metabolite maps; (b) sample voxel  $TE=144\text{ ms}$ ; (c)  $TE=35\text{ ms}$ ; (d) axial spectral slice  $TE = 144\text{ ms}$ ; (e)  $TE=35\text{ ms}$

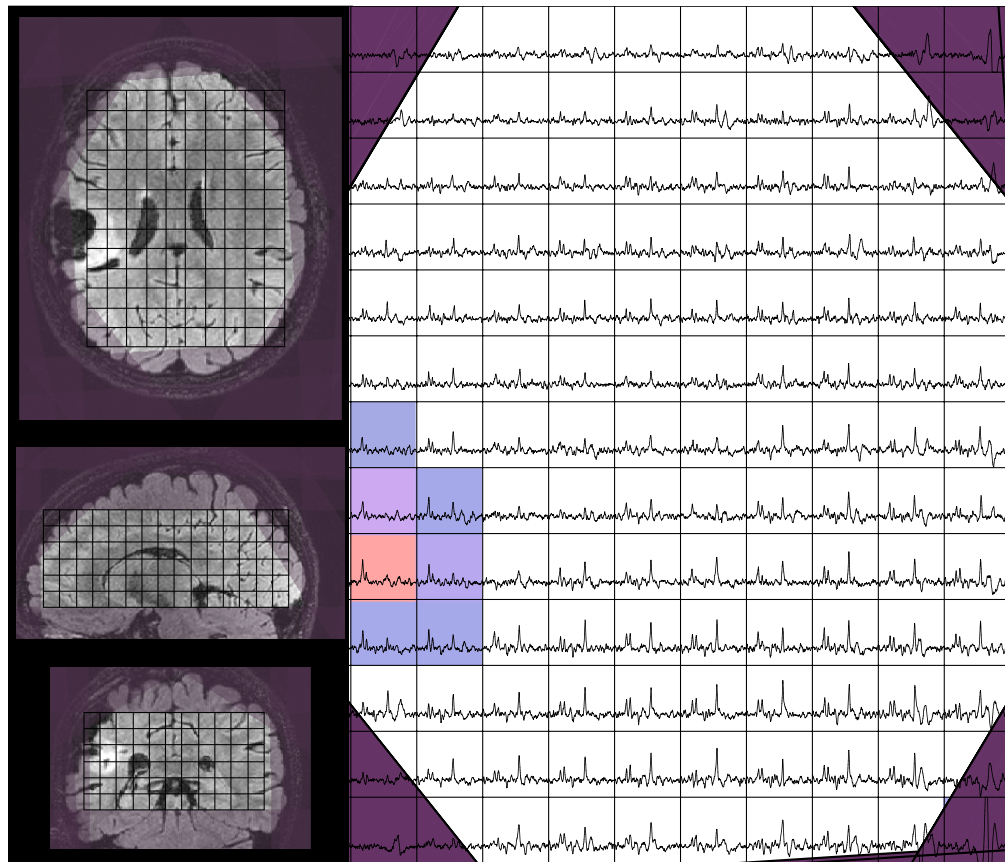


**Figure 6.8. Patient Data (Long Echo).**

In this work we have demonstrated combining automatic prescription and slice-selective excitation. The novel dualband OVS pulses helped minimize the length of the OVS pulse train and allowed to use more bands to better approximate brain shape. The use of slice selection instead of PRESS will allow a single spin-echo sequence to be implemented to achieve even shorter echo times and reduce RF power deposition.

These results indicate, that OVS alone, while sufficient for long-echo MRSI may not be sufficient to reliably achieve the needed level of lipid suppression for short echo acquisitions. The lipid signal could be improved by combining OVS with other techniques, such as short TI inversion recovery (STIR). This approach has

been successfully implemented at 7T by Yan Li and presented at the 2012 ISMRM meeting (74).

In conclusion, the combination of slice-selective excitation and effective outer-volume suppression using dualband VSS pulses allowed high-quality 3D MRSI data from supratentorial brain to be acquired in only 6.5 min. Automated prescription allows this technique to be implemented without the need of significant operator training.

## **Summary**

Proton Magnetic Resonance Spectroscopic Imaging (MRSI) is a valuable modality for diagnosis and evaluation of brain diseases. Two major difficulties encountered in implementing MRSI in a clinical setting are limited coverage and difficulty in prescription. The goal of my dissertation work was the development of novel techniques for automation of MRSI scan planning and acquisition.

In order to enable this work, I have implemented a number of new features for the scanner software and the MRSI pulse sequence, including dual-band Very-Selective Suppression (VSS) pulses for outer-volume suppression (OVS), octagonal OVS scheme, interface between a pulse sequence, shimming algorithm and an external process, allowing to use calculated geometrical parameters during MRSI acquisition. I have also developed software for automated OVS band placement, optimization of the geometry of an oblique selected volume or selected slice that can be run on an MRI scanner during the exam. The data processing and visualization pipeline had to be modified to allow the processing of the oblique 3D MRSI datasets with extended coverage that are acquired with the automated protocols. The technical details of these software projects were described in chapter 3.

### **Automated Saturation Band Placement**

Chapter 4 described the development of a technique for optimizing coverage of brain 3D MRSI by automated placement of outer-volume suppression (OVS) saturation bands and compared the performance for PRESS MRSI protocols with manual and automatic placement of saturation bands.

Excitation of subcutaneous lipids has been a major problem in 3D brain MRSI that has limited the coverage obtained. OVS saturation bands are commonly used to further reduce the lipid excitation. Manual placement of these sat bands is time-consuming and depends on the skill of the operator. Thus, it is hard to ensure consistently good placement of the sat bands, which is necessary to obtain useful MRSI data. This is one major reason why MRSI is currently not widely used in a clinical setting. To improve coverage of the brain and to simplify prescription of 3D MRSI, we have developed a technique for automatic optimization of sat band position and orientation that simultaneously maximizes coverage of subcutaneous fat by the sat bands and minimizes the portion of brain tissue that is suppressed.

The automated OVS procedure included the acquisition of anatomic images from the head, obtaining brain and lipid tissue maps, calculating optimal saturation band placement and then using those optimized parameters during the MRSI acquisition. The data were analyzed to quantify brain coverage volume and data quality.

3D PRESS MRSI data were acquired from 3 healthy volunteers and 29 patients using protocols that included either manual or automatic sat band placement. On average, the automatic sat band placement allowed the acquisition of PRESS MRSI data from 2.7 times larger brain volumes than the conventional method, while maintaining data quality. This work led to a publication "Improved Spatial Coverage for Brain 3D PRESS MRSI by Automatic Placement of Outer-Volume Suppression Saturation Bands" (1).

## **Automated Oblique Prescription**

My second project (chapter 5) was to completely automate the process of 3D PRESS MRSI prescription, including placement of the selection box, saturation bands and shim volume, while maximizing the coverage of the brain. Two major difficulties encountered in implementing Magnetic Resonance Spectroscopic Imaging (MRSI) in a clinical setting are limited coverage and difficulty in prescription.

The automated prescription technique included acquisition of an anatomical MRI image, optimization of the oblique selection box parameters, optimization of the placement of OVS saturation bands, and loading of the calculated parameters into a customized 3D MRSI pulse sequence.

To validate the technique and compare its performance with existing protocols, 3D MRSI data were acquired from 6 exams from 3 healthy volunteers. To assess the performance of the automated 3D MRSI prescription for patients with brain tumors, the data were collected from 16 exams from 8 subjects with gliomas. This technique demonstrated robust coverage of the tumor, high consistency of prescription and very good data quality within the T2 lesion. This work led to a manuscript "Automated Prescription of 3D Brain MRSI Data" (2).

## **Slice-Selected 3D MRSI with Automated Prescription**

To further increase the covered volume, I have developed a technique that combined a new automatic prescription algorithm with an MRSI protocol that uses slice selection in place of PRESS (chapter 6). Slice selection that excited a slab in space, instead of a box, as in PRESS puts additional requirements on the

performance of OVS. Collaborating with Adam Kerr from Magnetic Resonance System Research Laboratory at Stanford University we implemented low-power dual-band saturation pulses that simultaneously suppress two parallel bands. The pulse waveforms were modified after scan prescription to achieve optimal suppression.

The novel dualband OVS pulses helped minimize the length of the OVS pulse train and allowed to use more bands to better approximate brain shape. The use of slice selection instead of PRESS will allow a single spin-echo sequence to be implemented to achieve even shorter echo times and reduce RF power deposition. We found out, however, that OVS alone, while sufficient for long-echo MRSI may not be sufficient to reliably achieve the needed level of lipid suppression for short echo acquisitions. This work was presented at the 19th meeting of the International Society for Magnetic Resonance in Medicine (ISMRM) in May of 2011 (3).

## Conclusion

These projects required me to learn pulse sequence programming and debugging. They have also led me to acquire intricate knowledge of the low-level operation of MRI scanners, and have served to develop my understanding of MR physics, biochemistry and biology of cancer.

The results of this work show that automated prescription can help solve two of the most significant problems with brain PRESS MRSI acquisitions: limited brain coverage and difficulty in prescription. The improved coverage will be useful for evaluating heterogeneous and infiltrative tumors, as well as tumors at the periphery of the brain, which are difficult to evaluate with current protocols. It should make

possible a more accurate assessment of the progression of tumors in serial studies.

The use of this technique reduces the need for extensive operator training, thus facilitating wider utilization of MRSI in the clinical setting. These techniques have been implemented in the clinical setting and used to acquire data from hundreds of patients with brain tumors.

There are several potential areas of research and development that can build upon this work. The automated prescription techniques should be adapted for high field MR scanners, where lipid contamination is an even bigger problem than it is at 3T. The acquisition of high-quality full-brain spectra at short echo times requires a combination of fat suppression method, such as OVS, inversion recovery and spatial filtering. Coverage of the inferior portions of the brain can be further improved by an acquisition of a separate MRSI volume, covering those areas. The techniques presented in this work could be adapted to automated planning of MRSI acquisitions of other organs, such as the prostate. Finally, there needs to be a combined effort with the scanner manufacturers to make these tools a product, widely available to the hospitals and imaging centers.

## Bibliography

1. Ozhinsky E, Vigneron DB, Nelson SJ. Improved spatial coverage for brain 3D PRESS MRSI by automatic placement of outer-volume suppression saturation bands. *Journal of magnetic resonance imaging : JMRI* 2011;33(4):792-802.
2. Ozhinsky E, Vigneron DB, Chang SM, Nelson SJ. Automated prescription of oblique brain 3D magnetic resonance spectroscopic imaging. *Magnetic resonance in medicine : official journal of the Society of Magnetic Resonance in Medicine / Society of Magnetic Resonance in Medicine* 2012.
3. Ozhinsky E, Kerr AB, Nelson S. Novel Automated 3D MRSI Acquisition with Whole Brain Slice Selection and Outer-Volume Suppression. *Proceedings 19th Scientific Meeting, International Society for Magnetic Resonance in Medicine*; 2011; Montreal. p 3450.
4. American Cancer Society. *Cancer Facts & Figures 2012*. Atlanta: American Cancer Society; 2012.
5. Bernstein M, Berger MS. *Neuro-Oncology: The Essentials*: Thieme Medical Publishers; 2000.
6. Sanai N, Polley MY, McDermott MW, Parsa AT, Berger MS. An extent of resection threshold for newly diagnosed glioblastomas. *J Neurosurg* 2011;115(1):3-8.
7. Nelson SJ. Magnetic resonance spectroscopic imaging. Evaluating responses to therapy for gliomas. *IEEE engineering in medicine and biology magazine : the quarterly magazine of the Engineering in Medicine & Biology Society* 2004;23(5):30-39.

8. Bottomley PA. Spatial localization in NMR spectroscopy in vivo. *Ann N Y Acad Sci* 1987;508:333-348.
9. Conolly S, Pauly J, Nishimura D, Macovski A. Two-dimensional selective adiabatic pulses. *Magnetic resonance in medicine : official journal of the Society of Magnetic Resonance in Medicine / Society of Magnetic Resonance in Medicine* 1992;24(2):302-313.
10. Cunningham CH, Vigneron DB, Chen AP, Xu D, Nelson SJ, Hurd RE, Kelley DA, Pauly JM. Design of flyback echo-planar readout gradients for magnetic resonance spectroscopic imaging. *Magn Reson Med* 2005;54(5):1286-1289.
11. Haase A, Frahm J, Hanicke W, Matthaei D. <sup>1</sup>H NMR chemical shift selective (CHESS) imaging. *Phys Med Biol* 1985;30(4):341-344.
12. Star-Lack J, Nelson SJ, Kurhanewicz J, Huang LR, Vigneron DB. Improved water and lipid suppression for 3D PRESS CSI using RF band selective inversion with gradient dephasing (BASING). *Magn Reson Med* 1997;38(2):311-321.
13. Star-Lack J, Spielman D, Adalsteinsson E, Kurhanewicz J, Terris DJ, Vigneron DB. In vivo lactate editing with simultaneous detection of choline, creatine, NAA, and lipid singlets at 1.5 T using PRESS excitation with applications to the study of brain and head and neck tumors. *J Magn Reson* 1998;133(2):243-254.
14. Kim DH, Adalsteinsson E, Glover GH, Spielman DM. Regularized higher-order in vivo shimming. *Magnetic resonance in medicine : official journal of the*

- Society of Magnetic Resonance in Medicine / Society of Magnetic Resonance in Medicine 2002;48(4):715-722.
15. Nelson SJ. Analysis of volume MRI and MR spectroscopic imaging data for the evaluation of patients with brain tumors. *Magn Reson Med* 2001;46(2):228-239.
  16. Osorio JA, Ozturk-Isik E, Xu D, Cha S, Chang S, Berger MS, Vigneron DB, Nelson SJ. 3D 1H MRSI of brain tumors at 3.0 Tesla using an eight-channel phased-array head coil. *J Magn Reson Imaging* 2007;26(1):23-30.
  17. Crane JC, Olson MP, Nelson SJ. SIVIC: An Extensible Open-Source DICOM MR Spectroscopy Software Framework and Application Suite. *Proceedings 18th Scientific Meeting, International Society for Magnetic Resonance in Medicine*; 2010; Stockholm. p 3354.
  18. Gonen O, Viswanathan AK, Catalaa I, Babb J, Udupa J, Grossman RI. Total brain N-acetylaspartate concentration in normal, age-grouped females: quantitation with non-echo proton NMR spectroscopy. *Magnetic resonance in medicine : official journal of the Society of Magnetic Resonance in Medicine / Society of Magnetic Resonance in Medicine* 1998;40(5):684-689.
  19. Woodward P. *MRI for technologists*. New York: McGraw-Hill Medical Pub. Division; 2001. iv, 408 p. p.
  20. Scheufler O, Kania NM, Heinrichs CM, Exner K. Hyperplasia of the subcutaneous adipose tissue is the primary histopathologic abnormality in lipedematous scalp. *Am J Dermatopathol* 2003;25(3):248-252.

21. Zhu H, Ouwerkerk R, Barker PB. Dual-band water and lipid suppression for MR spectroscopic imaging at 3 Tesla. *Magn Reson Med* 2010;63(6):1486-1492.
22. Bley TA, Wieben O, Francois CJ, Brittain JH, Reeder SB. Fat and water magnetic resonance imaging. *Journal of magnetic resonance imaging : JMRI* 2010;31(1):4-18.
23. Dixon WT. Simple proton spectroscopic imaging. *Radiology* 1984;153(1):189-194.
24. Bydder GM, Steiner RE, Blumgart LH, Khenia S, Young IR. MR imaging of the liver using short TI inversion recovery sequences. *J Comput Assist Tomogr* 1985;9(6):1084-1089.
25. Spielman DM, Pauly JM, Macovski A, Glover GH, Enzmann DR. Lipid-suppressed single- and multisection proton spectroscopic imaging of the human brain. *J Magn Reson Imaging* 1992;2(3):253-262.
26. Hetherington HP, Pan JW, Mason GF, Ponder SL, Twieg DB, Deutsch G, Mountz J, Pohost GM. 2D 1H spectroscopic imaging of the human brain at 4.1 T. *Magn Reson Med* 1994;32(4):530-534.
27. Balchandani P, Spielman D. Fat suppression for 1H MRSI at 7T using spectrally selective adiabatic inversion recovery. *Magnetic resonance in medicine : official journal of the Society of Magnetic Resonance in Medicine / Society of Magnetic Resonance in Medicine* 2008;59(5):980-988.
28. Crawford FW, Khayal IS, McGue C, Saraswathy S, Pirzkall A, Cha S, Lamborn KR, Chang SM, Berger MS, Nelson SJ. Relationship of pre-surgery metabolic

- and physiological MR imaging parameters to survival for patients with untreated GBM. *J Neurooncol* 2009;91(3):337-351.
29. Andronesi OC, Gagoski BA, Sorensen AG. Neurologic 3D MR spectroscopic imaging with low-power adiabatic pulses and fast spiral acquisition. *Radiology* 2012;262(2):647-661.
30. Maudsley AA, Domenig C, Sheriff S. Reproducibility of serial whole-brain MR spectroscopic imaging. *NMR in biomedicine* 2010;23(3):251-256.
31. Tran TK, Vigneron DB, Sailasuta N, Tropp J, Le Roux P, Kurhanewicz J, Nelson S, Hurd R. Very selective suppression pulses for clinical MRSI studies of brain and prostate cancer. *Magn Reson Med* 2000;43(1):23-33.
32. Xu D, Chen AP, Cunningham C, Osorio JA, Nelson SJ, Vigneron DB. Spectroscopic imaging of the brain with phased-array coils at 3.0 T. *Magn Reson Imaging* 2006;24(1):69-74.
33. Henning A, Schar M, Schulte RF, Wilm B, Pruessmann KP, Boesiger P. SELOVS: brain MRSI localization based on highly selective T1- and B1- insensitive outer-volume suppression at 3T. *Magn Reson Med* 2008;59(1):40-51.
34. Henning A, Fuchs A, Murdoch JB, Boesiger P. Slice-selective FID acquisition, localized by outer volume suppression (FIDLOVS) for  $^1\text{H}$ -MRSI of the human brain at 7 T with minimal signal loss. *NMR Biomed* 2009;22(7): 683-696.
35. Posse S, Otazo R, Caprihan A, Bustillo J, Chen H, Henry PG, Marjanska M, Gasparovic C, Zuo C, Magnotta V, Mueller B, Mullins P, Renshaw P, Ugurbil K, Lim KO, Alger JR. Proton echo-planar spectroscopic imaging of J-coupled

- resonances in human brain at 3 and 4 Tesla. Magnetic resonance in medicine : official journal of the Society of Magnetic Resonance in Medicine / Society of Magnetic Resonance in Medicine 2007;58(2):236-244.
36. Yung KT, Zheng W, Zhao C, Martinez-Ramon M, van der Kouwe A, Posse S. Atlas-based automated positioning of outer volume suppression slices in short-echo time 3D MR spectroscopic imaging of the human brain. Magnetic resonance in medicine : official journal of the Society of Magnetic Resonance in Medicine / Society of Magnetic Resonance in Medicine 2011;66(4):911-922.
37. Dantzig GB, Orden A, Wolfe P. The generalized simplex method for minimizing a linear form under linear inequality restraints. Pacific Journal Math 1955;5:183-195.
38. Lagarias JC, Reeds JA, Wright MH, Wright PE. Convergence properties of the Nelder-Mead simplex method in low dimensions. Siam J Optimiz 1998;9(1):112-147.
39. Osorio JA, Xu D, Cunningham CH, Chen A, Kerr AB, Pauly JM, Vigneron DB, Nelson SJ. Design of cosine modulated very selective suppression pulses for MR spectroscopic imaging at 3T. Magn Reson Med 2009;61(3):533-540.
40. Kerr A, Larson P, Vigneron D, Pauly J. Reduced Peak Power Dualband VSS Pulse Design. Proceedings 17th Scientific Meeting, International Society for Magnetic Resonance in Medicine; 2009 April; Honolulu. p 2577.
41. Shinnar M. Reduced power selective excitation radio frequency pulses. Magnetic resonance in medicine : official journal of the Society of Magnetic

- Resonance in Medicine / Society of Magnetic Resonance in Medicine  
1994;32(5):658-660.
42. Pickup S, Ding X. Pulses with fixed magnitude and variable phase response profiles. *Magnetic resonance in medicine : official journal of the Society of Magnetic Resonance in Medicine / Society of Magnetic Resonance in Medicine* 1995;33(5):648-655.
43. Pauly J, Le Roux P, Nishimura D, Macovski A. Parameter relations for the Shinnar-Le Roux selective excitation pulse design algorithm [NMR imaging]. *IEEE transactions on medical imaging* 1991;10(1):53-65.
44. Zierhut ML, Ozturk-Isik E, Chen AP, Park I, Vigneron DB, Nelson SJ. (1)H spectroscopic imaging of human brain at 3 Tesla: comparison of fast three-dimensional magnetic resonance spectroscopic imaging techniques. *Journal of magnetic resonance imaging : JMRI* 2009;30(3):473-480.
45. Di Costanzo A, Scarabino T, Trojsi F, Popolizio T, Catapano D, Giannatempo GM, Bonavita S, Portaluri M, Tosetti M, d'Angelo VA, Salvolini U, Tedeschi G. Proton MR spectroscopy of cerebral gliomas at 3 T: spatial heterogeneity, and tumour grade and extent. *Eur Radiol* 2008;18(8):1727-1735.
46. Xu M, See SJ, Ng WH, Arul E, Back MF, Yeo TT, Lim CC. Comparison of magnetic resonance spectroscopy and perfusion-weighted imaging in presurgical grading of oligodendroglial tumors. *Neurosurgery* 2005;56(5): 919-926; discussion 919-926.
47. Rijpkema M, Schuuring J, van der Meulen Y, van der Graaf M, Bernsen H, Boerman R, van der Kogel A, Heerschap A. Characterization of

- oligodendrogiomas using short echo time 1H MR spectroscopic imaging. NMR Biomed 2003;16(1):12-18.
48. Hattingen E, Delic O, Franz K, Pilatus U, Raab P, Lanfermann H, Gerlach R. (1)H MRSI and progression-free survival in patients with WHO grades II and III gliomas. Neurol Res 2009.
49. Kuznetsov YE, Caramanos Z, Antel SB, Preul MC, Leblanc R, Villemure JG, Pokrupa R, Olivier A, Sadikot A, Arnold DL. Proton magnetic resonance spectroscopic imaging can predict length of survival in patients with supratentorial gliomas. Neurosurgery 2003;53(3):565-574; discussion 574-566.
50. Chang SM, Nelson S, Vandenberg S, Cha S, Prados M, Butowski N, McDermott M, Parsa AT, Aghi M, Clarke J, Berger M. Integration of preoperative anatomic and metabolic physiologic imaging of newly diagnosed glioma. J Neurooncol 2009;92(3):401-415.
51. Narayana A, Chang J, Thakur S, Huang W, Karimi S, Hou B, Kowalski A, Perera G, Holodny A, Gutin PH. Use of MR spectroscopy and functional imaging in the treatment planning of gliomas. Br J Radiol 2007;80(953):347-354.
52. Sajja BR, Wolinsky JS, Narayana PA. Proton magnetic resonance spectroscopy in multiple sclerosis. Neuroimaging Clin N Am 2009;19(1):45-58.
53. Patel MS, Hu X. A robust algorithm for reduction of truncation artifact in chemical shift images. IEEE Trans Med Imaging 1993;12(4):812-818.
54. Seber GAF. Multivariate observations. New York: Wiley; 1984. 686 p.

55. Li T, Martinez-Ramon M, Heileman G, Posse S. Automatic Outer Volume Suppression (OVS) Slice Placement for Proton-Echo-Planar-Spectroscopic-Imaging (PEPSI). Proceedings of the 14th Annual Meeting of ISMRM; 2006 May; Seattle. p 3086.
56. Zhang Y, Brady M, Smith S. Segmentation of brain MR images through a hidden Markov random field model and the expectation-maximization algorithm. IEEE Trans Med Imaging 2001;20(1):45-57.
57. Li Y, Srinivasan R, Ratiney H, Lu Y, Chang SM, Nelson SJ. Comparison of T(1) and T(2) metabolite relaxation times in glioma and normal brain at 3T. J Magn Reson Imaging 2008;28(2):342-350.
58. Han E, Gold G, Stainsby J, Wright G, Beaulieu C, Brittain J. In-Vivo T1 and T2 Measurements of Muskuloskeletal Tissue at 3T and 1.5T. Proceedings 11th Scientific Meeting, International Society for Magnetic Resonance in Medicine; 2003 July; Toronto. p 450.
59. Hovdebo J, Ryner L. An Improved Method for Automatic Placement of Spatial Saturation Planes in MR Spectroscopy. Proceedings of the 17th Annual Meeting of ISMRM; 2009 April; Honolulu. p 2376.
60. Ryner L, Westmacott G, Davison N, Latta P. Automated Positioning of Multiple Spatial Saturation Planes for Non-Cuboidal Voxel Prescription in MR Spectroscopy Proceedings of the 13th Annual Meeting of ISMRM; 2005; Miami. p 350.
61. Martinez-Ramon M, Gallardo-Antolin A, Cid-Sueiro J, Heileman GL, Yung KT, Zheng W, Zhao C, Posse S. Automatic placement of outer volume suppression

- slices in MR spectroscopic imaging of the human brain. *Magn Reson Med* 2010;63(3):592-600.
62. Horska A, Barker PB. Imaging of brain tumors: MR spectroscopy and metabolic imaging. *Neuroimaging clinics of North America* 2010;20(3):293-310.
63. Bonavita S, Di Salle F, Tedeschi G. Proton MRS in neurological disorders. *Eur J Radiol* 1999;30(2):125-131.
64. Young S, Bystrov D, Netsch T, Bergmans R, van Muiswinkel A, Visser F, Sprigorum R, Gieseke G. Automated planning of MRI neuro scans. *Proc SPIE* 2006;6144, 61441M.
65. Tao X, Gupta S. Automatic Scan Plane Planning Method for Brain MRI. Proceedings 17th Scientific Meeting, International Society for Magnetic Resonance in Medicine; 2009 April; Honolulu. p 2903.
66. Itti L, Chang L, Ernst T. Automatic scan prescription for brain MRI. *Magnetic resonance in medicine : official journal of the Society of Magnetic Resonance in Medicine / Society of Magnetic Resonance in Medicine* 2001;45(3):486-494.
67. Nelles M, Gieseke J, Urbach H, Semrau R, Bystrov D, Schild HH, Willinek WA. Pre- and postoperative MR brain imaging with automatic planning and scanning software in tumor patients: an intraindividual comparative study at 3 Tesla. *Journal of magnetic resonance imaging : JMRI* 2009;30(3):672-677.

68. Gedat E, Braun J, Sack I, Bernarding J. Prospective registration of human head magnetic resonance images for reproducible slice positioning using localizer images. *Journal of magnetic resonance imaging : JMRI* 2004;20(4):581-587.
69. van der Kouwe AJ, Benner T, Fischl B, Schmitt F, Salat DH, Harder M, Sorensen AG, Dale AM. On-line automatic slice positioning for brain MR imaging. *NeuroImage* 2005;27(1):222-230.
70. van den Boomgaard R, van Balen R. Methods for fast morphological image transforms using bitmapped binary images. *CVGIP: Graphical Models and Image Processing* 1992;54(3):252-258.
71. Byrd RH, Gilbert JC, Nocedal J. A Trust Region Method Based on Interior Point Techniques for Nonlinear Programming *Mathematical Programming* 2000;89(1):149–185.
72. Bland JM, Altman DG. Statistical methods for assessing agreement between two methods of clinical measurement. *Lancet* 1986;1(8476):307-310.
73. McKnight TR, Noworolski SM, Vigneron DB, Nelson SJ. An automated technique for the quantitative assessment of 3D-MRSI data from patients with glioma. *Journal of magnetic resonance imaging : JMRI* 2001;13(2):167-177.
74. Li Y, Larson P, Chen AP, Kelley DA, Chang SM, Nelson SJ. Characterization of Gliomas Using MRI and Short Echo 1-H MRSI at 7 Tesla. *Proceedings 20th Scientific Meeting, International Society for Magnetic Resonance in Medicine;* 2012; Melbourne. p 1807.

### **Publishing Agreement**

*It is the policy of the University to encourage the distribution of all theses, dissertations, and manuscripts. Copies of all UCSF theses, dissertations, and manuscripts will be routed to the library via the Graduate Division. The library will make all theses, dissertations, and manuscripts accessible to the public and will preserve these to the best of their abilities, in perpetuity.*

### ***Please sign the following statement:***

*I hereby grant permission to the Graduate Division of the University of California, San Francisco to release copies of my thesis, dissertation, or manuscript to the Campus Library to provide access and preservation, in whole or in part, in perpetuity.*



Author Signature

10.01.2012

Date